International PhD in atomic
and molecular photonics

CYCLE XXXII

Coordinator Prof. Cataliotti Francesco Saverio

# Morpho-functional investigation of electro-mechanical dysfunction in cardiac hypertrophy by advanced optical methods and tissue transformation

Academic Discipline (SSD): FIS / 03

| **Doctoral Candidate** | **Supervisor** |
|---|---|
| Dr. Lazzeri Erica | Dr. Sacconi Leonardo |

**Coordinator**
Prof. Cataliotti Francesco Saverio

Years 2016 / 2019

*Alla mia famiglia*

# Contents

# Summary

During my PhD, I performed functional and structural investigations on the heart; I optimized clearing and staining protocols on cardiac tissue, and I exploited advanced imaging techniques to perform high-resolution studies working at two different projects.

In the first project, the energetics of demembranated multicellular cardiac muscle strips were investigated from three Hypertrophy Cardiomyopathy (HCM) patients with the E258K mutation. Energetic measurements in multicellular preparations may suffer from artefacts, related to the density and the orientation of the contractile material. Alterations of cardiomyocytes organization or disarray, a common HCM histopathological feature at whole heart level, may decrease isometric tension while increasing the isometric ATPase of multicellular preparations, thus leading to an artificial increase in tension cost (TC). To exclude this hypothesis, a new protocol that combines a novel tissue clearing technique, previously used to clear the mouse brain [1], and an advanced optical microscopy, two-photon fluorescence microscope (TPFM), was developed. With this approach it was possible to perform a three-dimensional (3D) cytoarchitecture analysis of the myofibril orientation, with a micron-scale resolution, on a subset of human ventricular strips previously used for mechanical and energetical experiments.

In the second project, action potential propagation of entire hearts was investigated from a transgenic mouse model of HCM with a mutation on the gene coding for cardiac Troponin T (cTnT). The wide field system used to perform this investigation has already been utilized to study electrical activity [2]. Subsequently, on the same hearts employed for functional studies, clearing techniques were applied to make the tissue transparent and to homogenize the refractive index [3]. This is

necessary to label entire samples with fluorescent proteins, used to visualize cardiac fiber structure, and to execute high resolution imaging with light-sheet microscopy for large volume acquisitions. Finally, cyto-architecture analysis based on cardiomyocytes and myofilaments alignment was applied to correlate electro-mechanical dysfunction with structural alterations.

These innovative experimental approaches will allow to dissect the morphological causes leading to alterations of electrical conduction and to electro-mechanical dysfunction, and, more generally, will represent a whole new paradigm for diagnostic and therapeutic investigations.

# Part I

## Introduction

# Chapter I

# Motivation: the challenge of fine heart architecture

Cardiovascular diseases represent the main cause of death in Europe with major social and economic burdens. There are acquired and congenital diseases that, following cardiac remodelling processes, determine electrical conduction alterations with consequent electro-mechanical dysfunction and arrhythmias development. However, current predictive models of these alterations are based on non-integrated and low resolution information. In this thesis, we propose to characterize cardiac conduction system alterations in pathological models of great clinical relevance, exploiting innovative methods to perform high resolution imaging.

The heart is the central organ of the cardiovascular system and allows blood circulation through rhythmic contractions. The contraction is ensured by contractile cells named cardiomyocytes, these cells are joined together by specialized structures called jap junctions that allow almost free diffusion of ions. Thus, the cardiac muscle is a functional syncytium, in which an electrical signal named action potential (AP) propagates from cell to cell and activates myofilaments contraction. Therefore, 3D alignment of cells and myofilaments defines the conduction pathway of AP during cardiac contraction. Consequently, electro-mechanical dysfunctions are closely linked with structural alterations.

A relevant pathological model is HCM. The prevalence of the disease is approximately 1:500 in Caucasian young adults. HCM is a genetic heart disease characterized by left ventricular (LV) hypertrophy, which develops in the absence of other inciting factors, such as augmented hemodynamic load or infiltrative disorders. The most common morphologic pattern is an asymmetric LV hypertrophy which involves mainly the interventricular septum. However, other configurations of hypertrophy cannot be excluded and are not closely related to the graveness of the disease. A peculiar histological feature of HCM cardiomyocytes is the prominent disarray and fibrosis [4] (see figure 1).

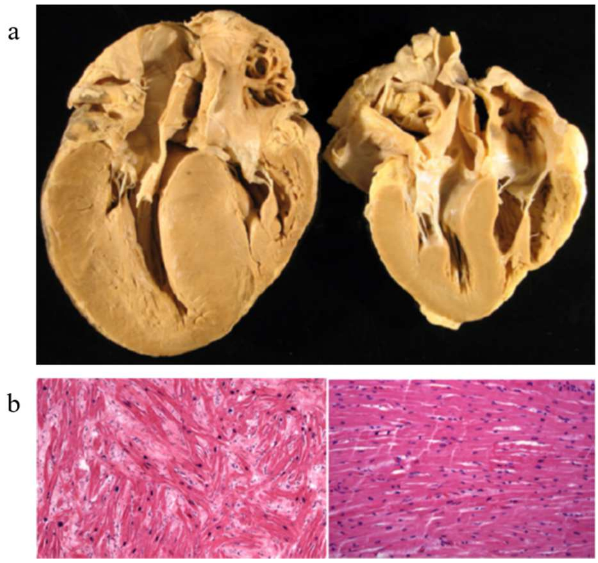

***Figure 1: Pathologic feature in HCM.*** ***(a)*** *Gross pathology showing hypertrophic cardiomyopathy (left) as compared to normal cardiac morphology (right).* ***(b)*** *Histologic sections stained with hematoxylin and eosin. HCM cardiomyocytes demonstrate disarray and variable orientation with an increased myocardial fibrosis (left). In contrast, normal myocardium demonstrates a very orderly arrangement of cardiomyocytes (right). Modified from* [4].

Disorganized cellular architecture and expanded interstitial collagen probably serve as arrhythmogenic substrates predisposing electro-mechanical instability. This substrate is likely the source of primary ventricular tachycardia and ventricular fibrillation, which appear to be the predominant mechanisms of sudden death [5]. Therefore, it is great relevance correlate 3D reconstructions with cellular resolution to electro-mechanical dysfunctions.

The traditional method to study tissue morphology is thin sections preparation. However, this method does not preserve the structure of intact conduction pathway and only provides two-dimensional (2D) information [6]. But biological structures are 3D, in fact, scientists have always tried to extend tissue imaging to thick specimens. On the imaging side, the invention of confocal microscopy [7], the development of two-photon microscopy [8] and the recent revival of light-sheet microscopy (LSM) [9] have provided a wide choice of microscopy methods allowing optical sectioning with 3D resolution. On the other hand, the effectiveness and usability of these techniques in macroscopic specimens are hampered, because biological specimens are naturally opaque. The main source of this opaqueness is scattering, that is caused by refractive index mismatching between biomolecules and surrounding medium [10].

To overcome this issue, tissue clearing methods that render tissues optically transparent by reducing scattering were developed (see figures 2 and 3). These techniques have been widely applied in neurosciences, but they are hardly used to study cardiac tissue.

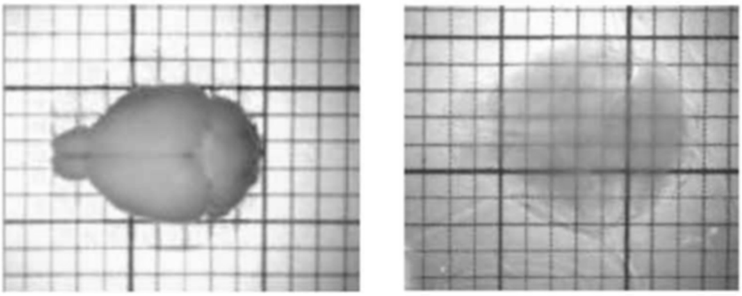

***Figure 2:*** *Transmission images of whole mouse brain before (left) and after (right) clearing protocol. From* [1]*.*

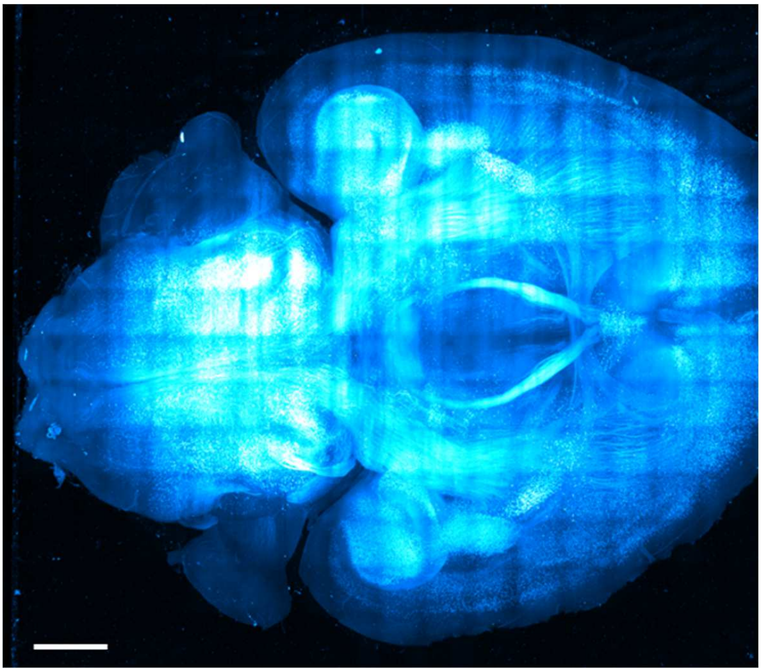

***Figure 3:*** *Maximum intensity projection of clarified mouse brain imaged with light-sheet microscopy. Scale bar 1 mm. From Pavone F. S. laboratory (LENS).*

In this thesis project, a clearing-imaging-analysis pipeline is developed to visualize cardiac conduction pathway in three-dimensions and a multi-technique approach is employed to correlate electro-mechanical dysfunction with structural alterations. In detail, this thesis is dedicated two different projects; one is related to correlating force production and energy consumption with structural alteration occurring in human samples of HCM. The other project regards the correlation between action potential propagation defects and cardiac conduction in a mouse model of HCM at the whole heart level.

# Chapter II

# Anatomy and physiology of the heart

## 2.1 Structural organization and action potential propagation

This section focuses on cardiac anatomy and physiology. These characteristics are at the base of the correct functioning of the heart. This first part describes the close correlation between structure and function that is essential for ensuring proper cardiac function.

### 2.1.1 Organ structure

The mammalian heart can be viewed as two separate pumps that operate in series: the right atrium and the right ventricle that pump blood from the systemic veins into the pulmonary circulation, and the left atrium and the left ventricle witch pump blood from pulmonary veins into systemic circulation (see figure 4). Within the heart, atrioventricular (AV) valves prevent blood from flowing backward from the ventricles into the atria: on the right the tricuspid valve and on the left the mitral valve. Semilunar valves separate each ventricle from its great artery: the pulmonic valve between the right ventricle and the pulmonary artery, the aortic valve between the left ventricle and the aorta. The cardiac wall presents three layers: epicardium, endocardium and myocardium. The epicardium is the outermost layer, while the endocardium is the innermost layer. The myocardium is the medium and thickest layer, and contains both cardiomyocytes and connective tissue. Although cardiomyocytes represent most of the myocardial mass, approximately 70% of the cells are smaller non-myocytes, which include vascular smooth muscle, endothelial cells and fibroblasts. Finally, the heart is enclosed in the double-walled pericardial sac. The sac consists of two layers: a tough, fibrous covering and a secretory lining. The outer fibrous covering of the sac attaches to the connective tissue that separates the lungs. The secretory lining produces a thin pericardial fluid, which provides lubrication to avoid friction between the pericardial layers as they glide over each other with every heartbeat.

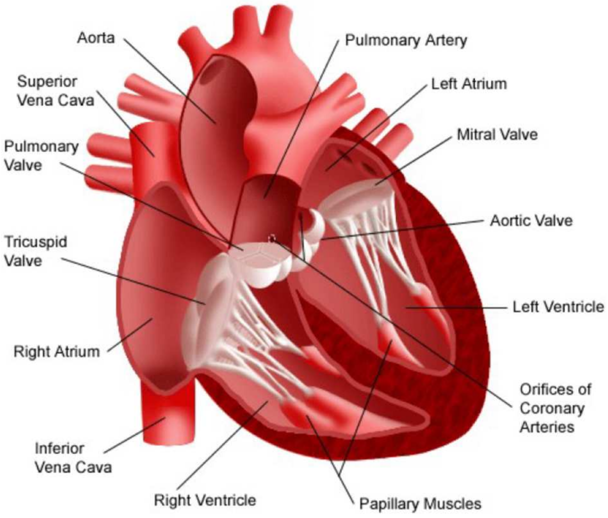

***Figure 4:*** *Interior view of the heart. From* [11].

### 2.1.2 Cardiac cycle

Each heartbeat is characterized by two phases that represent cardiac cycle: the systole (ventricular contraction) and the diastole (ventricular relaxation). Starting from a phase in which atria and ventricles are relaxed, blood enters the atria, passes through the AV valves and fills the ventricles. The semilunar valves are closed because the ventricular pressure is lower than the aortic one (see point 1, figure 5). At the end of the diastole, the atrial pressure exceeds that in the ventricle and a rapid filling occurs of the ventricles (see point 2, figure 5). At this point, the systole begins and the ventricles contract, increasing the pressure inside them. When the ventricular pressure exceeds the atrial one, the AV valves close (see point 3, figure 5).

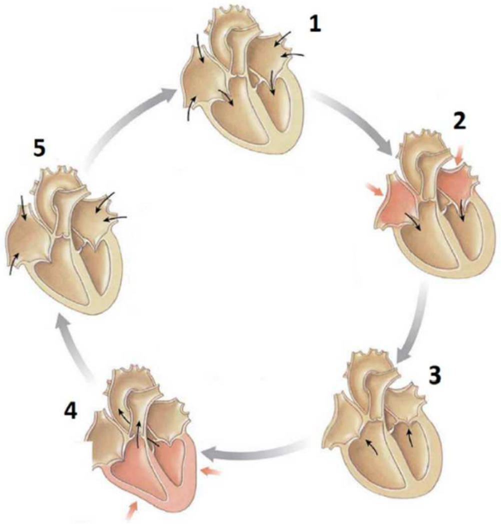

***Figure 5: Cardiac cycle representation.*** ***1****: late ventricular diastole;* ***2****: atrial systole;* ***3****: isovolumetric ventricular contraction;* ***4****: ventricular ejection;* ***5****: isovolumetric ventricular relaxation. Modified from* [12].

Consequently, the ventricular pressure increases and overcomes the aortic one. This induces opening of the semilunar valves (see point 4, figure 5). Blood is pushed into the aorta and pulmonary arteries, thus ventricular pressure decreases and when it becomes lower than the aortic one, the semilunar valves close (see point 5, figure 5). Therefore, the systole ends, and diastole begins. Blood enters the atria, but it does not flow into the ventricles because the AV valves are closed. When the ventricular pressure decreases, AV valves open and the cardiac cycle begins again.

### 2.1.3 Conduction system

Each cardiac cycle corresponds to a heart contraction that is generated by a signal, named AP, that originates within the muscle itself. This ability is due to the action of specialized muscle cells, called autorhythmic cells. There are two types of autorhythmic cells: pacemaker cells that induce AP and establish cardiac rhythm; and conduction fibres that propagate AP into the whole heart. These cells constitute the cardiac conduction system. Pacemaker cells are localized in two regions of the heart: the sinoatrial (SA) node located in the upper part of the right atrium, and the AV node placed in proximity of the tricuspid valve (see figure 6). The heartbeat is generated by the SA node because it has a higher frequency than the AV node (70 pulses/minute for the SA node against 50 pulses/minute for the AV node). So, an excitation wave starts from the SA node depolarizing atria. Then the wave propagates to the AV node, which spreads it to His bundle, consisting of muscle fibres located in the interventricular septum. The His bundle is divided in two branches that lead the wave to the right and left ventricles. Then the wave travels through an extended network of branches called Purkinje fibres, which reach the apex of the ventricles.

Finally, the wave spreads to the base of the heart, depolarizing the ventricles. This depolarizing wave generates muscle contraction.

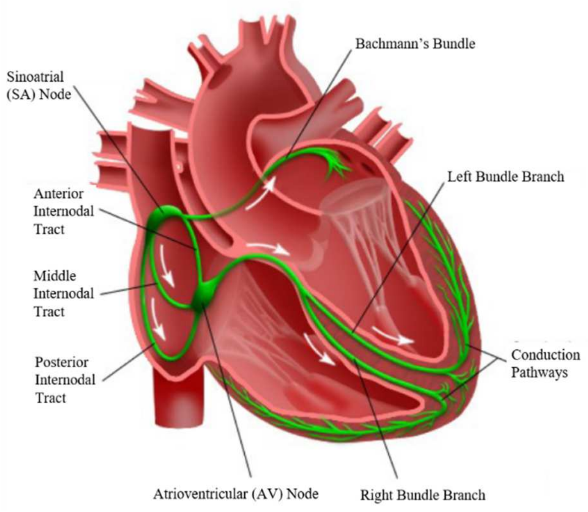

***Figure 6:*** *Scheme representing the electrical conducting system of the heart. From* [13].

### 2.1.4 Membrane potential of cardiomyocytes

Cardiomyocytes are excitable cells characterized by a membrane potential ($E_m$), that is a consequence of the unequal distribution of a few key ions between intracellular and extracellular fluids. The electrical properties of cardiomyocytes are determined by the selective movement of ions through the plasma membrane (sarcolemma). The resting $E_m$ is generated by $Na^+$ and $K^+$ ions, consequently, the $E_m$ changes depend on the electromechanical gradients of $Na^+$ and $K^+$ across the sarcolemma [14]. In fact, the intracellular and extracellular concentration of $Na^+$ and $K^+$ are different (see Table 1). This difference is maintained by the $Na^+$/

$K^+$ pump, that transports three $Na^+$ outside and two $K^+$ inside the cell. This unequal transport separates charges across the membrane, with the outside becoming more positive compared to the inside.

| Ion | $[X]_i$ (mM) | $[X]_e$ (mM) |
|---|---|---|
| $[Na^+]$ | 10 | 140 |
| $[K^+]$ | 145 | 5.4 |
| $[Ca^{2+}]$ | <1 | 1.8 |
| $[Cl^-]$ | 4 | 120 |
| $[A^-]$ | 0 | 65 |

***Table 1:*** *Intracellular (i) and extracellular (e) concentrations of the main ions that determine the potential difference across the sarcolemma.*

At rest, sarcolemma is almost exclusively permeable to $K^+$ establishing a Donnan Equilibrium where intracellular $[K^+]$ is much higher than extracellular concentration of the same ion. This means that $K^+$ tendency to move out of the cell following its concentration gradient is counterbalanced by the electrical gradient that would rather promote $K^+$ entry. The potential at this equilibrium is known as equilibrium potential of $K^+$, ($E_{k+}$). This equilibrium $E_x$ can be calculated for each ion (x) by the Nernst equation [equation 1].

$$E_x = \frac{RT}{z_x F} \ln\left(\frac{[X]_e}{[X]_i}\right) \qquad [1]$$

Where $R$ is the universal gas constant (8,314 $Jmol^{-1}K^{-1}$), $T$ is the absolute temperature, $z_x$ is the valence of the ion and $F$ is the Faraday's constant

(96,485 $Cmol^{-1}$). Using the values in table 1, the Nernst potentials are $E_{Na+}$ = 70 mV, $E_{K+}$ = -88 mV, $E_{Ca2+}$ = 128 mV and $E_{Cl-}$ = -80 mV at body temperature (37°C). The resting potential of cardiomyocytes is about 82 mV very close to $E_{K+}$, but a bit less negative because of a weak influence of $Na^+$. Therefore, the $E_m$ is more accurately determined by the Goldman-Hodgkin-Katz equation [equation 2].

$$E_m = \frac{RT}{z_x F} \ln\left(\frac{\sum_N^i P_{X^+}[X^+]_e}{\sum_N^i P_{X^+}[X^+]_i} + \frac{\sum_M^j P_{Y^-}[Y^+]_e}{\sum_M^j P_{Y^-}[Y^+]_i}\right) \qquad [2]$$

Where $X^+$ and $Y^-$ represent monovalent cations and monovalent anions respectively and $P$ is the correspondent permeability. At rest, the permeability of $Ca^{2+}$ and $A^-$ is zero, they do not contribute on $E_m$. Thus, the Goldman-Hodgkin-Katz equation [equation 3] of resting is:

$$E_m = \frac{RT}{z_x F} \ln\left(P_{K^+}\frac{[K^+]_e}{[K^+]_i} + P_{Na^+}\frac{[Na^+]_e}{[Na^+]_i} + P_{Cl^-}\frac{[Cl^-]_e}{[Cl^-]_i}\right) \qquad [3]$$

A current is generated by flow of ions. By convention, the direction of current flow is expressed as the direction in which the positive charges are moving. Because the interior of the resting cell is negatively charged, inward currents cause depolarization and are generated when positive ions enter the cell. In resting cells, outward currents cause hyperpolarization, while outward currents that follow depolarization, cause repolarization, and so membrane potential returns to resting value. The ionic currents are described by Ohm's law: $R=E/I$ [15], where $R$ is resistance, $E$ is potential, and $I$ is current flow. It can be written also using the conductance ($g$) that is the reciprocal of membrane resistance, as follows: $g=I/E$. Since there is a pre-existing electrochemical gradient, the current generated by an ion flux ($i_x$) is: $i_x=g_x(E_m-E_x)$, which states that $i_x$ is determined by the conductance of the membrane for the ion ($g_x$)

and the electromotive force that drives the ion across the membrane ($E_m$-$E_x$), which is the difference between the actual transmembrane potential ($E_m$) and the equilibrium potential of given ion ($E_x$). Conductance of some ion channels, voltage-gated ion channels, depend on membrane voltage. When depolarization approaches a critical level, the threshold, the cell responds actively with the opening of voltage-gated ion channels, producing an all-or-none action potential.

### 2.1.5 Action potential

Cardiac AP is a brief change of the membrane potential across the sarcolemma. All cardiomyocytes are electrically synchronized by structures know as gap junctions which allow cell to cell action potential propagation [16]. It is possible to identify two main types of cardiac muscle cells:

- working cells, in which force generation (contraction) is the principal aim;
- autorhythmic (pacemaker) cells, specialized for initiating and conducting the APs to the working cells.

The action and resting $E_m$ of these two kinds of cells are deeply different. The working cells have an action potential composed of 5 phases (see figure 7).

- Phase 0 is the phase of rapid depolarization due to an intense inward $Na^+$ current. The opening of the channels is voltage-dependent and triggered by depolarization but a time-depending closing mechanism generates a transitory current with rapid kinetics. This current is biphasic with a rapid inward component due to $Na^+$ and a slower outward one activated by $K^+$. Indeed, also the $K^+$-channels open after depolarization with a slower kinetics.

- Phase 1 is the phase of rapid repolarization. The current responsible for this phase is $I_{to}$. This is characterized by a rapid outflow of $K^+$.
- Phase 2, is known as plateau phase. The $E_m$ remains almost constant, because the current density during this phase is smaller than depolarization and repolarization phases of the AP. Moreover, several currents are involved in this phase. One of these, is slow and inward, activated by $Ca^{2+}$ L type channels, also known as DiHydroPyridine Receptor (DHPR). This inward current opposes several repolarizing $K^+$ currents. Indeed, this static phase originates from the balance of the two forces.
- Phase 3 is the phase of rapid repolarization that restores the $E_m$ to its resting value. The currents involved are: $I_{Ko}$ delayed rectifier and $I_{K1}$. $I_{Ko}$ in the cardiac action potential can be resolved in $I_{Kur}$, $I_{Kr}$ and $I_{Ks}$, three small currents. $I_{K1}$, cardiac inward rectifying potassium current stabilizes the resting $E_m$ and is responsible for shaping the initial depolarization and final repolarization of the AP.
- Phase 4, phase of resting potential around -90 mV in normal working cells. This phase is regulated by $I_{K1}$ which prevents depolarization of working cardiomyocytes before a new AP.

The characteristic of the heart to own autorhythmic cells (pacemaker cells) inside its structure allows it to beat rhythmically without any nervous stimulation. Indeed, $Na^+$ voltage-gated channels open when the membrane hyperpolarizes at the end of a previous AP. Because of this behaviour the current gained the name of funny $I_f$. The net inward $Na^+$ flow through $I_f$-channels causes the slow depolarization over the threshold and avoids getting a membrane resting potential. Another feature of pacemaker cells is the presence of a transient $Ca^{2+}$ current, $I_{CaT}$. $I_f$ together with $I_{CaT}$ depolarize the cell until $I_{CaL}$ becomes active and pacemaker's rising phase starts. The falling phase is driven, as in working cells, by $K^+$ efflux coupled with closure of the L-type $Ca^{2+}$ channels. At the end of an AP, the slow closure of $K^+$ channels occurs at negative potential values. Therefore, the polarizing effect of $K^+$ efflux is restrained, promoting depolarization and a new AP.

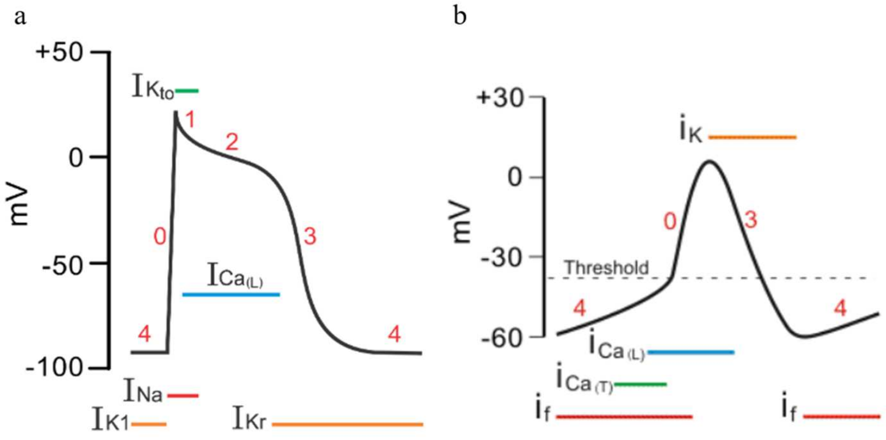

***Figure 7: Cardiac action potential.*** ***(a)*** *Scheme depicting the working cell action potential and* ***(b)*** *pacemaker action potential. In both, the currents involved at each phase of AP are shown. From* [17].

## 2.1.6 Action potential propagation

Cardiomyocytes are joined together with connections in series at specialized structures known as intercalated discs, where gap-junctions allow almost totally free diffusion of ions. Thus, the wave of AP depolarization proceeds via gap junctions and depolarizing current spreads from one cell to the next, bringing $E_m$ in the subsequent cell beyond the threshold for an AP. This wave of AP depolarization is defined by passive depolarization and spreads to the gap junctions (carried mainly by $K^+$ ions), causing the downstream regions to depolarize. Current flow in the reverse direction occurs in the extracellular space (where $Na^+$ and $Cl^-$ carry the charge). This current charges up the membrane capacitance to depolarize the downstream membrane without ions passing. Thus downstream membrane is being depolarized passively. This passive depolarization can bring the neighbouring membrane closer to threshold to trigger an AP. This passive current shows no refractoriness and conduction in both directions. An AP would also propagate in both directions from an initial focal depolarization. However, if Na channels are refractory (due to recent inactivation) retrograde AP is prevented. The ability of the membranes to propagate passive depolarization is extremely important in determining the rate and fidelity of the wave of excitation that spreads through the heart. In fact, if the active zone depolarizes faster, reaching more positive $E_m$, this will spread more rapidly and further to excite downstream regions with a faster conduction velocity. This is partly why atrial and ventricular conduction are much faster than in the SA and AV node. The cellular geometry and characteristics, especially resistance, also play a big role (see figure 8). As the passive current proceeds down the cell and across gap junctions a limiting factor in how far it will reach is how easily it flows longitudinally vs. across the membrane. Thus if the membrane resistance ($R_m$ in $\Omega$-$cm^2$) is high compared to the longitudinal resistivity ($R_i$ in $\Omega$-cm) more current will stay intracellular and charge membrane capacitance further downstream. $R_i$ also gets smaller with increasing cell diameter. The usual quantitative measure of how well passive current spreads along the fibre is the space or length constant $\lambda = (\text{radius} \times R_m/(2R_i))^{1/2}$ which is on the order of 2 mm in cardiac muscle. This means that at one point in time it takes 2 mm for the impact of a local active depolarization to decay to 37% of its peak value. More generally $E_m$ at a distance x from the point where it is $V_0$, is given by $V_x = V_0e^{-x/\lambda}$. While external resistivity ($R_0$) should also be added to $R_i$ in the $\lambda$ equation, its value is usually small in comparison to

$R_i$. Thus large diameter cells with many gap junctions and high $R_m$ would have the largest space constant and be best at high propagation velocity.

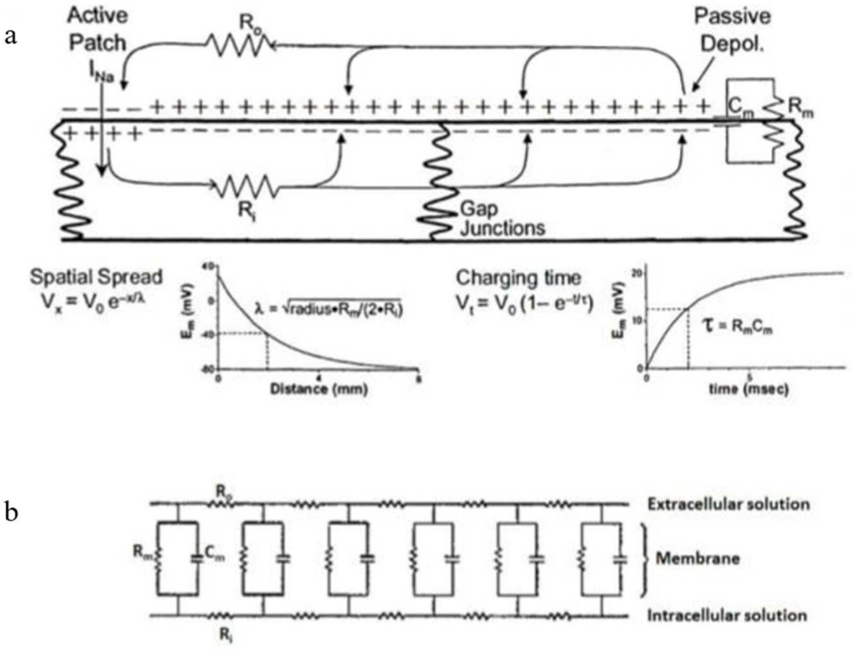

***Figure 8: Propagation of depolarization in cardiomyocytes. (a)*** *Inward ionic current ($I_{Na}$) in the active patch at left causes passive spread of depolarization longitudinally through resistance ($R_i$ and $R_0$) which includes gap junctions. The flow of positive charge (K ions) down cell can charge the membrane capacitance ($C_m$) and leak out via Rm (K channels). The degree and rate of spatial spread are dictated by the length constant ($\lambda$) and time constant ($\tau$) as indicated in insets. Technically $\lambda$ depends on $R_i$+$R_0$ but $R_0$ is usually small in comparison to $R_i$ and can be neglected. Insets show expressions for passive spatial and temporal $E_m$ spread.* ***(b)*** *A simplified equivalent circuit of myocardial tissue. This same cable model can be extended to the transverse and depth dimensions in the real heart, and space constants differ in different directions and have been calculated. From [18].*

Indeed, these factors contribute directly to the slow propagation in AV nodal cells (small diameter) and the very high rates of propagation in Purkinje fibers which have high dimeters (large diameter and small $R_i$) and many gap junctions (lowering $R_i$). The membrane capacitance ($C_m$) is also important in determining the time constant ($\tau$=$R_mC_m$) for changing up the membrane to AP threshold. The equation describing this charging at time t is $V_t = V_0$ (1-e-t/$\tau$). Thus, smaller $\tau$ values will enhance propagation velocity. The heart is normally well tuned in terms of its propagation network, so that APs are activated in all cells in a progressive and synchronized manner.

## 2.2 Excitation-contraction coupling

This section explains the physiological process that translates an electrical stimulus into a mechanical response, called the excitation-contraction coupling (ECC).

### 2.2.1 Entry, release and recovery of $Ca^{2+}$

$Ca^{2+}$ is an intracellular second messenger involved in regulating several different biological phenomena and has got a particular importance in cardiac physiology. In addition to its role in cardiac electrical activity via $I_{CaL}$, $Ca^{2+}$ is essential in ECC by triggering $Ca^{2+}$ release from sarcoplasmic reticulum (SR) and by activating myofilaments for contraction. In fact, $Ca^{2+}$ entry through DHPR causes a massive release of $Ca^{2+}$ from SR through ryanodine receptor (RyR) 2 [19]. This mechanism is called calcium induced calcium release (see figure 9). $I_{CaL}$ is the main trigger for SR $Ca^{2+}$ release and is characterized by a $Ca^{2+}$ dependent inactivation providing a negative feedback that limits $Ca^{2+}$ entry and therefore depolarization too [20, 21].

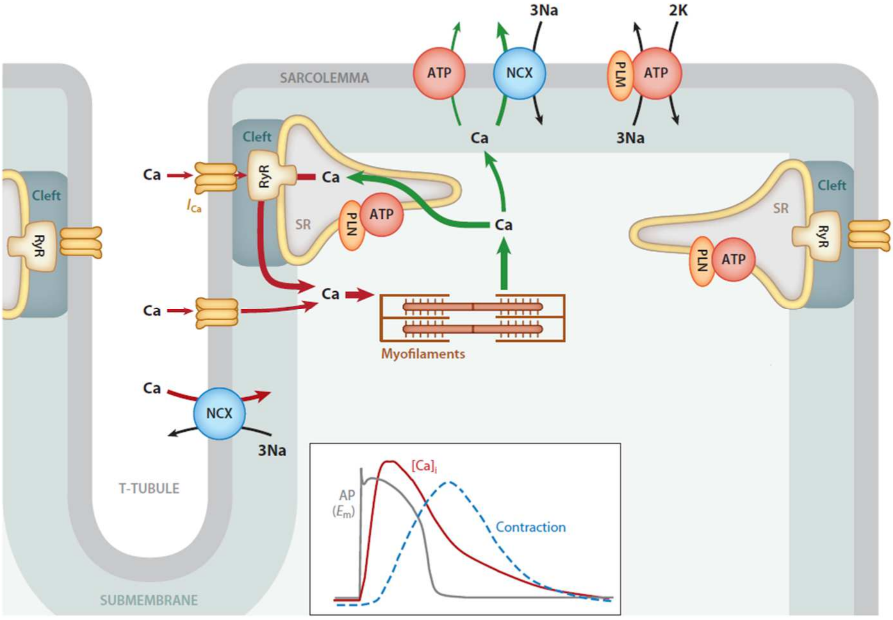

***Figure 9: $Ca^{2+}$ induced $Ca^{2+}$ release in a cardiomyocyte.*** *$Ca^{2+}$ entry via $I_{CaL}$ activates SR $Ca^{2+}$ release via the RyR, resulting in myofilament activation. SR $Ca^{2+}$ uptake via the SR Ca-ATPase [modulated by phospholamban (PLN)] and extrusion via NCX allow for relaxation. The cleft region where SR is juxtaposed to the sarcolemma is shown, as is the submembrane space, where $[Ca^{2+}]$ may differ from bulk $[Ca^{2+}]_i$. Arrows indicate ion translocation paths and $Ca^{2+}$ supply to (red) and removal from (green) the myofilaments. Modified from* [22].

When a DHPR opens, local $[Ca^{2+}]_i$ rises and triggers RyRs that increasing further $[Ca^{2+}]_i$. This activates myofilaments that are the end effector of ECC [23]. The strength of twitch depends on SR $Ca^{2+}$ release, which in turn depends on SR $Ca^{2+}$ content and the extent of the $Ca^{2+}$ trigger [24]. After each contraction, $[Ca^{2+}]_i$ must decrease, so that cardiac cycle is enabled again. There are two main mechanisms to reduce $[Ca^{2+}]_i$: SR $Ca^{2+}$-ATPase (SERCA) and sarcolemma $Na^+/Ca^{2+}$ exchanger (NCX). The first pumps $Ca^{2+}$ back into the SR consuming

ATP, the latter extrudes the cation in the extracellular space, exploiting the electrochemical gradient of $Na^+$, with a stoichiometry of 3Na:1Ca [25].

### 2.2.2 Myofilaments and $Ca^{2+}$-dependent activation

The smallest contractile unit of muscles is the sarcomere, constructed of specialized proteins called myofilaments. There are five recognizable bands within a sarcomere that give cardiac muscle its striated appearance (see figure 10). The boundaries of a sarcomere are delimited by Z-lines that are adjacent to the I-band. Following the I-band is the A-band that includes in its centre a paler region called H-zone. Inside the H-zone is a thin darker structure, called the M-line. The striated organization of the sarcomere corresponds to the presence of specific proteins involved in muscle contractile properties. The sarcomere comprises three kinds of filaments, titin, the thin and the thick filaments. The thin filaments contain F-actin, which is a polymer of G-actin monomers and is the main component of the I-band, tropomyosin and the troponin complex. In the complex, troponin C (TnC) is the $Ca^{2+}$ binding protein, troponin I (TnI) inhibits contraction and troponin T (TnT) binds to tropomyosin. Actin filaments interact with α-actinin at the Z-line and extend into the A-band. The thick filaments are constituted by myosin, which extents in the A-band and its position is guaranteed by the bond with titin. In resting cardiomyocytes, TnI has an inhibitory role on tropomyosin preventing actomyosin interactions. When intracellular $Ca^{2+}$ binds TnC, it entails a conformational change in the troponin complex, unlocking tropomyosin from actin. As a result, myosin actin-binding site is revealed and actomyosin interaction can occur with cross-bridges formation [26] (see figure 11).

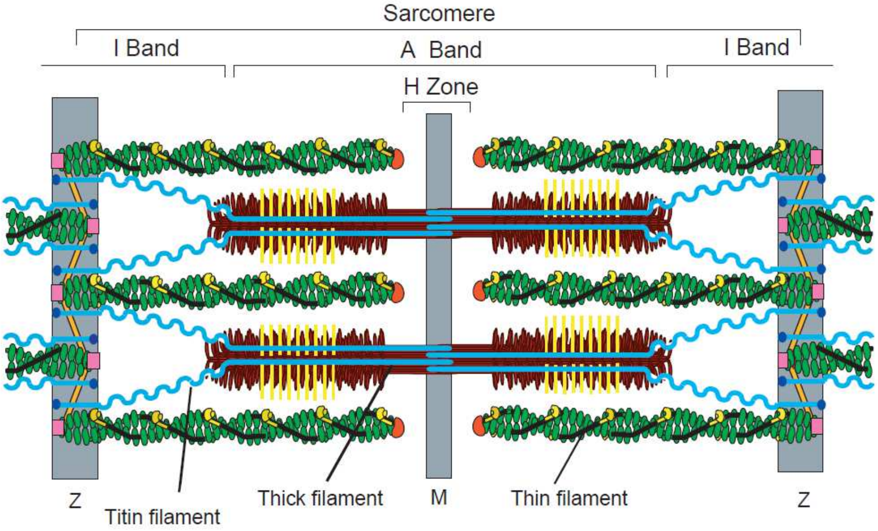

***Figure 10: Structure of cardiac sarcomere.*** *Representation of the major proteins of the sarcomere and of the basis organization of the sarcomere. The role of each of these proteins are critical to appreciate function of the heart. Thin filaments composed of actin (green) are anchored at the Z-line and form transient sliding interactions with thick filaments composed of myosin molecules (red). The M-line, I-band and A-band are anatomical features defined by their components (actin, myosin and cytoskeletal proteins) and appearance in polarized light. Titin (light blue) connects the Z-line with the M-line and contributes to the elastic properties and force production of the sarcomere through its extensible region in the I-band. Coordinated shortening of the sarcomere creates contraction of the cardiomyocytes. From* [27].

Myosin is a molecular motor consisting of two heavy chains (MHC) and four light chains (MLC, two structural light chains and two regulatory one). In detail, MHC consists of a globular motor domain (head), which has an ATPase activity and interacts with actin, a neck and a tail domain. Myosin neck binds to myosin light chain 1 (MLC-1) and 2 (MLC-2) that contribute to the regulation of the contractile function and to the stiffness of the neck region. Cross-bridges formation occurs in a cooperative manner, allowing a rapid thin filaments activation and force development [28]. Upon ATP hydrolysis, the myosin head undergoes a change in the binding angle resulting in the motion of thick filaments [29, 30].

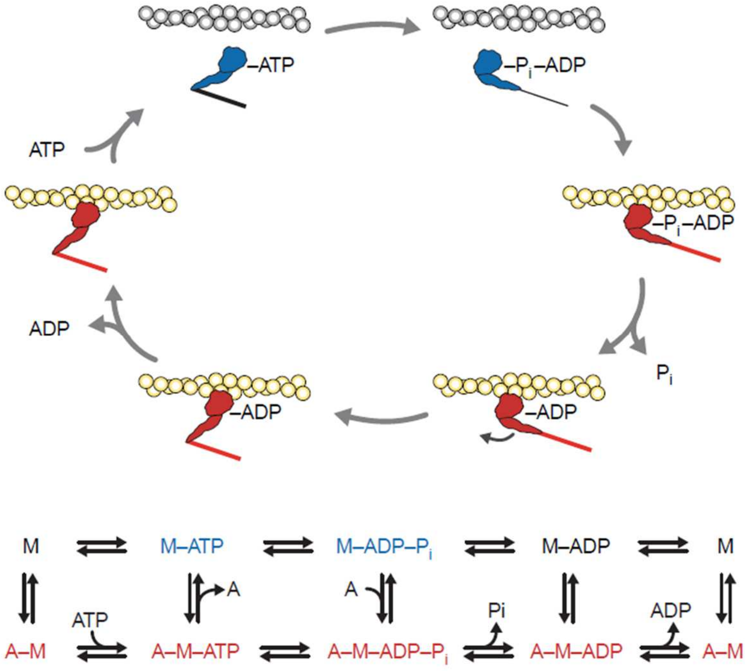

***Figure 11: Cross-bridge cycling.*** *Above, schematic diagram showing the predominant states of the actin–myosin ATPase cycle and the state of the lever arm in each state. Actin-bound states are represented in red; dissociated states are shown in blue. Myosin binds to ATP, hydrolyses it to ADP–Pi and releases the products in the absence of actin, but phosphate release is very slow. Actin binding myosin accelerates phosphate release, which is thought to precede the working stroke. ADP release is the slowest of the strongly bound rates, and is thought to limit velocity. Rebinding of ATP causes dissociation from actin and starts the cycle again. Below, scheme of the binding, hydrolysis, and dissociation of myosin with the energy molecule ATP. From* [31].

## 2.3 Morpho-functional alteration in HCM

HCM is a genetic heart disease characterized by left ventricular hypertrophy, which develops in the absence of other inciting factors, such as augmented hemodynamic load or infiltrative disorders. The most common morphologic pattern is an asymmetric LV hypertrophy (see figure 12) which involves mainly the interventricular septum. However, other configurations of hypertrophy cannot be excluded and are not closely related to the graveness of the disease [4].

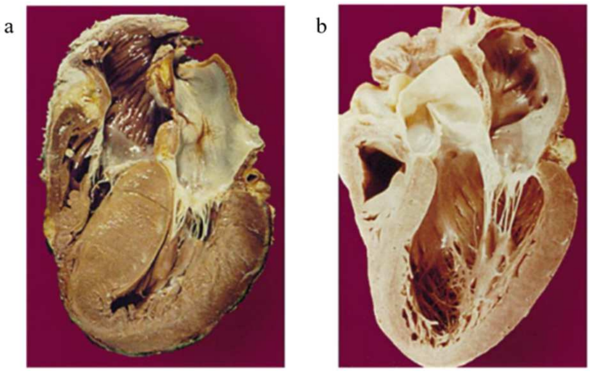

***Figure 12: Patterns of cardiac remodelling.*** ***(a)*** *Robust increase in LV wall thickness of HCM in comparison to* ***(b)*** *the normal LV wall thickness of the healthy heart* [32].

A particular histological feature is disorganization of LV myocardial architecture, composed by hypertrophied cardiomyocytes with bizarre shapes and multiple intercellular connections often arranged in chaotic alignment at oblique and perpendicular angles (see figure 13). Cellular disarray may be widely distributed, occupying substantial portions of LV wall (average 33%). Another characteristic feature is fibrosis.

Indeed, with premature death of hypertrophic cardiomyocytes, the cardiac fibroblasts and associated extracellular matrix increase and further contribute to the distortion in cardiomyocytes architecture [5].

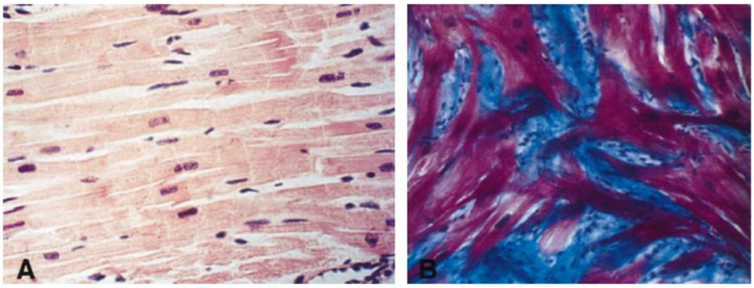

***Figure 13: Histopathology of HCM.*** ***(a)*** *The normal architecture of healthy ventricular myocardium shows orderly alignment of cardiomyocytes with minimal interstitial fibrosis.* ***(b)*** *Marked enlargement and disarray of cardiomyocytes (red) with increased interstitial fibrosis (blue) is evident in HCM. Stains: [a] hematoxylin and eosin; [b] mason trichrome* [32].

Disorganized cellular architecture and expanded interstitial fibrosis, probably serve as arrhythmogenic substrates predisposing to electrical instability. This substrate is likely the source of primary ventricular tachycardia and ventricular atrial fibrillation, which appear to be the predominant mechanisms of sudden death. These mechanisms are in association with triggers intrinsic to the disease process, namely, myocardial ischemia, systemic hypotension and supraventricular tachyarrhythmias. The prevalence of the disease is approximately 1:500 in Caucasian young adults. The pathophysiology of HCM shows a remarkable variability in disease development, age of onset and graveness of the symptoms. Indeed, many patients have a clinical history without any symptoms, whereas others display severe consequences until heart failure, malignant arrhythmia or sudden death. Over 900 mutations in more than 20 genes are identified as cause of

HCM, all with an autosomal dominant (A/D) pattern of inheritance. Nevertheless, the disease-causing genetic background is clarified in only 45-60 % of cases [33]. Most the known mutations involve components of contractile mechanism, establishing the paradigm that HCM is a sarcomere disease. Mutations in the genes encoding cardiac β-myosin heavy chain (β-MHC, MYH7), cardiac myosin binding protein C (cMyBPC, MYBPC3), cTnT (TNNT2) and cTnI (TNNI3) are the most prevalent and in aggregate, account for over 80% of HCM.

- β-MHC is an abundant protein that has two functional domains: the head domain binds ATP, contains the ATPase activity and the actin-binding domain to form the action-myosin complex crucial for force generation. In general, MYH7 mutations have been associated with a gain of function, resulting in increased actin-dependent ATPase activity, in vitro sliding velocity and force production [34, 35].
- The function of cMyBPC is unknown, but it is thought to provide structural integrity to the sarcomere, play a role in sarcomeric assembly [36], and may modulate myosin ATPase activity and cardiac contractility in response to adrenergic stimulation [37]. Mutations in MYBPC3 have been characteristically associated with gain of function and late-onset disease [38].
- cTnT links the troponin complex to tropomyosin, thus playing a central role in the regulation of contraction. The disease caused by TNNT2 mutations were associated with gain of function and an increased risk of sudden death despite only modest hypertrophy [39, 40].

Each mutation has somewhat different effects on myofilament properties, though all mutations can be predicted to result in [41]:

- impaired relaxation;
- reduced diastolic compliance;

- reduced contractile reserve;
- preserved systolic function under baseline conditions;
- cardiac dysfunction under inotropic stimulation.

Therefore, it is of fundamental importance to understand what the relationship between function and structure is to be able to comprehend the mechanisms underlying the correlation between electro-mechanical dysfunctions and structural alterations.

## Chapter III

# Imaging techniques in cardiovascular research

The heart is a complex organ characterized by a close correlation between function and structure, as explain in chapter II. This chapter describes the microscopy techniques utilized to correlate electro-mechanical dysfunctions with structural alterations.

## 3.1 Functional imaging

Functional imaging is used to study cardiac function. In particular, by combining a wide field system with voltage-sensitive dyes it is possible to investigate action potential propagation at the whole heart level.

### 3.1.1 Wide field microscopy

Wide field fluorescence microscopy is common technique to obtain both topographical and dynamical information. It is based on an illumination of the entire sample. A light emitting diode (LED) giving out pure white light is usually used as a source of light. The excitation light beam enters an optical system consisting of two converging lenses called tube lens and objective. To deflect the light toward the objective, a dichroic mirror is used which reflects the wavelengths of the excitation light while letting those of fluorescence (see figure 14) transmit. Excitation light illuminates the whole sample which is located at the focal plane of the objective. The emitted fluorescence is collected by the objective, transmitted through the dichroic mirror towards a relay lens arrangement that reconstructs the image.

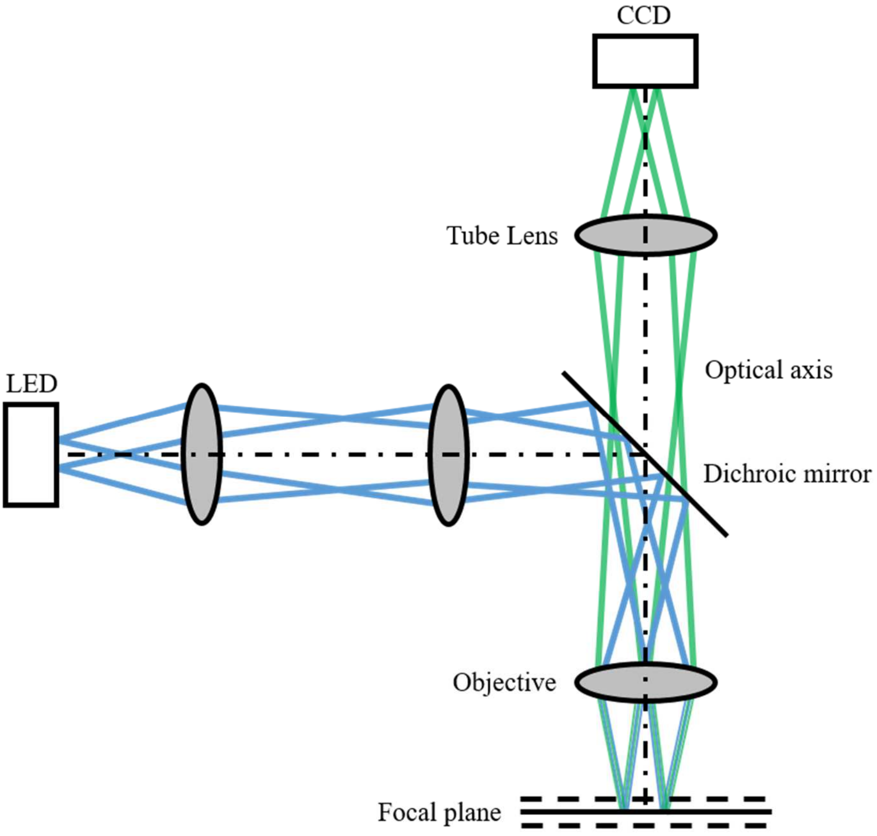

***Figure 14: Scheme of a wide field microscope.*** *A LED allows a simultaneous illumination of the entire sample which is located on the focal plane. The fluorescence is collected by an objective, transmits through the dichroic mirror, towards the tube lens that reconstructs the image. The emitted light arrives at the detector and it is detected by a camera (usually a CCD camera).*

The light, before arriving at the detector, is filtered using a filter that lets through only the wavelength corresponding to the emission of the dye, in order to eliminate the excitation light. Light is detected by a camera (usually Charged Coupled Device (CCD) camera) and the image is reconstructed by considering all the fluorescent spots in the sample. Thus both the illumination and detection of light covering the whole visual field of the microscope objective is achieved simultaneously.

### 3.1.2 Voltage-sensitive dyes

The electrical activity may be considered the most particular characteristic of excitable cells and several efforts have been done to create sensors capable of following the membrane potential changes. There are important technical problems that need to be overcome to measure a membrane potential variation. For instance:

- The electrical field decreases exponentially with distance from the membrane, meaning that the voltage sensor needs to be either physically attached or inside the membrane, to probe the phenomenon. Moreover, the membrane is an active cellular component and its electrical properties may vary with the insertion or attachment of chromophores.
- The extracellular membrane is not the only membrane present in the cell. Fluorescent molecules need to be localised exclusively at the plasmalemma. Since intracellular membranes are not involved in electrical activity any dye attached to them would only increase background noise.
- Compared to the bulk cytoplasm, the membrane is very thin and the number of chromophores in that volume is limited. It means that only a few photons can be emitted, reducing the signal that gets over photon shot noise. Increasing the light source power or the time and area of illumination would improve the signal but

might exert photodamage and eventually jeopardise the biological sample.

Once the afore-mentioned problems are overcome, effective voltage imaging can be achieved via exploiting different physicochemical features of molecules. One of the most used method to generate voltage-sensitive indicator is the synthesis of organic chromophores that bind to the outer cellular membrane. In particular, hemicyanine dyes attract attention because they exhibit electrochromism as voltage-sensing mechanism [42]. The electrochromic mechanism is a direct interaction of the electric field with the dye and does not require any movement of the chromophore (see figure 15). This means that the dye rapidly responds to the membrane potential variations.

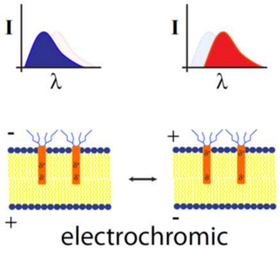

***Figure 15: Electrochromic mechanism.*** *In this phenomenon, the membrane potential changes the relative energy of the ground and excited states of the chromophore altering the excitation and emission wavelength. Modified from* [43].

## 3.2 Structural imaging

Structural imaging is used to investigate cardiac structure. However, to obtain 3D reconstruction at micron scale resolution, advanced optical microscopies are required: serial two-photon sectioning (STP), exploiting non-linear microscopy, and LSM.

### 3.2.1 Non-linear microscopy

There are different ways to perform non-linear microscopy, but the most common in biology is two-photon excitation (TPE). It consists of two photons, each with half of the energy, interacting with the fluorescent molecule in a quasi-simultaneous fashion (in $\approx 10^{-16}$ s). Absorption of a photon by the fluorescent molecule occurs only when the quantum energy of the photon matches the energy gap between the initial and final states (quantized energy states). In TPE, each photon provides only half of the required energy and by itself promotes a virtual energy state. If another photon strikes within this time window the energy of the two photons can be summed to allow an energy state transition (see figure 16). Halving the energy by two implies that $\lambda$ must be doubled (from the photon energy equation) and therefore the wavelengths used are redder compared to single photon excitation. This is an advantage when dealing with biological samples, because near-infrared light penetrates deeper into scattering tissue and is less phototoxic. Moreover, the multiple-photon requirement for fluorescence excitation implies that the generated fluorescence depends non-linearly on the number of photons per time and $cm^2$ [44], i.e. $P \propto I^n$, where $P$ is the probability, $I$ is the intensity of the photon flux, and $n$ is the number of photon required for excitation. Thus, for TPE the formula is: $P \propto I^2$. This means that to generate sufficient signal, the excitation light has to be concentrated in space and time. By focusing a laser beam through a high numerical aperture (NA) objective it is possible to spatially limit the TPE probability at the focal plane. Away from the focus, the TPE probability drops off rapidly so that elsewhere in the sample TPE is a very unlikely event [45]. Concentration in the time domain requires the use of lasers that emit short pulses (typically 100 fs at about 80-100 MHz) with high peak intensities. The lack of out-of-focus excitation in non-linear microscopy further reduces photodamage and thus increases tissue viability. Moreover, in the infrared light biological tissues are more transparent allowing to reach a high imaging depth. Indeed, the maximum depth achievable in living animals is ≈800 μm [46]. However, it drastically decreases in fixed samples (300 μm) [47]. That limits the imaging analysis of high-volume samples such as the whole mouse heart.

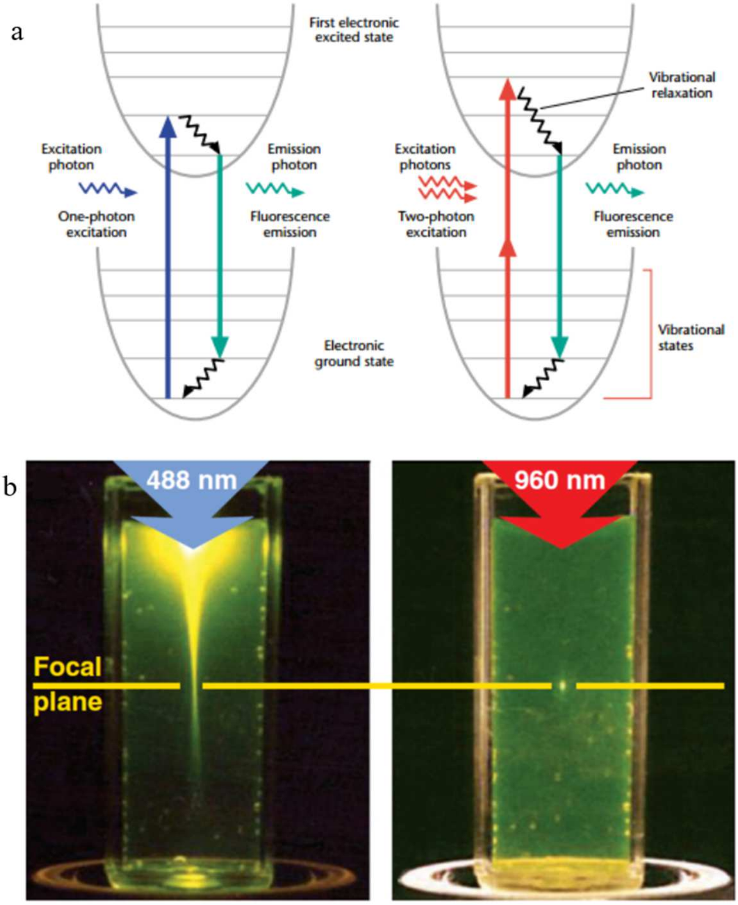

***Figure 16: Localization of fluorescence by two-photon excitation.*** ***(a)*** *Jablonski diagram of one-photon (left) and two-photon (right) excitation, which occurs as fluorophores are excited from the ground state to the first electronic states. One-photon excitation occurs through the absorption of a single photon. Two-photon excitation occurs through the absorption of two lower-energy photons via a virtual state. After either excitation process, the fluorophore relaxes to the lowest energy level of the first excited electronic states via vibrational processes. The subsequent fluorescence emission process for both relaxation modes is the same. From [48].* ***(b)*** *On the left, single-photon excitation of fluorescein by focused 488 nm light (0.16 NA). On the right, two-photon excitation using focused (0.16 NA) femtosecond pulses of 960 nm light. Excitation volume is localized by the two-photon transition. From [45].*

### 3.2.2 Serial sectioning method

The growing need to obtain whole-organ reconstruction has led to the development of new approaches that combine different techniques. One method consists in obtaining automatic microscopes for large datasets analysis based on the integration of imaging and tissue sectioning. One of these systems is STP tomography [49]. It combines TPFM with the serial sectioning of the sample. These methods are characterized by the presence of automated high-throughput instrumentation. A motorized platform under the microscope objective moves the sample allowing top-view mosaic imaging. Before every cycle of acquisition, a sectioning step is performed followed by a mechanical removal of the imaged tissue. In STP, the sample is fixated with paraformaldehyde. This allows for embedding the tissue in agar and performing the sectioning with a vibratome (see figure 17). This approach does not require specific efforts in preparing the sample, however, it presents a disadvantage. Due to tissue deformations introduced by slicing, imaging cannot be done near the tissue cuts. It is preferable to image 50 μm below every cut. Moreover, since the tissue is fixed, the imaging penetration depth achievable with the TPFM is a few hundreds of μm. In addition, to obtain the complete reconstruction of large volumes, a long acquisition time is required (days up to weeks). Furthermore, this technique intrinsically destroys the sample during imaging. To overcome these downsides another approach, that does not require sample cutting, can be used: LSM.

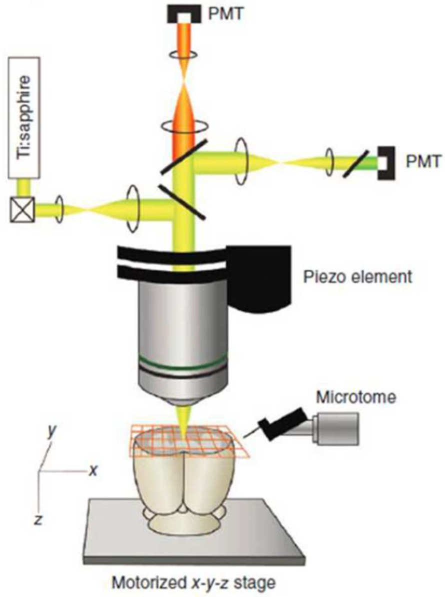

***Figure 17: Serial sectioning:*** *STP tomography, a two-photon microscope is used to image the focal plane of the sample, afterwards a microtome sections off the imaged tissue. A piezo objective scanner can be used for z-stack imaging. From* [50].

## 3.2.3 Light-sheet microscopy

LSM is a fluorescence microscopy technique that uses a thin sheet of light to illuminate the specimen, performing optical sectioning [51 - 54]. In detail, during LSM the sample is illuminated with a thin sheet of light confined in the focal plane of the detection objective. The fluorescence emission is collected along an axis perpendicular to the illumination plane (see figure 18). The optical paths of excitation and detection light are decoupled guaranteeing optical sectioning also with low-NA optics (axial resolution is given by the thickness of the light sheet). Moreover, with this approach, fluorophores are excited only at the focal plane of the detection objective, dramatically reducing photobleaching. The detection architecture is similar to the one of wide field microscopy, making the acquisition faster compared with two-photon microscopy. Moving the sample through the light sheet permits to obtain a complete tomography of big specimens. This technique drastically reduces acquisition time and achieves good resolution at high penetration depths. However, it requires the sample to be transparent. To allow imaging at high depths it is necessary to reduce light scattering and make the tissues transparent. This goal can be achieve by homogenizing the refractive index inside and outside the sample by using clearing agents.

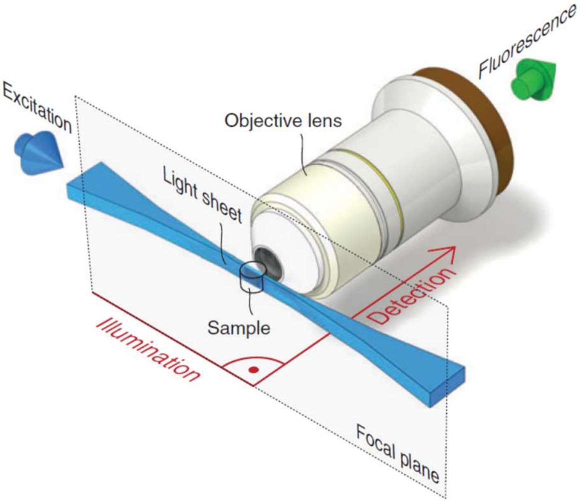

***Figure 18: Fluorescence light-sheet microscopy.*** *In LSM, fluorescence excitation (blue arrow) and detection (green arrow) are split into two distinct optical paths. The illumination axis is orthogonal to the detection axis. A microscope objective lens and common wide field optics are used to image the sample onto a camera (not shown). The illumination optics are designed to illuminate a very thin volume around the focal plane of the detection objective. Many different implementations of this principle exist, however, the most common one is the generation of a sheet of laser light that illuminates the sample in the focal plane from one side. From* [53].

# Chapter IV

# Optical clearing methods

The 3D structure of organs requires volumetric imaging. Different techniques, such as STP and LSM, can be used to investigate organ architecture. They allow 3D reconstruction of large specimens at high resolution; however, they are limited by light scattering that makes imaging problematic. Indeed, light does not propagate well inside tissues. To overcome this limit, samples should be as transparent as possible to improve imaging depth. Many different methods have been developed to clear tissues and reduce scattering. This chapter describes the mechanism of light scattering and the clearing techniques that make tissues transparent and, therefore, are used for large volume 3D reconstruction.

## 4.1 Scattering and refractive index

Scattering is the event that occurs when light rays encounter irregularities in the propagating medium and are diverted from their straight path [55]. Clear samples are necessary to assure that all wavelengths pass through the tissue reducing scattering. Scattering happens when the refractive index between different regions of the sample is heterogeneous. This event limits the penetration of light into tissue when the variation of the refractive index is similar to the wavelength used for imaging [56 - 58]. The refractive index must be homogenized inside and outside the sample to reduce scattering and to make the tissue transparent (see figure 19).

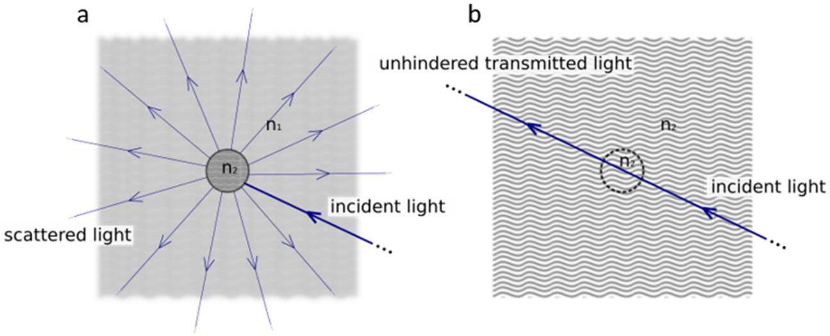

***Figure 19: Light scattering and refractive index matching.*** ***(a)*** *Scattering occurs when the refractive index between different regions of the sample is heterogeneous ($n_1 \neq n_2$).* ***(b)*** *Scattering is strongly reduced, and light can pass through the tissue when the sample and the surrounding medium have similar refractive indexes ($n_1 = n_2$). From* [59].

## 4.2 Optical clearing methods

In order to homogenize the refractive index and reduce scattering to clear the sample, different approaches have been developed based on organic solvents, high-refractive index aqueous solutions, hyperhydrating solutions and tissue transformation (see figure 20). The first optical clearing method was reported by Spalteholz in 1914 [60]. His approach was based on two steps: a dehydration step using ethanol, and a clearing step with high refractive index solvents. Subsequently, this scheme has been reintroduced by Dodt et al. [52], using a mixture of benzyl alcohol and benzyl benzoate (BABB, n=1.55) as index-matching solution. Becker et al. [61] investigated dehydration with tetrahydrofuran (THF) and clearing in dibenzyl ether (DBE, n=1.56), obtaining better results in fluorescence preservation and sample transparency. This technique was called 3DISCO [62].

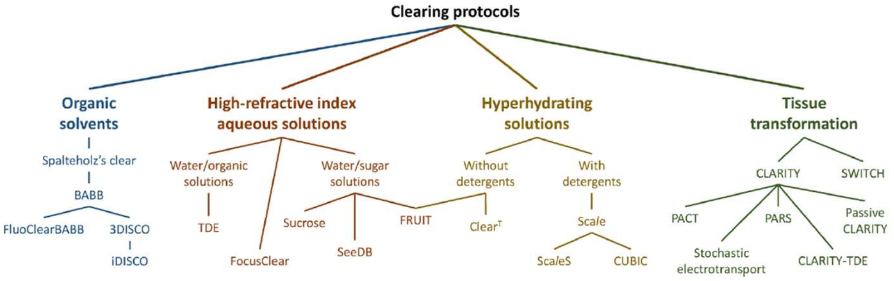

***Figure 20:*** *The classical taxonomy of clearing methods. From* [10].

Afterwards, the iDISCO method [63] combined the protocol with whole tissue immunostaining, avoiding the necessity of protein fluorescence preservation. Another improvement on BABB clearing, based on pH control and different dehydration agents, is FluoClearBABB [64]. All these methods are used because they guarantee high transparency, they are easy to perform and very fast, and can be applied to different tissue types [52]. However, they have some disadvantages that limit their applicability. They lead to a fast protein fluorescence quenching (few days), tissue alteration and shrinkage [61], moreover most of them have the capacity to dissolve glues used in the construction of objective lenses. For these reasons other approaches have been studied based on aqueous solutions with high refractive index. Some methods exploit high concentration solutions of sugars, such as sucrose ($n=1.44$) [65] or fructose (SeeDB and FRUIT, $n=1.48$) [66, 67]. Sugars are not toxic, compatible with protein fluorescence and do not alter tissue structure. However, aqueous techniques do not clear as well as the organic methods. Moreover, highly concentrated sugar solutions are difficult to manage due to their high viscosity and require long incubation times. Alternative approaches, to solve this problem, are based on organic compounds like 2,2′-thiodiethanol (TDE, $n=1.42$) [1, 68, 69], and commercial solutions (FocusClear™, $n=1.45$). Moreover, there are methods based on protein hyper-hydration with urea, the first to be developed is the Scale method (n=1.38) [70]. A further development of Scale is ScaleS [71]. Other protocols exploiting hyper-hydration are ClearT, (n=1.44) [72] and CUBIC (n=1.48) [73, 74]. These techniques lead to fluorescence preservation, but, they lead also to tissue swelling and subcellular structure alterations, moreover, urea denatures proteins, hydrates them, and decreases the overall refractive index of the tissue.

## 4.3 Tissue transformation

Tissue transformation techniques try to stabilize the protein content of the sample by cross-linking proteins to a gel mesh. The pioneer methodology in the field has been CLARITY [3]. The method removes cell lipid bilayers and allows light and macromolecules to penetrate deep into the tissue, permitting 3D imaging and immune-histological analysis. To provide structural integrity and retain biomolecules, CLARITY transforms the tissue into a nanoporous hydrogel-hybridized lipid-free form. The procedure is divided into four steps (see figure 21). The first step consists in animal perfusion at 4°C with the hydrogel monomers (acrylamide and bis-acrylamide), paraformaldehyde and the thermally triggered initiator. In the second step, tissue incubation at 37°C permits to obtain the hybridization of the tissue with the hydrogel. This construct physically supports tissue structure and chemically incorporates biomolecules. Lipids extraction is carried out in the third step by electrophoretic tissue clearing (ETC). ETC is based on the active transport of ionic micelles through the tissue. Lipids are incorporated within micelles and removed from the specimen. The hydrogel is highly permeable, which allows immunohistochemistry, facilitating tissue labelling. As a final step, the refractive index matching solution FocusClear$^{TM}$, a very expensive solution, is used to clear the sample.

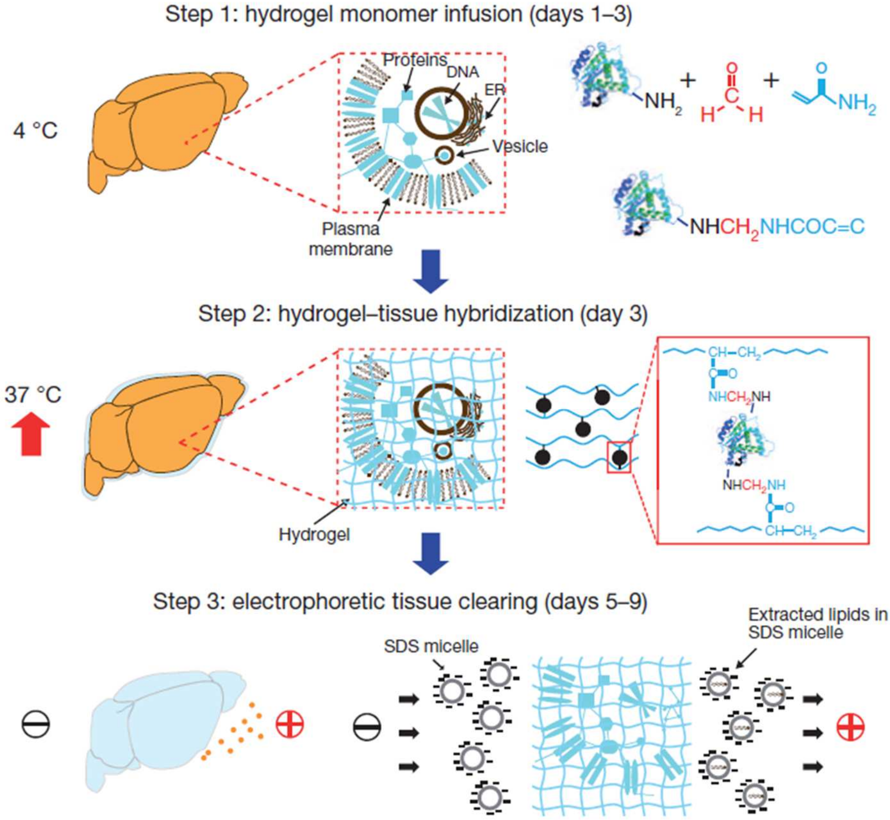

***Figure 21: CLARITY protocol.*** *Scheme showing the different steps of the CLARITY method. The first step consists in the perfusion of the sample with paraformaldehyde (red) and hydrogel monomers (blue). The hydrogel-tissue hybridization occurs in the second step. In the third step, electric fields applied across the sample in ionic detergent actively transport micelles into, and lipids out of, the tissue, leaving fine-structure and cross-linked biomolecules in place. After that, the brain is ready for refractive-index matching and imaging. From* [3].

Similar to this method, another technique called PACT (PAssive CLARITY Technique), that uses a Refractive Index Matching Solution (RIMS) to clear samples [75], was published. Another approach named PARS (Perfusion-assisted Agent Release in Situ) has been developed to achieve whole organ labelling using a continuous perfusion of the sample with immune-histochemical solutions (like antibodies and blocking buffers).

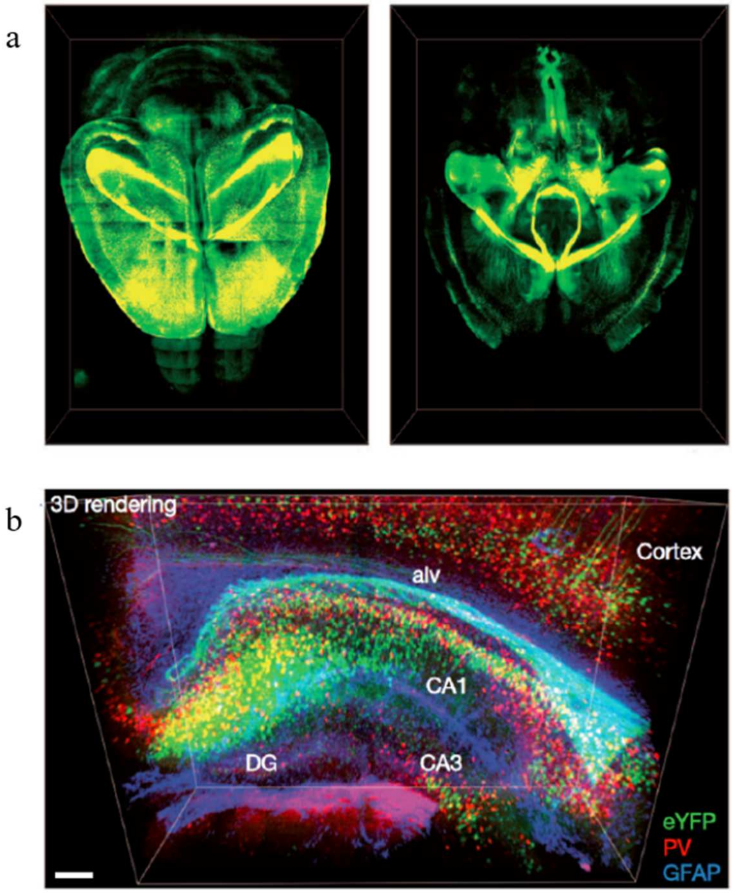

***Figure 22*: *Whole mouse brain imaging.* *(a)*** *Images made with a confocal microscope of a mouse brain after CLARITY hydrogel-tissue hybridization, ETC, and refractive-index matching.* ***(b)*** *Three-dimensional view of mouse hippocampus showing yellow fluorescent protein expressing neurons (green), parvalbumin-positive neurons (red) and astrocytes (blue). Scale bar, 200 μm. Modified from* [3].

Other improvements to the original CLARITY approach include the use of cheaper index matching solutions, such as TDE [1], histodenz [75], or diatrizoic acid [76, 77]. As CLARITY protocols, these methods require a long preparation time (weeks) and complicated procedures, nonetheless, they are attractive because of the high degree of transparency and of the increased sample porosity, which helps whole-mount immunohistochemistry on large portions of tissue (see figure 22). All these protocols have been developed on the brain. Subsequently, some of these have been tried on other organs, like the heart, without obtaining excellent results in clearing (see figure 23), because of the dark red colour typical of muscles that is given by myoglobin presence. Because of the low level of transparency, imaging does not show an outstanding resolution due to light scattering (see figure 24). However, in this thesis work the CLARITY method was used as starting procedure, making some modifications from the original protocol, necessary to obtain an excellent clearing and to be able to perform mesoscopic resolution imaging on mouse and human cardiac samples using two-photon and light-sheet microscopies.

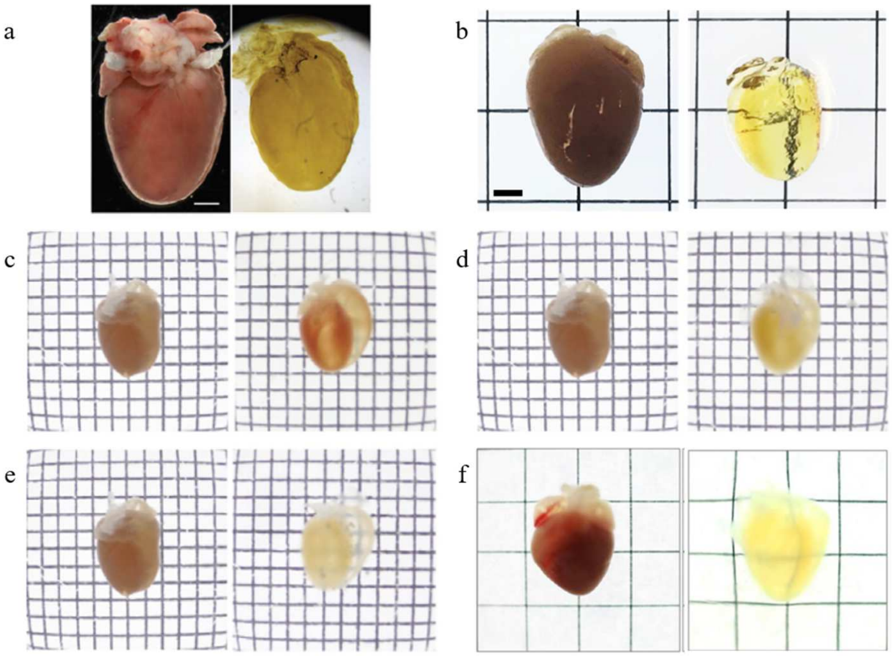

***Figure 23: Different clearing protocols on the heart.*** *Transmission images of whole heart from adult mice after **(a)** BABB, **(b)** iDISCO, **(c)** SeeDB, **(d)** Sca/e, **(e)** CUBIC and **(f)** CLATIRY protocols. These images show the low level of transparency and the shrinkage phenomenon after some clearing processes (BABB and iDISCO). Scale bars (a) and (b) 1 mm. Modified from* [6, 73, 78, 79].

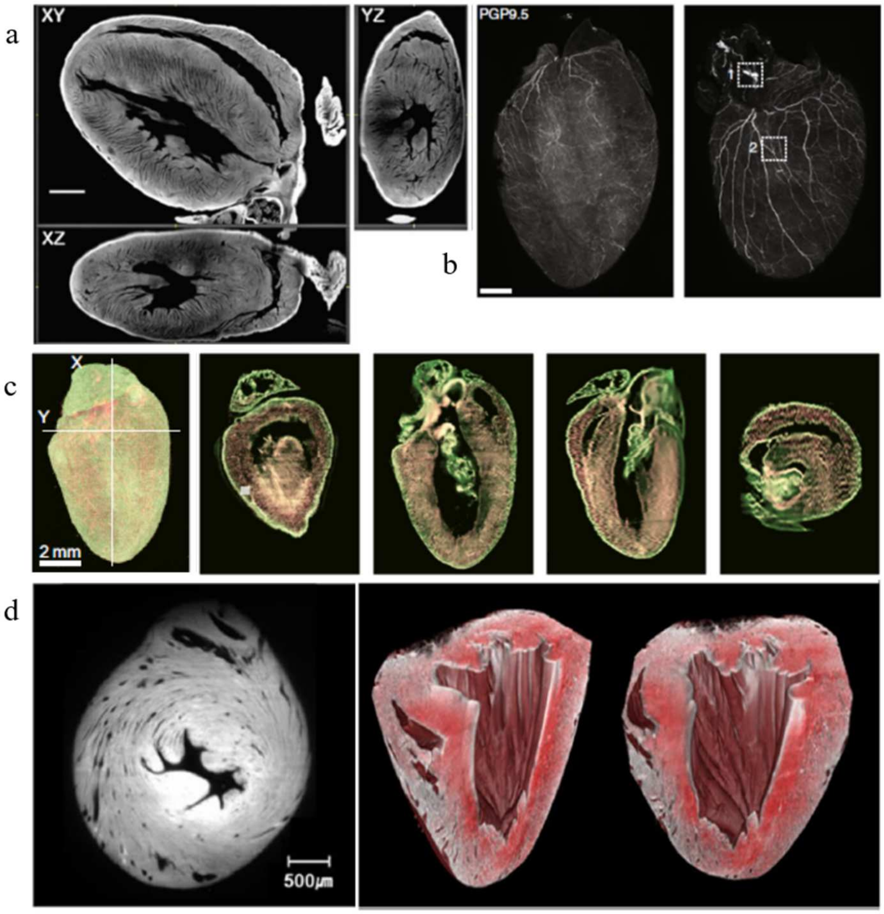

***Figure 24: Whole heart imaging after different clearing protocol.*** ***(a)*** *Orthogonal sections (XY, XZ, and YZ) of the whole heart at the median plane imaged with two-photon fluorescence microscope after BABB protocol.* ***(b)*** *3D confocal projections of the ventral and dorsal side of a cleared heart with iDISCO method.* ***(c)*** *After CUBIC, the reconstituted 3D and section images of a heart were acquired with light-sheet fluorescence microscopy.* ***(d)*** *Light-sheet image of a heart cleared with CLARITY (left). 3D reconstruction of the entire heart from light-sheet images (right). Scale bars (a) and (b) 1 mm. Modified from* [6, 73, 78, 79].

# Part II

## Advanced morpho-functional analysis on ventricular tissue in HCM patients

# Summary

In this thesis work, a mutation in the gene coding for cMyBP-C, that is the most common cause of HCM, was investigated. The E258K-MyBP-C is a highly penetrant missense mutation with poorly understood molecular mechanisms. Mechanics of contraction as well as the energy cost of tension generation were investigated using LV tissue from E258K HCM patients and from donor hearts. Maximal ATPase and isometric active tension were simultaneously measured in permeabilized LV strips. Moreover, to check whether cardiomyocytes disarray, typical of HCM hearts, may have contributed to functional alteration in the HCM preparations, the strips used for mechanical investigations were immunostained, clarified and imaged at mesoscale level. An immunostaining protocol using anti-α-actinin antibody was optimized to visualize sarcomere structure. Then, an advanced tissue clearing method [1] in combination with TPFM was employed to reconstruct the 3D image of the strips at sub-micrometre spatial resolution. A 3D cytoarchitecture analysis tool based on 3D Fourier Transform was developed and applied to determine cardiomyocytes orientation across and along the strips. Both global and local statistics of spatial disarray were derived and correlated to mechanical and energetic data.

# Chapter V

# Biological rationale

HCM is the most common inherited heart disease, with an estimated prevalence of 1:200 [80]. It is characterized by abnormal and asymmetric thickening of the left ventricle, diastolic dysfunction, structural remodeling of the myocardium (i.e. myocyte disarray and myofibril misalignment) and sudden cardiac death. Most genotyped HCM patients harbor mutation in one of the genes coding for cardiac sarcomeric proteins, such that HCM is defined primarily as a disease of the sarcomere [81, 82]. A complex chain of events may lead from molecular defects in sarcomeric proteins to contractile dysfunction and cardiac remodeling of the intact heart. It was previously shown that, mutations both on thick and thin-filament proteins (i.e R403Q, K280N) [83 - 85], primarily increase energy consumption during tension generation (tension cost). Inefficient or excessive ATP utilization for tension development, at the sarcomere level, may have a decisive role in the pathogenesis of HCM disease [86]. The "energy depletion hypothesis" for HCM is supported by several studies both on human heart samples and animal models [84, 87 - 95]. Mutations in MYBPC3, the gene coding for cMyBP-C, together with mutations in myosin heavy chain (MYH7), are the most common cause of HCM [96]. cMyBP-C is a thick-filament associated protein that localizes in the cross-bridge bearing C-zone in the A band of cardiac sarcomere, where it plays important structural and functional roles [97 - 100]. In the last years, a growing number of missense mutations in MYBPC3 have been identified [101]. However, their molecular mechanisms remain controversial. The E258K is a pathogenic missense mutation on the last nucleotide of the exon 6 of MYBPC3, resulting in the substitution of the amino acid lysine for glutamic acid (i.e G>A) at position 258 in cMyBPC [102, 103]. This mutation is highly penetrant and is usually associated with a severe phenotype and a poor prognosis in HCM patients [96].

# Chapter VI

# Methods

The present chapter provides the experimental biological preparation employed in the study and the technique used to perform functional measurements. Moreover, to improve the imaging depth achievable with fluorescence microscopy tissue transparency is paramount. The protocol utilized to clear the sample and the fluorescence microscopy technique used to image it are described below.

## 6.1 Cardiac tissue for functional and structural experiments

The study conforms with the principles of World Medical Association's Declaration of Helsinki for medical research involving human subjects. The experimental protocols were approved by the ethics committee of Careggi University Hospital (2006/0024713; renewed May 2009). Each patient gave written informed consent. All participants were unrelated index patients. HCM diagnosis was by 2D echocardiographic identification of a hypertrophied (≥13 mm), non-dilated LV, in the absence of another cardiac or systemic disease capable of producing that magnitude of ventricular hypertrophy. The study included three patients with Glu258Lys (E258K) missense mutation, referred to surgical myectomy for relief of drug-refractory symptoms related to left ventricular outflow tract obstruction, from the Referral Center for Cardiomyopathies in Florence, Italy. And, two donor patients from

Erasmus Medical Centre, Rotterdam, The Netherlands. After collection in cold cardioplegic solution, surgical ventricular tissues from HCM and donor patients were quickly frozen in liquid nitrogen and stored at -80 °C.

## 6.2 Fibers preparation

Ventricular muscle strips (n=21 HCM and n=25 donor) were dissected parallel to the long axis of the fibres in cold relaxing solution (see table 2) under a dissecting microscope. Subsequently, muscle strips were chemically permeabilized by overnight (O/N) incubation in relaxing solution with 1% Triton X-100 at 4 °C. The tissues were then extensively washed in fresh ice-cold relaxing solution, stored at 4 °C, and used within 24 h [95].

| | Stock solution or MW | pCa9 (mM) |
|---|---|---|
| KOH | 56.11 g/mol | 66.32 |
| EGTA | 380.35 g/mol | 10 |
| KProp | 1 M | 49.76 |
| $Na_2CrP$ | 255.1 g/mol | 10 |
| $MgCl_2$ | 1 M | 6.48 |
| ATP | 592.6 g/mol | 6.3 |
| BES | 213.3 g/mol | 100 |
| g or ml / 1L | pH 7.0 adjust with KOH | |

***Table 2:*** *Components and concentrations of the solution used to skin human muscle samples.*

## 6.3 Energetic and mechanical measurements

The skinned preparations were mounted horizontally between a force transducer (KG4, Scientific Instruments Heidelberg, Germany or modified silicon strain gauge AE-801, SenSonor, Horten, Norway) and a motor (Scientific Instruments Heidelberg, Germany) via aluminium T-clips (see figure 25).

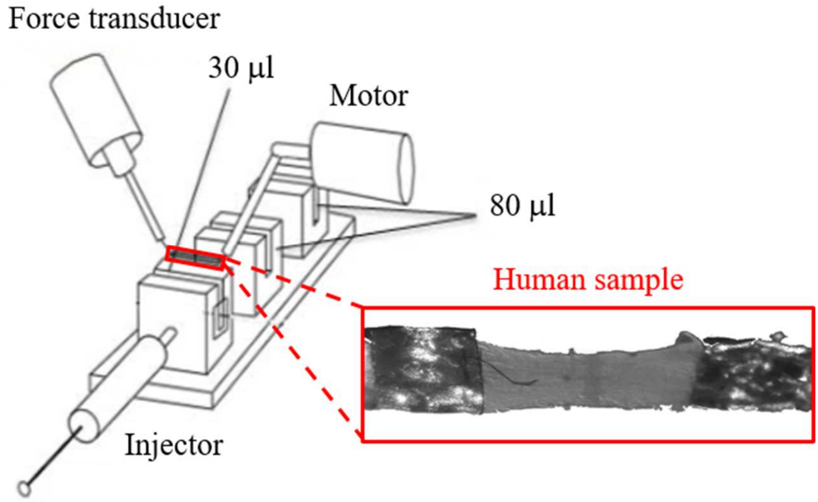

***Figure 25: Experimental set-up.*** *Representative scheme exhibiting the muscle fiber positioned between a force transducer and a motor. The muscle fiber is transferred from the baths which contain the relaxing and pre-activating solution (80 µl), to the ATPase assay chamber (30 µl) which contain activating solution. Modified from* [105]*. A magnification showing ventricular skinned strip mounted using two T-clips is displayed in the red square.*

The length of the preparations was adjusted based on the passive tension stretching them about 15% above the slack length, which correspond to a sarcomere length (SL) of about 2.1-2.2 µm [104]. Mean dimensions (± S.E.M.) of HCM and donor ventricular preparations amounted to 1.34 ± 0.06 and 1.53 ± 0.07 mm in length, 0.31 ± 0.01 and 0.27 ± 0.01 mm in width, and 0.28 ± 0.01 and 0.23 ± 0.01 mm in depth, respectively. Three types of solutions were employed: relaxing solution, pre-activating solution and maximal activating solution (see table 3).

| | Stock solution or MW | Activating pCa4.5 (mM) | Pre-activating pCa10 (mM) | Relaxing pCa10 (mM) |
|---|---|---|---|---|
| **$CaCl_2$** | 1 M | 10 | - | - |
| **ATP (93.1% pure)** | 551.14 g/mol | 6.2 | 6.2 | 6.2 |
| **EGTA (96.5% pure)** | 380.35 g/mol | 10 | 10 | 0.2 |
| **$MgCl_2$** | 1 M | 6.6 | 6.92 | 6.69 |
| **Kprop** | 1 M | 14.2 | 33.99 | 34.35 |
| **BES** | 213.3 g/mol | 100 | 100 | 100 |
| **DTT** | 500 mM | 1 | 1 | 1 |
| **HDTA** | 348.36 g/mol | - | - | 9.8 |
| **PEP** | 206.14 g/mol | 10 | 10 | 10 |
| **$NaN_3$** | 1 M | 5 | 5 | 5 |
| **g or ml / 100 ml** | **pH 7.0 adjust with KOH** | | **Ionic strength 200** | |

***Table 3:*** *Components and concentrations of the solution used to relaxing, pre-activating and activating phases.*

Solutions were applied in the sequence: relaxing, pre-activating, activating, relaxing. Isometric force and ATPase activity were simultaneously measured at 25 °C. During the measurement fibers were kept inside a small (30 µl) chamber with thin quartz windows containing activating solution. The force generated and ATP consumed were measured simultaneously during the contraction (see figure 26). Maximal force was determined at steady-state level and normalized to the cross-sectional area (CSA, $mm^2$) of the muscle strip to calculate tension (force/CSA, $mN/mm^2$). The CSA of the preparation was estimated based on an elliptical shape, i.e, $CSA = (width \times depth \times \pi)/4$. ATPase activity was measured using an enzyme coupled assay. In this assay the ATP regeneration from ADP and phosphoenol-pyruvate, catalysed by the enzyme pyruvate kinase, is coupled to the oxidation of NADH to $NAD^+$ and the reduction of pyruvate to lactate, catalysed by L-lactic dehydrogenase. NADH oxidation was measured photometrically from the absorbance at 340 nm of near-UV light. This absorbance signal was calibrated using multiple injections of 50 nl of 10 mM ADP in the measuring chamber. Using this calibration, ATPase activity ($pmol\mu l^{-1}s^{-1}$) in the preparation was derived from the slope of the absorbance signal. The TC (isometric ATPase per unit force, $pmol\mu l^{-1}s^{-1}/mN/mm^2$) was calculated as the ratio ATPase activity/tension.

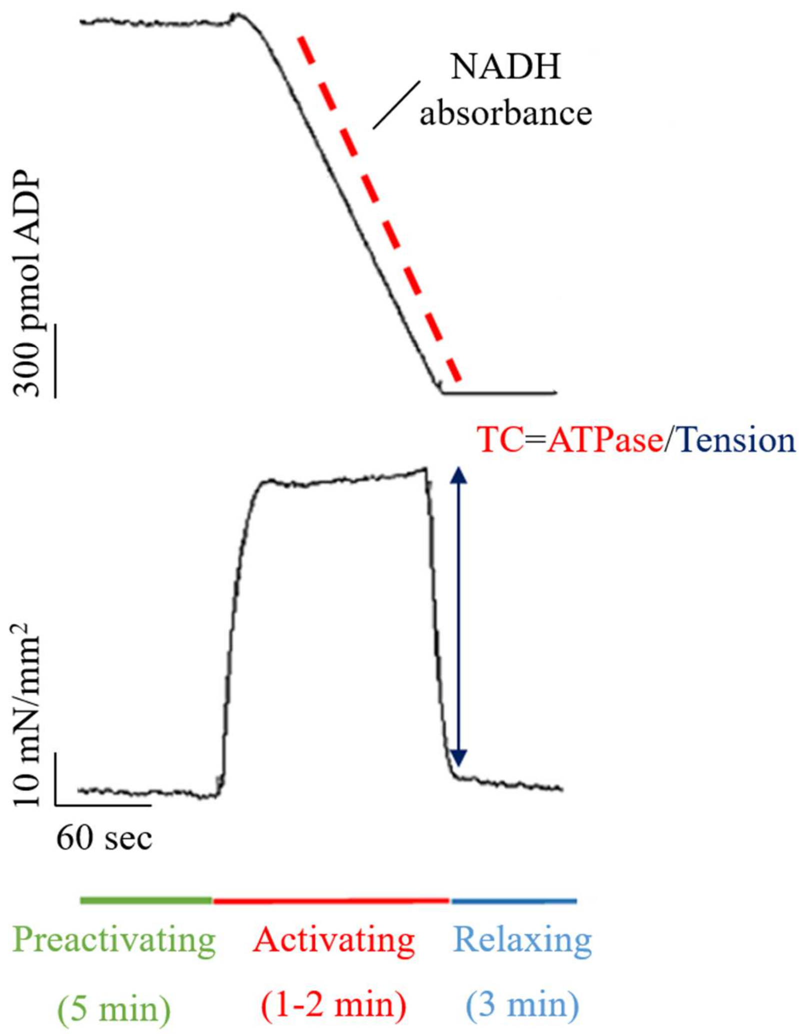

***Figure 26: Strip activation cycle.*** *NADH absorbance is measured and is directly proportional to ATP consumption (top). The difference between maximum and rest tension is measured (bottom). Tension cost (TC) is the difference between maximal and resting ATPase activity / maximal force ratio.*

## 6.4 Fibers preparation: fixation, staining and clearing

To perform structural analysis, strips were fixed O/N in 5 ml of paraformaldehyde (PFA) 4% in 0.01 M phosphate-buffered saline (PBS, pH 7.6) at 4°C. During fixation samples were kept stretched to maintain the same structural organization of the tissue and avoid swelling. Samples were then rinsed three times (15 minutes each) in 5 ml of 0.01M PBS at 4°C. Each strip was stained first with an anti-α-actinin antibody (A7811, Sigma-Aldrich, US, dilution 1:200) for 1 day at 4°C, then, after one day of washing with $PBST_1$ (PBS and 1% Triton X-100, pH 7.6) at room temperature (RT), a secondary antibody conjugated with an Alexa Fluor 594 (ab150108, Abcam, UK, dilution 1:100) was applied for 3 days at RT. Then, after one day of washing with $PBST_1$ at RT, samples were fixed in 1 ml of PFA 4% at RT for 5 minutes to prevent antibody detachment. To remove exciding PFA residue, samples were rinsed three times (5 minutes each) in 1 ml of 0.01M PBS at RT. Finally, samples were optically cleared with serial incubations in 2 ml of 20%, 47% and 68% (vol/vol) TDE (166782-500G, Sigma-Aldrich, US) in 0.01 M PBS (TDE/PBS) each for 1 hour at RT while gently shaking [1].

## 6.5 Two-photon fluorescence microscope

A custom-made TPFM was used to image the strips (see figure 27). A mode locked Ti:Sapphire laser (Chameleon, 120 fs pulse width, 80 MHz repetition rate, Coherent, CA) operating at 780 nm was coupled into a custom-made scanning system based on a pair of galvanometric mirrors

(LSKGG4/M, Thorlabs, USA). The laser was focused onto the specimen by a refractive index tunable 25× objective lens (LD LCI Plan-Apochromat 25×/0.8 Imm Corr DIC M27, Zeiss, Germany). The system was equipped with a closed-loop XY stage (U-780 PILine® XY Stage System, Physik Instrumente, Germany) for radial displacement of the sample and with a closed-loop piezoelectric stage (ND72Z2LAQ PIFOC objective scanning system, 2 mm travel range, Physik Instrumente, Germany) for the displacement of the objective along the z axis. The fluorescence signal was collected by an independent GaAsP photomultiplier module (H7422, Hamamatsu Photonics, NJ). Emission filter of 618 ± 25 nm was used for Alexa Fluor 594 detection.

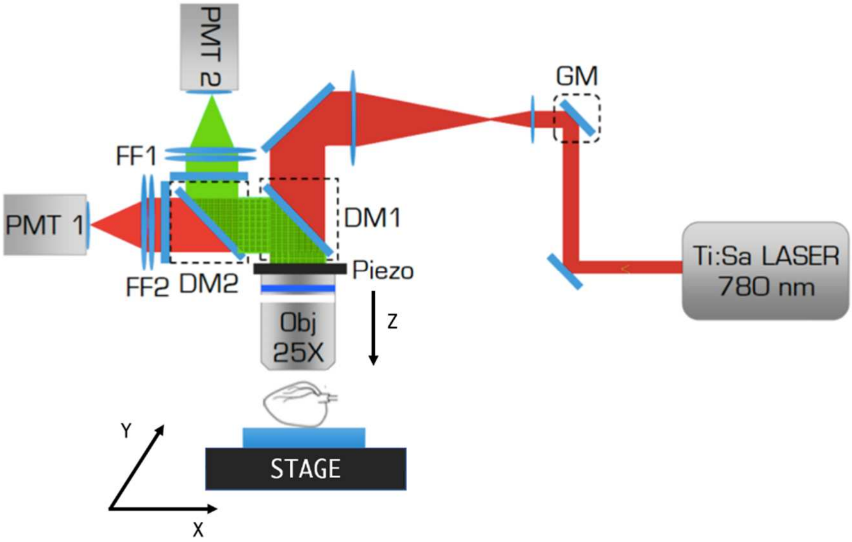

***Figure 27: A custom-made two-photon fluorescence microscope (TPFM).*** *Simplified scheme shows TPFM apparatus. Obj: objective; GM: galvanometric mirrors; DM: dichroic mirror; FF: fluorescence filter; PMT: photomultiplier tube; Piezo: closed-loop piezoelectric stage; Stage: closed-loop XY stage.*

## 6.6 Imaging and image pre-processing

The whole volume was acquired performing z-stack imaging of adjacent regions. Each stack had the depth equal to the thickness of the analyzed strip (in a range of 250-350 µm) with a z step of 2 µm between images. Each frame had a field of view of (450 × 450) µm and a pixel size of (0.44 × 0.44) µm. Adjacent stacks had an overlap of 40 µm. The stacks were fused together in order to reconstruct the whole sample. ZetaStitcher (G. Mazzamuto, "ZetaStitcher: a software tool for high-resolution volumetric stitching", https://github.com/lens-biophotonics/ZetaStitcher) was used for volumetric stitching, a Python package developed internally for this purpose. This software exploits the overlap between neighboring stacks to correct the micron-scale mechanical error of the imaging platform (see figure 28).

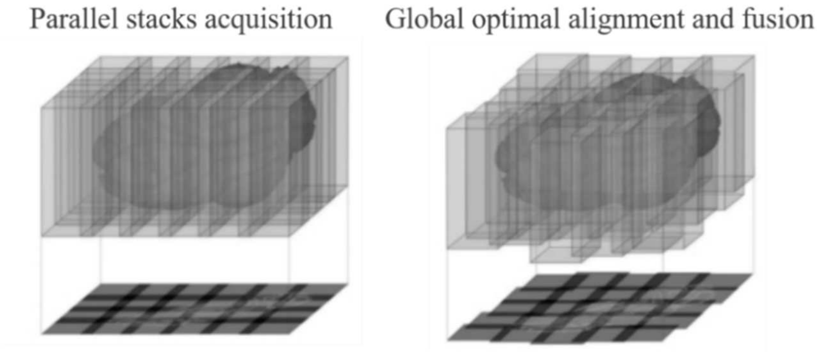

***Figure 28: Volumetric stitching.*** *Scheme of parallel stacks acquisition, alignment and fusion made with the global optimization algorithm ZetaStitcher. Modified from* [106].

It is based on two steps: an alignment process followed by image fusion. As a first step, a 2D cross-correlation map is evaluated at several depths for every pair of adjacent 3D stacks, moving each stack relative to its neighbor. The final position of all stacks is determined by applying a global optimization algorithm to the displacements of the individual pairs. Finally, the stacks are fused into a 3D reconstruction of the whole sample stored in single TIFF file.

## 6.7 3D segmentation and reconstruction

In order to reconstruct 3D muscle fibers architecture of the whole muscle strip with sub-cellular resolution, an image analysis pipeline based on sarcomeric z-lines periodicity was developed. This required well resolved and high contrast 3D images. To this end, the signal-to-noise ratio of the images was improved by applying a deconvolution process, performed using the Huygens Software (Scientific Volume Imaging), based on the actual Point Spread Function (PSF) of TPFM used for imaging. Then, a Contrast Limited Adaptive Histogram Equalization (CLAHE algorithm; clip = 0.08, K = 128 pixels) was applied to each frame. This image post-processing guarantees the necessary contrast and resolution to discriminate sarcomeric z-lines across the whole sample. Subsequently, to perform a 3D segmentation of the muscle tissue, a 2D analysis was applied at each optical section where a K-Means algorithm was used to quantize the pixel intensities in four levels. These four clusters were dynamically classified as background or tissue and morphological operators were applied to the binary segmentation in order to delete artifacts and to smooth the result. In particular, the closing operator was applied to remove salt and pepper noise artifacts; then, little black holes were filled and little white objects were removed to include intracellular space and to remove extracellular elements. Finally, an opening operator and a dilatation operator were applied to smooth the border of the cell areas. The 3D mask was then obtained by stacking 2D segmented sections along the Z axis and applied the TPFM stitched image.

## 6.8 Fibers architecture analysis and quantification

To analyze the fiber architecture of the sample at cellular level the volume has been virtually decomposed into portions of (16 × 16 × 16) µm that correspond to macro-voxels of (36 × 36 × 8) pixels. Macro-voxels were analyzed only if they contain at least 80% of cell tissue. To estimate cell orientation the perpendicularity between the sarcomere z-lines and the cardiomyocyte axis was exploited with a frequency analysis approach. A 3D Fast Fourier Transform (FFT) was applied to each macro-voxel to extract the related spectrum $S$ and shifted in a symmetric configuration (see figure 29). Due to the anisotropic voxel size, the z-axis was oversampled in the frequency space: the z component of the spectrum was extended and filled with zero intensity pixels to reach an isotropic dimension of (36 × 36 × 36) pixels. Then, a band-pass filter was applied to $S$ selecting the frequencies of sarcomeric structures. Considering that in the frequency space the voxel size is (0.0631 × 0.0631 × 0.0625) $\mu m^{-1}$, a 3D spherical filter was created with a cutoff frequency of 0.556 $\mu m^{-1}$ (1 / 1.8 µm) = 9 pixels in radius and a bandwidth between 0.5 $\mu m^{-1}$ (1 / 2.0 µm) = 8 pixels and 0.625 $\mu m^{-1}$ (1 / 1.6 µm) = 10 pixels in radius. The Power Spectrum Density (defined as $|S|^2$) was calculated for the filtered (PSD) and unfiltered ($PSD_f$) spectrum. A Gaussian with $\sigma = 0.8$ (kernel of 3 × 3 × 3 pixels) was convolved with both $PSD$ and $PSD_f$, in order to smooth the contribution of the border of the macro-voxel. Then, the ratio between $PSD_f$ and $PSD$ ($PSD_{ratio}$) was calculated and, if it was greater than 50%, the frequency content was considered reliable. In this case, the coordinates of the voxel with maximum intensity were extracted from the $PSD_f$ to localize the principal frequency component. A centroid of a $(4 \times 4 \times 4)$ pixel region around the peak was evaluated in order to improve the spatial resolution. Finally, the components of the 3D orientation vector were defined as the distance between the centroid and the center of the spectrum. Every vector was stored in a virtual volume indexed by the position of the analyzed macro-voxel to reconstruct the fibers architecture of the whole sample.

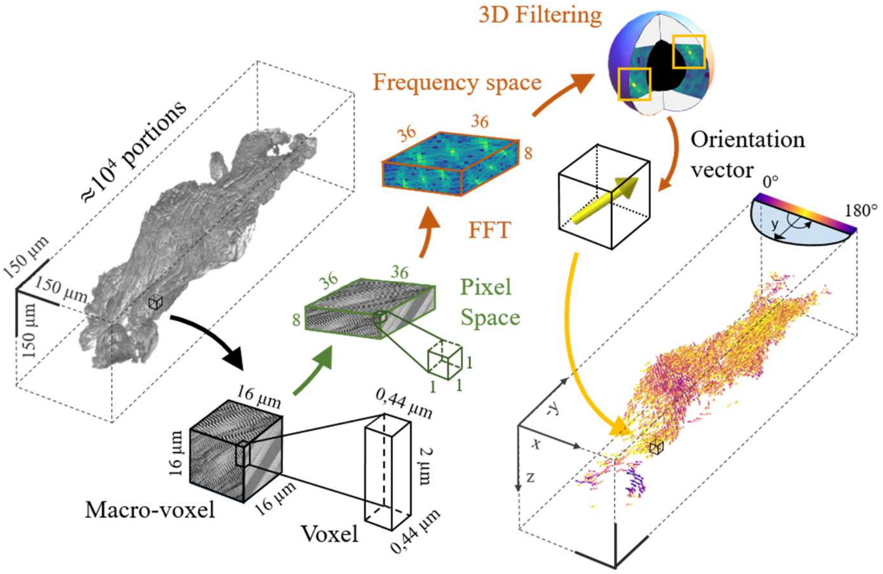

***Figure 29: Fibers orientation analysis.*** *A pipeline explaining the different steps used to obtain an orientation map with sub-cellular resolution of strip fibers is shown. The 3D volume is virtually divided in macro-voxel of (16 × 16 × 16) µm. A 3D FFT is applied to each macro-voxel obtaining a PSD (Frequency Space). A band-pass filtering is applied to select the periodicity of the sarcomere z-lines and the bigger frequency component (the yellow highlighted peaks) is localized. The orientation of the fibers is extracted by the peaks position in the 3D space and stored as a vector (Orientation vector). Finally, the fibers architecture of the sample is reconstructed by the ensemble of the total orientation vectors.*

Two geometrical parameters were defined to quantify the global fiber spatial organization: Alignment (A in equation 4) and Disarray (D in equation 5).

$$A = \frac{\sum_i \frac{d_y^i}{\sqrt{d_x^i + d_y^i + d_z^i}}}{N} \in [0,1] \qquad \forall i \in [0,\ldots,N] \qquad [4]$$

Where *N* is the number of vectors and *d* is the vector component. This parameter was calculated with respect to the Y axis: strip major axis that also define the direction of the force measurement.

$$D = \frac{\sum_j \left(1 - \left|\frac{\sum_i \hat{u}_{ij}}{n_j}\right|\right)}{m} \in [0,1] \quad \forall i \in [0,\ldots,n]\,;\ \forall j \in [0,\ldots,m] \quad [5]$$

Where *m* is the number of macro-voxel (of a dimension 64×64×64 $\mu m^3$) where a local disarray is quantified. We define local disarray the module of the average vector of the *n* orientation vectors $\hat{u}$ within the $j^{th}$ macro-voxel.

## 6.9 Statistical analysis

Graphs were done with OriginPro 2018 (OriginLab Corporation). The statistical test used to calculate P values and to compare normally-distributed data was Unpaired t test. The P values are indicated in the figures and considered significant when < 0.05.

# Chapter VII

# Results

This chapter presents the results obtained by combining functional measurements (maximal force and TC) with structural features achieved using TDE clearing and TPFM.

## 7.1 Functional investigation

To investigate the impact of the cMyBP-C E258K mutation on the sarcomere energetics, Triton-permeabilized ventricular strips from myectomy samples from three E258K HCM patients and two donors, were used to simultaneously measure maximal force as well maximal steady-state ATPase activity at 25°C. Representative functional recording of both force development and ATPase activity of a muscle strip are shown in figure 30a. Maximal tension (maximal force normalized by CSA) was significantly lower (31.08 ± 1.49 $mN/mm^2$) in HCM preparations compared to donors (40.1 ± 0.97 $mN/mm^2$) ($p<0.05$), as shown in figure 30b. The amount of ATP consumption in relation to isometric force development or TC, was calculated, for each preparation, as the ratio between ATPase activity and active tension. As shown in figure 30c, TC was significantly higher in HCM than in donor samples. TC (in $pmol\mu l^{-1}s^{-1}/mN/mm^2$) amounted to 2.26 ± 0.06 in donor tissue and to 3.08 ± 0.12 in HCM tissue ($p<0.05$).

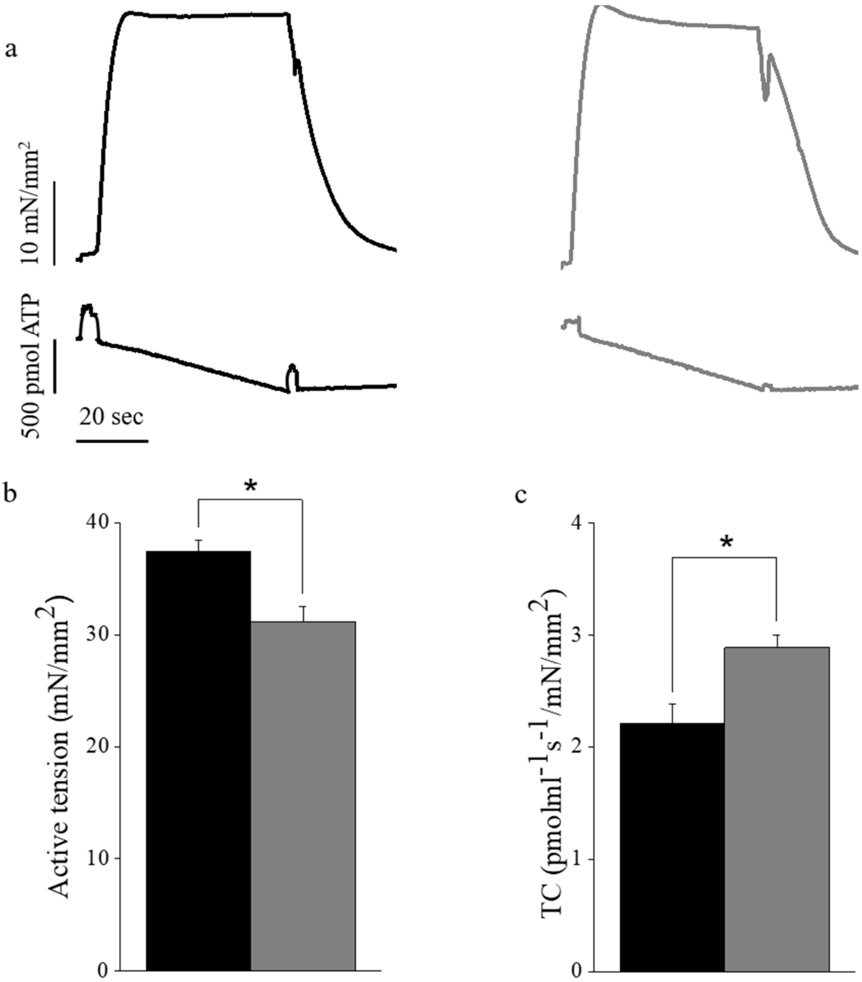

***Figure 30: Impact of the E258K mutation on sarcomere energetics. (a)*** *Representative isometric tension (top) and ATPase activity recordings in skinned ventricular strips from donors (black) N=2, n=25 and E258K (gray) N=3, n=21 at 25°C.* ***(b)*** *Mean ± SEM of maximal active tension. Tension of E258K strips was significantly reduced compared to donors (*$p<0.05$).* ***(c)*** *TC determined as the ratio between ATPase activity and maximal active tension. TC of E258K muscle strips was significantly higher compared to donors (*$p<0.05$). N=number of patients, n=number of muscle strips. Statistical tests: Unpaired Student t tests * = $P<0.05$.*

Steady-state tension was corrected in each individual strip for its mild deterioration, force rundown, during each activation assuming that a similar amount of deterioration occurred with each contraction [107]. Time-dependent force rundown was, on average, 6.1 ± 1.6 % and 9.18 ± 1.7 % in HCM and donor strips, respectively. Any strip exhibiting greater than 20% force deterioration was discarded.

## 7.2 Structural investigation

Mechanical dysfunction observed in the HCM patients can be also related to macroscopical disorganization of myocardial fibers. To exclude this hypothesis, a 3D architecture analysis of the samples was performed. To this aim, a protocol able to reconstruct the whole intact strip using a combination of advanced labeling, clearing and imaging techniques was developed.

### 7.2.1 Staining, clearing and imaging optimization

A subset of samples that previously underwent functional measurement were structurally evaluated in a direct correlative manner. The fiber reconstruction (performed maintaining the same traction used for functional investigation) was based on sarcomeric labeling using an anti-α-actinin antibody. This immuno-staining protocol has been optimized on three months old C57Bl/6 wild-type (WT) mouse heart. The heart was excised, and the proximal aorta was perfused retrogradely first with 0.01 M PBS, then with PFA 4%. After that, the heart was fixed as previously described in methods for the strips. Later, trials with primary ($Ig_1$) and secondary ($Ig_2$) antibodies at different incubation times were performed (see figure 31). The immune-staining protocol with the highest signal amplification corresponds to incubation time of 24 and 72 hours for $Ig_1$ and $Ig_2$ respectively. This immune-staining protocol was able to stain the strips thought their whole thickness, of about 300 μm (see figure 32). A TDE based clearing method [1] was used to homogenize the refractive index of the tissue and reduce light scattering. The entire sample was acquired using a custom-made two-photon fluorescence microscope equipped with a motorized closed-loop XY stage that produce a tiled scan allowing mesoscopic reconstruction at micro-scale resolution (see figure 33). A volumetric stitching based on a global optimization algorithm was performed on the entire sample using a custom-made Python software: ZetaStitcher.

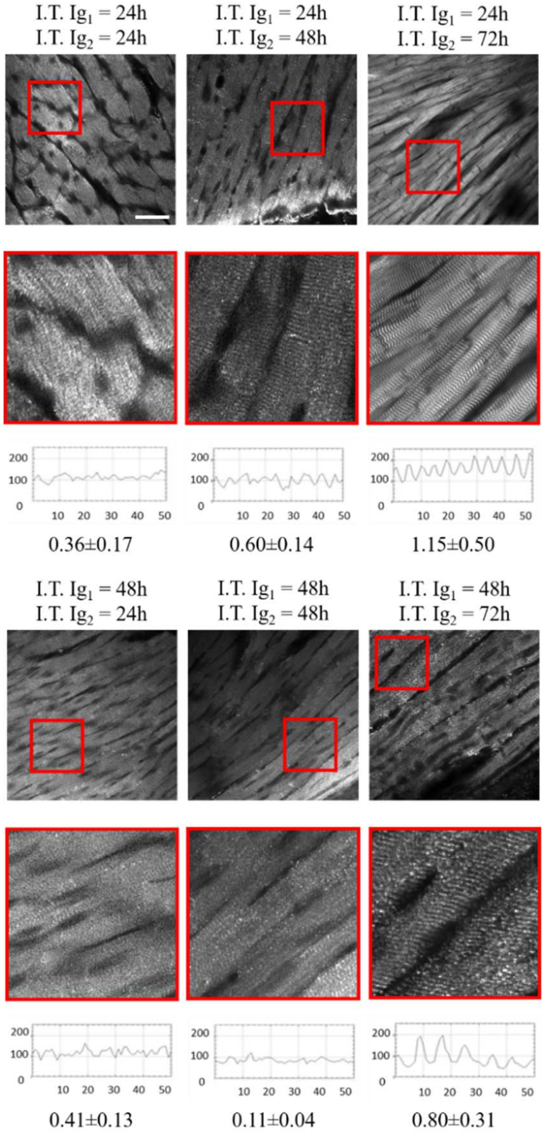

***Figure 31: Representative two-photon images of mouse heart stained with Ig1 and Ig2 antibodies at different I.T..*** *Red squares are magnifications to appreciate sub-cellular resolution. Plot profile analysis perform with Fiji (http://fiji.sc/Fiji) to assess the best contrast in sarcomeric staining. Scale bar 50 µm.*

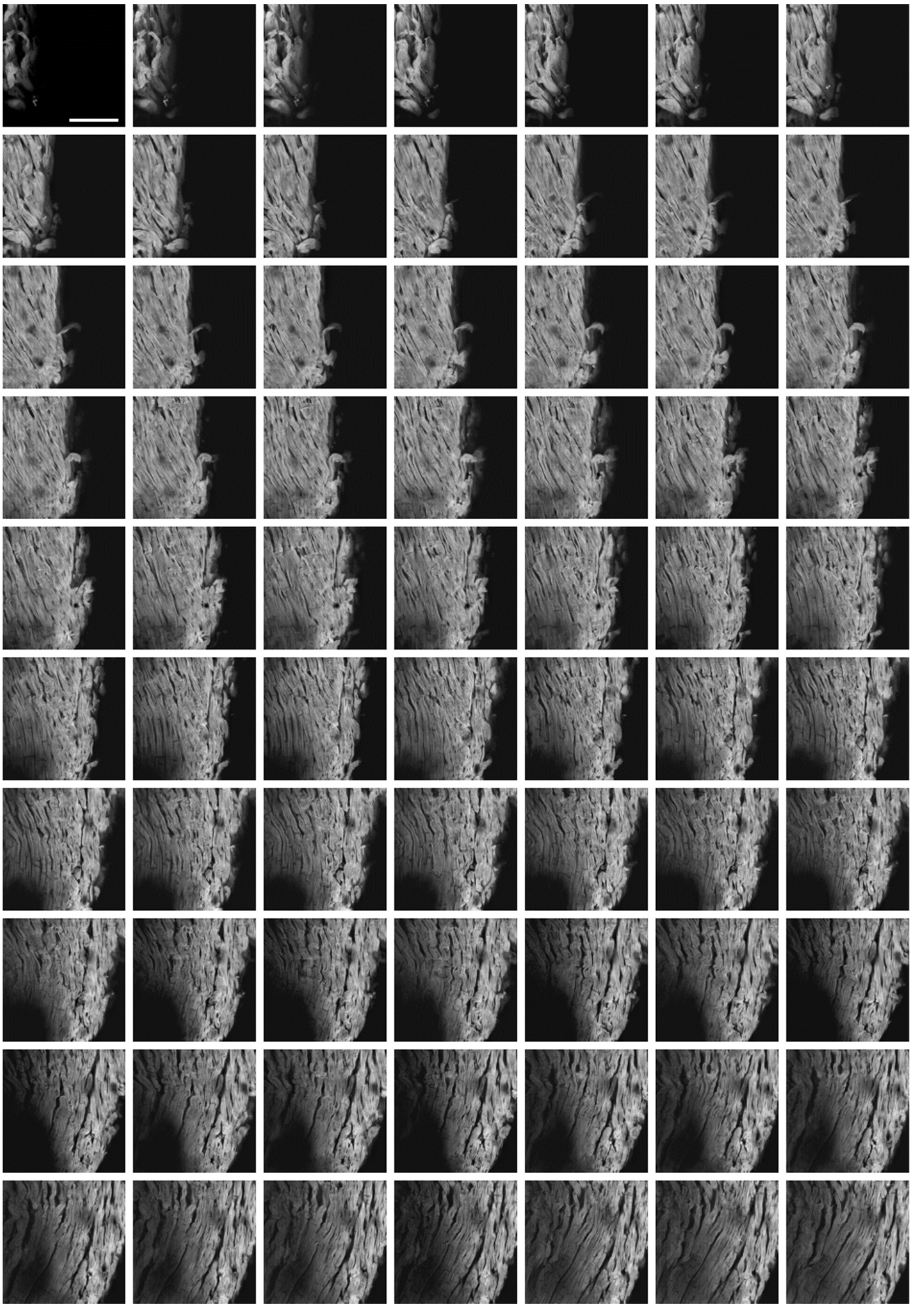

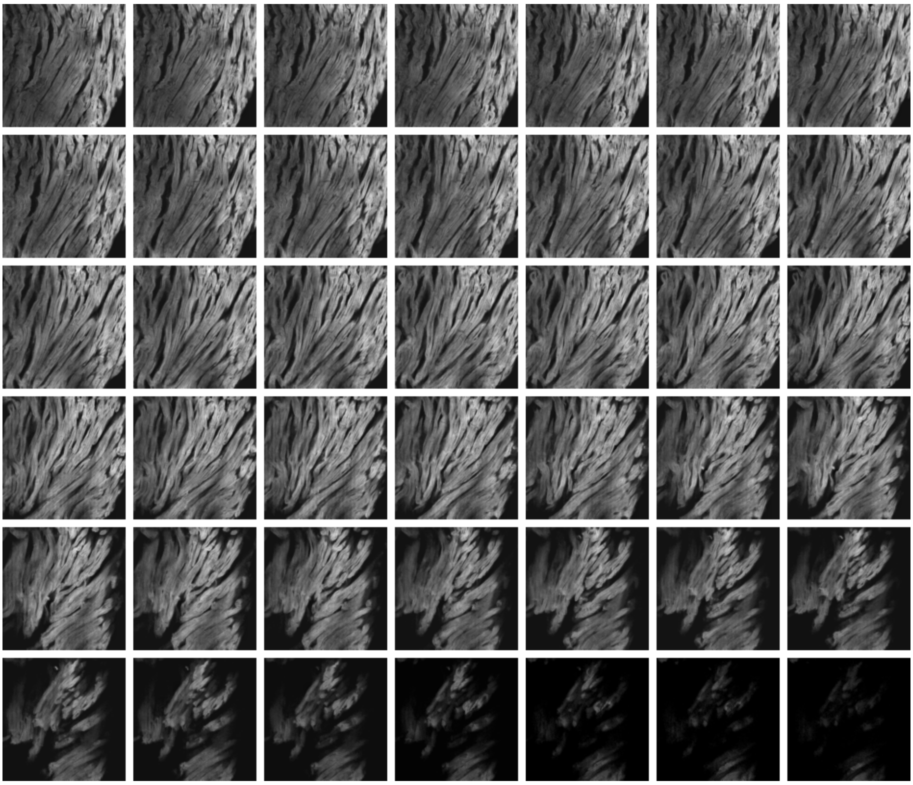

***Figure 32: Representative stack of human muscle strip.*** *Frames in series of a stack with a depth of 224 μm. There are 2 μm between one frame and the next. Sample is immune-stained with anti-α-actinin antibody, cleared with 68% TDE/PBS and imaged with TPFM (Zeiss, 25X objective). Scale bar 100 μm.*

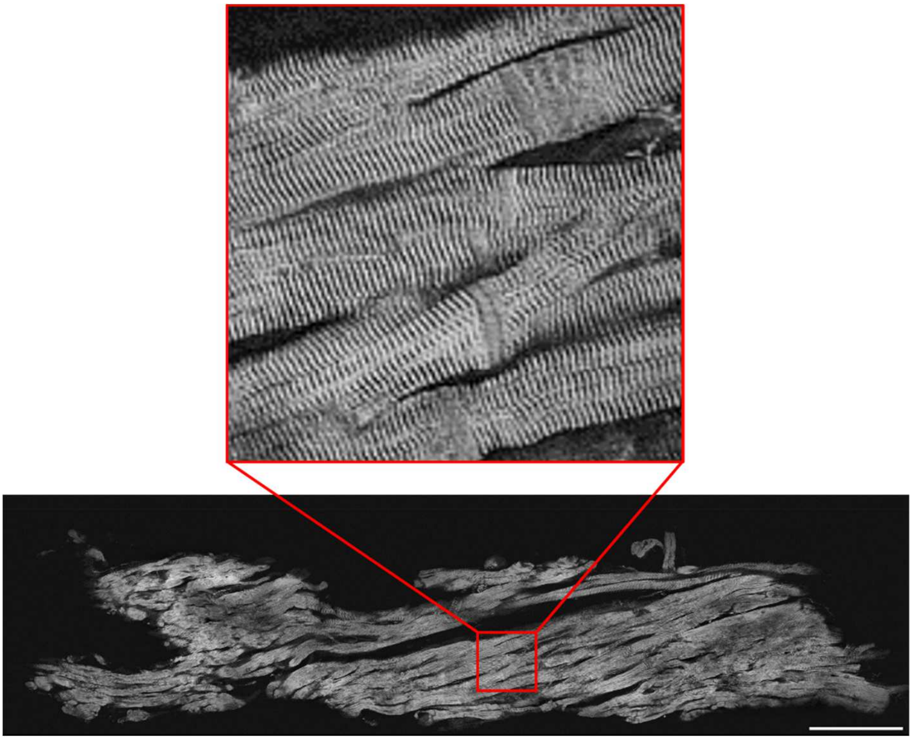

***Figure 33: Tissue labeling, imaging, and preprocessing.*** *A reconstruction of a representative human muscle strip labeled with anti-α-actinin antibody, cleared with 2,2'-thiodiethanol 68% and imaged with two-photon fluorescence microscope is represented. The frame shows the stitched area after the deconvolution and the contrast equalization. A magnification showing the sarcomere z-lines at sub-cellular resolution is displayed in the red square. Scale bar 200 µm.*

### 7.2.2 Correlation

The advanced structural investigation was performed in seven strips from one donor and seven strips from two E258K HCM patients, previously used for functional investigation. In particular, a global quantification of 3D cellular organization was performed defining two geometrical parameters: alignment and disarray. The alignment represents the average direction of the fibers with respect to the strip major axis (the direction of the force measurement) and it represents the real contribution of the cells to the force production. The disarray characterizes the degree of order of fibers inside the strip and it was quantified by simply averaging local disarrays. Based on these two parameters, no qualitative macroscopic difference in the tissue organization was observed between E258K patients and donor (see figure 34).

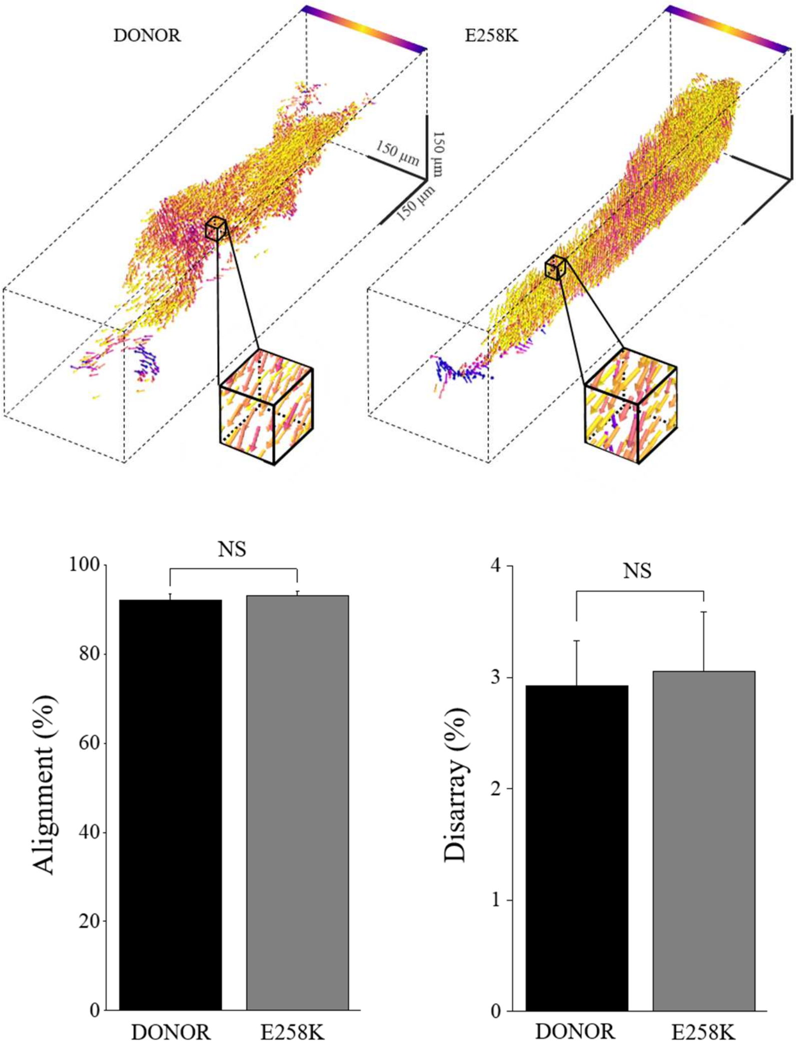

***Figure 34: Structural analysis***. *Representative 3D reconstructions of strips from donor (left) and E258K patient (right) show vectors distribution based on fibers orientation. Different colors render the angle of the vector on the XY plane. Quantitative comparisons of cellular alignment (respect to the traction axis) and local disarray of skinned ventricular strips from E258K N=2, n=7 and donor N=1, n=7 are reported in column bar. N=number of patients, n=number of muscle strips. Statistical tests: Unpaired Student t tests. NS = no significant.*

Structural differences were not detected between the two experimental classes, however functional defects were confirmed in the subgroup of samples randomly chosen. In detail, in figure 35 structural and functional features were correlated at a sample-by-sample level. The results show a significant reduction of the maximum force, without a statistical difference in fibers alignment and a significant increase of TC with not variation in fibers disarray.

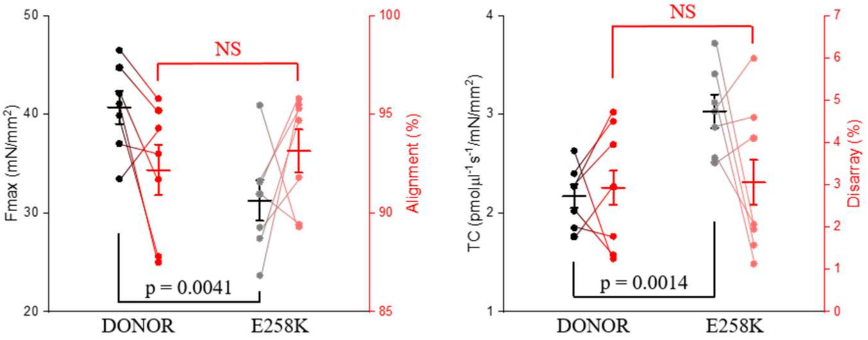

***Figure 35: Correlative analysis.*** *Structural (in red) and functional (in black) results of 14 stripes (seven from one donor and seven from two E258K patients) are analyzed. On the left Maximal Force (Fmax) and Alignment (A) are correlated while on the right TC and Disarray (D) are compared.*

# Chapter VIII

# Discussion

Mutations in cMyBP-C are prevalent causes of HCM. Although HCM-causing truncated mutations in cMyBP-C are well studied, the growing number of disease-related cMyBP-C missense mutations remain poorly understood.

This study investigated if E258K mutation in gene encoding MYBPC3 underlie changes in the force production and energetic cost of contraction in human samples. Energy cost of contraction was studied in vitro measurements of force generation and ATPase activity in cardiac muscle strips from three HCM patients and the results were compared with cardiac muscle strips from two donors. Permeabilized cardiac multicellular preparations from manifest HCM patients with E258K mutation on cMyBP-C showed significantly lower maximal tension development compared with multicellular preparations from donors. This is in line with the previously found decrease in maximal tension in single human cardiac cells harbouring MYBPC3 mutation and in human cardiac muscle strips with truncated mutation in c-MyBPC compared with donor cardiomyocytes and multicellular preparations respectively [95, 108 - 112]. Moreover, the results showed TC significantly increased in E258K patients compared to donors. This increase of TC is explained primarily by a reduction of maximal force. This finding is in line with previous results in muscle strips from transgenic mouse model and human sample harbouring mutations in TNNT2 [86, 93, 113], but also in human muscle strips with mutations on genes encoding for MYH7 and MYBP3 [84, 95].

Myocardial remodeling such as disarray and misalignment may contribute to lower maximal force and to increase TC in cardiac muscle strips. Indeed, the synchronized contraction of cardiomyocytes in parallel alignment should allow for maximal force development, while cardiomyocytes orientated at different angles (local disarray) would lead to reduced maximal force development. To exclude this hypothesis, a novel approach was developed to directly correlate the influence of structural features with force development and TC generation in skinned muscle strips from E258K patients and donors.

To this aim, using a combination of advanced immune-staining and tissue clearing, an imaging protocol able to reconstruct the whole intact strip with sub-cellular resolution was developed. To quantify structural features FFT analysis was applied in seven strips from one donor and seven strips from two E258K patients previously used for functional investigation. Cellular alignment (with respect to the traction axis) and local disarray were analyzed and no significant differences were found between E258K patients and donor. Finally, maximal force and cellular alignment were correlated, while TC was correlated with local disarray. These results suggest that structural alterations do not influence sarcomere energetics, because there was no correlation between functional and structural features. Consequently, the hypothesis according to which the presence of sarcomeric gene mutation induce energy depletion is confirmed.

In conclusion, using this novel approach, functional and structural measurements were directly correlated sample by sample.

# Part III

## Structural mapping of action potential propagation pathways through healthy and diseased hearts

# Summary

In this project, a transgenic mouse model of HCM carrying a missense mutation R92Q in the gene coding for cTnT was examined. The mutation R92Q is characterized by a severe degree of left ventricle hypertrophy. First, using a recently-developed ultra-fast optical system [2] the propagation of electrical activity was mapped in whole diseased and control hearts. Then, advances in tissue clearing, staining and high-resolution optical microscopy were combined to reconstruct the 3D organization of cardiac conduction in the whole mouse heart. A PASSIVE CLARITY protocol [3] was developed for clearing the heart and for achieving fluorescent probe penetration into the whole tissue. A fluorescent staining protocol was optimized to visualize the whole heart cytoarchitecture at sub-cellular level. The high contrast and resolution of LSM was exploited to image cellular organization by staining in the cardiac tissue. A cytoarchitectonic analysis was applied to identify cells and to map myofilaments alignment in three dimensions, defining the conduction pathway of action potential propagation at intercellular level. Finally, the propagation maps were correlated with the pathological disorganization of myofilaments using the 3D high-resolution optical reconstruction.

# Chapter IX

# Biological rationale

Thin filament mutations occur in only 6-8% of patients with HCM, making it a rare condition. However, several clinical and preclinical studies pointed out that HCM associated with thin filament mutations is in many ways a disease on its own, since both the clinical course and the molecular pathophysiology are different from much more common thick filament HCM [114]. To date, a wide array of nearly 100 independent mutations in all components of the cardiac thin filament have been identified [115]. Despite the clinical heterogeneity observed in this group of patients, compared with patients carrying thick filament mutations, thin-filament patients appear to suffer from a higher risk of sudden cardiac death, even in the absence of the “classical” risk factors such as the presence of strong hypertrophy. Moreover, these patients are more likely to develop severe diastolic dysfunction, systolic abnormalities and refractory heart failure. In a considerable subgroup of patients, HCM is determined by mutations of the sarcomere thin filament regulatory protein genes, including cTnT, cTnI and Tropomyosin (Tm). Albeit mutations in cTnT are the most common thin filament mutations, they account for only 3-5% of all cases of HCM. Nonetheless, HCM patients with cTnT mutations have an increased likelihood of suffering a sudden cardiac death [39]. At least 26 known mutations have been found in the human cardiac TnT gene that are linked to HCM, including 23 missense mutations, one deletion mutation, and one splicing donor site mutation [116]. Patients who present TnT mutations often show no or mild hypertrophy, myocardial disarray, and have a malignant phenotype associated with a high incidence of sudden death. Thin filament HCM has been much less studied due to its rarity and no specific preventive therapeutic option exists to address the increased risk of arrhythmias and clinical progression. From this stems the need of detailed studies on the electrical activity and structural alterations in the presence of thin filament mutations, because electro-mechanical dysfunction is closely correlated with myofilaments disorganization. Indeed, electro-mechanical dysfunction in HCM hearts may lead to ventricular tachyarrhythmia emanating from a structurally abnormal myocardium [117 - 122]. Therefore, it is of great relevance to correlate action potential propagation at the whole heart level with 3D reconstructions at cellular resolution.

# Chapter X

# Methods

This chapter explains the innovative techniques used to perform functional measurements and high-resolution 3D reconstructions.

## 10.1 Animal model

A transgenic mouse-model of HCM carrying the heterozygous missense mutation Arg92Gln (R92Q) in TNNT2 gene with C57BL/6 genetic background was generated in Dr. Tardiff's Lab [123, 124] and employed for this study. Heterozygous progenitors were bred with C57BL/6 females and the genotypes of the offspring determined by PCR on DNA from tail biopsy specimens. Animals used for experiments were 6 months old males and females control (CTRL) and heterozygous R92Q. Animals were maintained and bred at the animal facility of the University of Florence, Italy, according with the local ethical committee rules. All experimental protocols were performed in agreement with current Italian and European regulations and were approved by the local institutional review board and the animal-welfare committee of the Italian Ministry of Health.

# 10.2 Isolated and perfused mouse heart

Transgenic positive and negative mice (6 months old) were heparinized (0.1 mL at 5,000 units/mL) and anesthetized by inhaled isoflurane (5%). The excised heart was immediately bathed in Krebs-Henseleit (KH) solution and cannulated through the aorta. The KH buffer contained (in mM): 120 NaCl, 5 KCI, 2 $Mg_2SO_4$-$7H_2O$, 20 $NaHCO_3$, 1.2 $NaH_2PO_4$-$H_2O$, and 10 glucose pH 7.4 when equilibrated with carbogen (95% $O_2$–5% $CO_2$). The contraction was inhibited for the entire experiment with blebbistatin (5 µM) in the solution. The cannulated heart was retrogradely perfused (Langendorff's perfusion) with the KH solution and then transferred to a custom-built optical mapping chamber at a constant flow of 2.5 mL/min at 37°C. Two platinum electrodes were placed below the heart for monitoring cardiac electrical activity via electrocardiogram (ECG). After stabilization of the ECG, typically within a few seconds, 1 mL of perfusion solution containing the voltage sensitive dye (di-4-ANBDQPQ; 5 µg/mL, University of Connecticut Health Center, Farmington, CT, USA) [125] was bolus injected into the aorta.

# 10.3 Optical mapping

Action potential propagation was investigated using a custom-made mesoscope (see figure 36). The whole mouse heart was illuminated in wide field configuration using a 2× objective (TL2x-SAP, Thorlabs, Newton, NJ, USA) and a light emitting diode (LED) operating at a wavelength centred at 625 nm (M625L3, Thorlabs) followed by a band-pass filter at 640/40 nm (FF01-640/40-25, Semrock, Rochester, NY, USA). The heart was illuminated with a maximum intensity of 1 $mW/mm^2$. A dichroic beam splitter (FF685-Di02-25×36, Semrock) followed by a band-pass filter at 775/140 nm (FF01-775/140-25, Semrock) was used for collecting the VSD-emitted fluorescence. A 20× objective (LD Plan-Neofluar 20×/0.4 M27, Carl Zeiss Microscopy, Oberkochen, Germany) was used to focus the fluorescence in a central portion (128×128 pixels) of the sensor of a sCMOS camera (OrcaFLASH 4.0, Hamamatsu Photonics, Shizuoka, Japan) operating at a frame rate of 1.6 kHz (630 µs actual exposure time). All microscope components were fixed onto a custom vertical honeycomb steel breadboard.

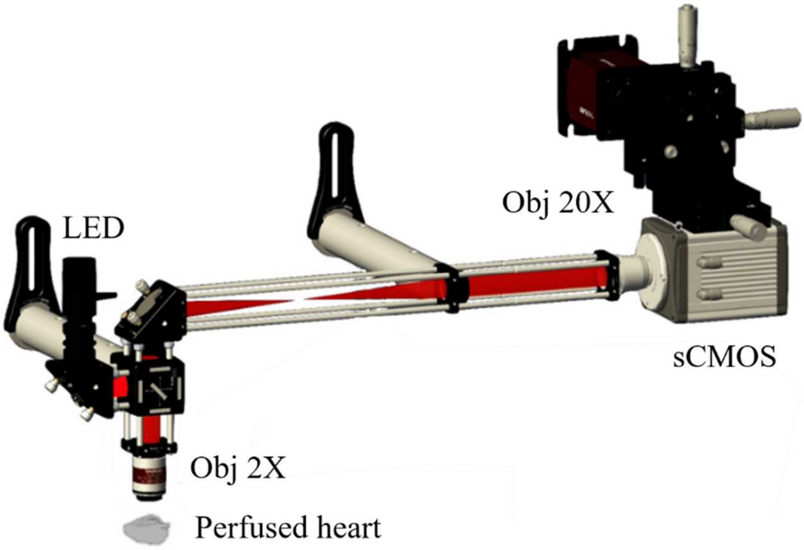

***Figure 36: Scheme of the wide field fluorescence mesoscope.*** *A red LED followed by a band-pass filter (640/40 nm) excites through a 2× objective the whole mouse heart, stained with a red-shifted electro-chromic voltage-sensitive dye (Di-4-ANBDQPQ). A dichroic beam splitter followed by a band-pass filter (775/140 nm) is used for collecting the emitted fluorescence signal. A 4f system is adopted to collimate the beam onto a 20× objective. The signal is then focused into a central portion (128×128 pixels) of a sCMOS sensor operating at a framerate of 1.6 kHz (630 µs actual exposure time). Modified from* [126].

## 10.4 Data analysis

$\Delta F/F_0$ imaging of electrical activity in the heart was performed processing the raw datum with ImageJ: for each frame, the mean baseline was first subtracted and then the frame was normalized to the mean baseline yielding a percentage change in fluorescence over time. Isochronal maps were performed using a custom-made software written in LabVIEW (LabVIEW 2015, Version 15.0 64-bit, National Instruments, Austin, TX, USA).

## 10.5 Statistical analysis

Graphs were done with OriginPro 2018 (OriginLab Corporation). The statistical test used to calculate P values for each data set was Paired t test. The P values are indicated in the figures. Each symbol corresponds to a pair of animals: black symbols refer to CTRL animals, while red symbols to R92Q animals.

## 10.6 PASSIVE CLARITY protocol, staining and clearing

After functional investigations, PASSIVE CLARITY protocol [3] (see figure 37) was performed. The hearts were perfused with 10 mL of ice-cold PFA 4% in 0.01 M PBS (pH 7.6). The hearts were fixed O/N in 20 mL of PFA 4% at 4°C. Samples were then rinsed three times (15 minutes each) in 20 mL of 0.01M PBS at 4°C. Subsequently, the hearts were embedded in 40 mL of Hydrogel at 4°C for 3 days with gentle shaking. Hydrogel solution is a mixture of 4% (wt/vol) acrylamide, 0.05% (wt/vol) bisacrylamide and 0.25% (wt/vol) VA044 in PBS. The samples were then degassed, and the temperature was increased to 37°C for 3 hours to initiate hydrogel polymerization. The embedded samples were extracted from the hydrogel and incubated in clearing solution (sodium borate buffer 200 mM, pH 8.5) containing 4% (wt/vol) sodium dodecyl sulphate (SDS) at 37°C for three months while gently shaking. After lipids removal, samples were washed in PBS at RT for 1 day and then in $PBST_{0.1}$ (PBS and 0.1% Triton X-100, pH 7.6) at RT for 1 day to remove the SDS. The hearts were stained with wheat germ agglutinin (WGA) conjugated with an Alexa Fluor 594 (W11262, ThermoFisher Scientific, UK, dilution 1:100) for 1 day at RT. After three times (1 hour each) of washing in PBS at RT while gentle shaking, samples were fixed in 5 mL of PFA 4% at RT for 15 minutes to prevent WGA detachment. To remove exciding PFA residue, samples were rinsed three times (5 minutes each) in 5 mL of PBS at RT. Finally, the hearts were optically cleared with serial incubations in 50 mL of 20%, 47% and 68% (vol/vol) 2,2'-thiodiethanol (166782-500G, Sigma-Aldrich, US) in PBS (TDE/PBS). The incubations in 20% and 47% TDE/PBS were performed for 6 hours at RT while gently shaking, whereas the incubation in 68% TDE/PBS was executed O/N at 37°C while gently shaking [1].

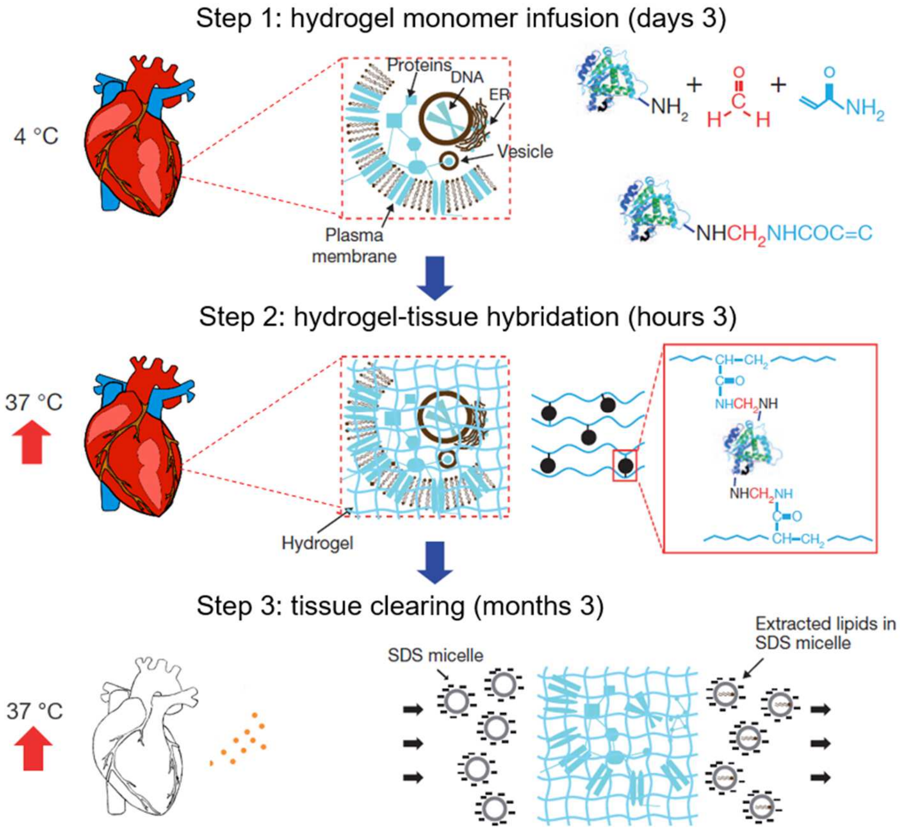

***Figure 37: PASSIVE CLARITY protocol.*** *Scheme showing the different steps of the PASSIVE CLARITY method. The first step consists in the perfusion of the sample with paraformaldehyde (red) and hydrogel monomers (blue). The hydrogel-tissue hybridization occurs in the second step. In the third step, the sample is washed in ionic detergent that passively transport micelles into, and lipids out of, the tissue, leaving fine-structure and cross-linked biomolecules in place. Modified from* [3]

## 10.7 Light-sheet microscope

Specimens were imaged using a custom-made light-sheet microscope [127] (see figure 38). The light sheet was generated by scanning the excitation beam with a galvanometric mirror (6220H, Cambridge Technology, MA) and confocality was achieved by synchronizing the galvo scanner with the line read-out of the sCMOS camera (Orca Flash 4.0, Hamamatsu Photonics, Japan). Five different wavelengths were available (MLDs and DPSSs, Cobolt, Sweden) for fluorescence excitation and an acousto-optic tunable filter (AOTFnC-400.650-TN, AA Opto-Electronic, France) was used to regulate laser power. The excitation light was focused with a long working distance, low magnification objective (10×, 0.3 NA, WD 17.5mm, Nikon, Japan) and fluorescence was collected on a perpendicular axis with a specialized objective for high refractive index immersion solutions with a correction collar for refractive indexes ranging from 1.41 to 1.52: the 10× Olympus objective (XLPLN10XSVMP, 10×, NA 0.6, WD 8 mm, Olympus, Japan). The samples were mounted on a motorized x-, y-, z-, ø -stage (M-122.2DD and M-116.DG, Physik Instrumente, Germany) which allowed free 3D motion plus rotation in a custom-made chamber filled with 68% TDE/PBS. The microscope was controlled via custom written LabVIEW code (National Instruments) using the Murmex package (Distrio, The Nederlands) which coordinated the galvo scanners, the rolling shutter and the stacks acquisition.

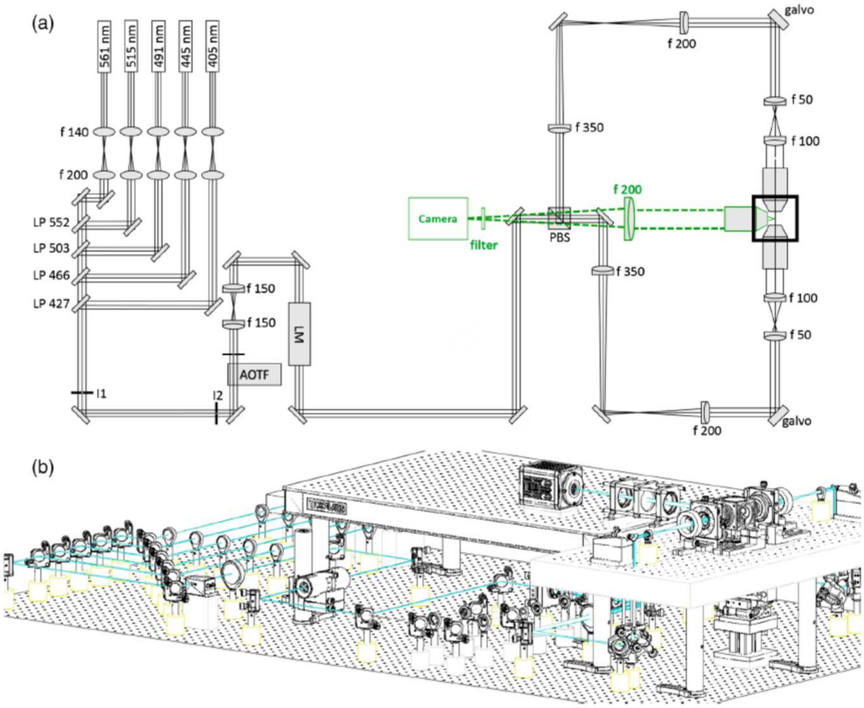

***Figure 38: LSM. (a)*** *Schematic of the light path. The galvo scanners are mounted above periscopes. LP: long-pass filter, I: iris, AOTF: acousto-optical tunable filter, LM: laser modulator, PBS: polarization beam splitter. Green dotted: detection path.* ***(b)*** *Oblique view of the microscope. A custom-made breadboard serves to mount the sample chamber and objectives at an elevated height and features two circular holes at the edges for the periscopes and a large central cut-out for the translation stages. A second breadboard is used for the camera. From* [127].

# 10.8 Imaging, image pre-processing and 3D reconstruction

The whole heart was imaged performing two acquisitions. Each acquisition corresponded to half a heart and was made by z-stacks of adjacent regions. Every stack had the depth equal to the thickness of half the analyzed heart (in a range of 5-7 mm) with a z step of 2 µm between images. Each frame had a field of view of (1.33×1.33) mm and a pixel size of (0.65×0.65) µm. Adjacent stacks had an overlap of 330 µm. Then, each stack was down sampled leading frames at a pixel size of (6×5.2×5.2) µm. The stacks were fused together in order to reconstruct the sample. ZetaStitcher (G. Mazzamuto, "ZetaStitcher: a software tool for high-resolution volumetric stitching"), was used for volumetric stitching (it was already described in the methods of the second part of this thesis, page ). Finally, the stacks are fused into a 3D reconstruction that correspond to half sample. The two 3D halves were fused together to reconstruct the whole heart. This blend was performed using ImageJ's plugin: Align3 TP. This datum was used to perform conduction fiber organization analysis. The same datum was also down sampled to a pixel size of (10×10.4×10.4) µm to execute segmentation. Moreover, raw data were compressed in JPEG2000 format to maintain the same resolution and reduce data size about 20 times to save the acquisition.

## 10.9 3D segmentation

To perform a 3D segmentation of the heart, a 2D analysis was applied at each frame with the pixel size of (10×10.4×10.4) µm using ImageJ's plugin: Trainable WEKA Segmentation 2D. This plugin is characterized by three phases. The first is the learning phase, in which the segmentation was performed manually on a frame and training features were selected to generate a model. This model was applied to all frames and a binary pixel classification map was generated during the classification phase. Finally, morphological operators were applied to the binary segmentation in order to delete artifacts and smooth the result.

## 10.10 Conduction fibers organization analysis

To analyze the conduction fibers organization of the whole heart the volume of the measure with the pixel size of (6×5.2×5.2) µm has been virtually decomposed in portions of (132×135.2×135.2) µm (see figure 39). To estimate conduction fibers orientation into each portion, a software based on the Structure Tensor Analysis has been developed. This method is an image analysis approach which derives a tensor from the distribution of image gradient directions within the neighborhood of each voxel [122]. The Structure Tensor Analysis is applied on every voxel, then the average tensor inside each portion is estimated. This analysis technique allowed to define a local orientation versor for each portion. Every versor corresponds to the conduction fibers direction into the portion analyzed. Furthermore, fractional anisotropy is collected to assess measure reliability. At the end of the Structure Tensor Analysis, the conduction fibers direction and the fractional anisotropy are determined through the entire 3D reconstruction. Subsequently, the volume of the measure has been virtually decomposed in portions of (528×540.8×540.8) µm to estimate local disarray. It is defined as (1-Alignment), where Alignment is the module of the average vector of local orientation versors. To calculate the average vector into each portion, weighted average of local orientation versors with their fractional anisotropy is performed. Finally, the global disarray of the whole volume is obtained averaging all local disarrays.

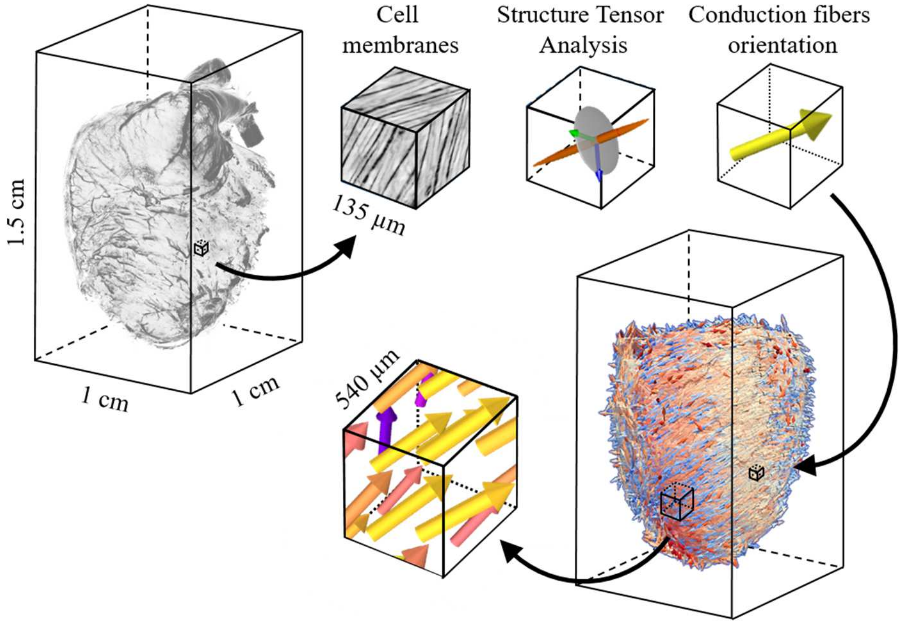

***Figure 39: Scheme of the 3D conduction fibers organization analysis.*** *The 3D reconstruction is virtually dissected in portions of about 135 µm. Inside each portion, a Structure Tensor Analysis is applied directly on the gray levels and the versor of 3D conduction fibers orientation is collected. Then, each orientation versor is re-allocated in a virtual volume to reconstruct the entire structural organization. The 3D reconstruction is virtually decomposed in portions of about 540 µm and local disarray is estimated inside each portion.*

# Chapter XI

# Results

This chapter reports the results obtained with innovative approaches, optical mapping and a clearing technique combined with LSM.

## 11.1 Functional investigation

A wide field mesoscope operating at 1.6 kHz was used to map the action potential propagation i0n Langendorff horizontally perfused mouse hearts stained with a red-shifted voltage sensitive dye (VSD, di-4-ANBDQPQ [128]). The hearts were electrically stimulated at the apex to follow action potential propagation along conduction fibers. Using a bipolar electrode, a burst of ten electrical stimuli at 10 Hz was delivered to the heart apex to overdrive the sinus rhythm. VSD mapping of electrically stimulated activity demonstrated uniform propagation from the apex to the base in CTRL mice. In R92Q mice a jagged action potential propagation from the apex to the surrounding myocardium after electrical stimulation (see figure 40) was observed.

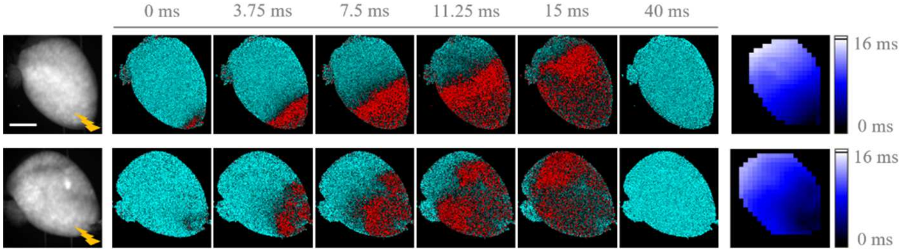

***Figure 40: Electrical stimulation in healthy and diseased whole mice hearts.*** *On the left, fluorescence images ($F_0$) of CTRL (top) and R92Q mice (bottom) hearts stained with VSD and stimulated at the apex with an electrode (yellow arrow). Scale bar 2 mm. Six representative frames of optical mapping ($\Delta F/F_0$) recorded from the same hearts. The electrical activation is reported in red and the baseline in cyan. On the right, corresponding colour-scale isochronal maps of the action potential reporting the activation time per pixel.*

The action potential propagation alteration was confirmed in diseased hearts, as shown in figure 41, from the maps generated by custom-made software in which the direction of action potential propagation for each pixel is represented by a vector. From all these vectors some parameters were calculated: conduction velocity (CV), SD mod and SD angle. As shown by graphs in figure 42a, there was not significant difference of the CV between R92Q and CTRL mice. Therefore, in R92Q mice SD mod, that is standard deviation of average conduction velocity, was significantly increased compared with CTRL mice. Moreover, SD angle, that is standard deviation of average angle, was significantly increased in R92Q compared with CTRL mice (see figures 42b and 42c). These results highlighted uniformity and homogeneity of action potential propagation in healthy hearts, and showed an alteration and heterogeneity of electrical activity in diseased hearts.

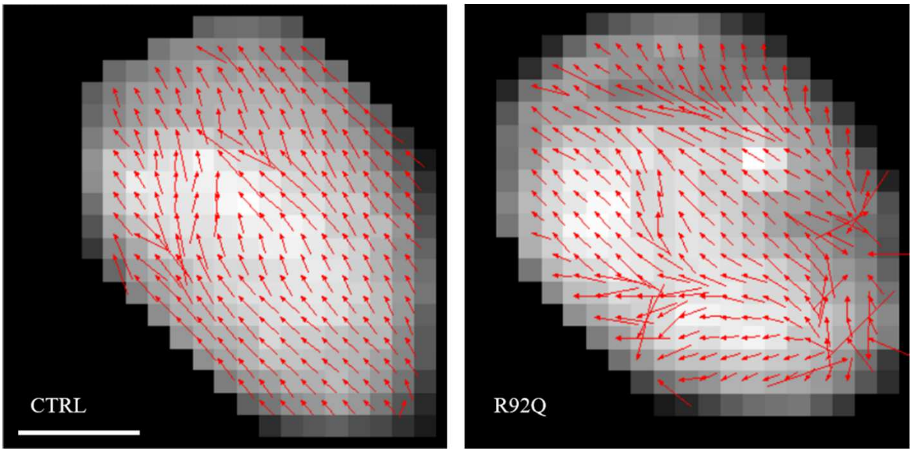

***Figure 41: Activation maps of healthy and diseased whole hearts.*** *Maps of CV and its modality of propagation of CTRL (left) and R92Q (right) mice. Scale bar 2 mm.*

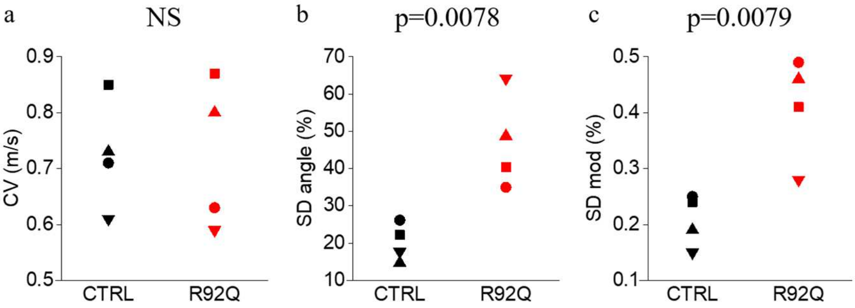

***Figure 42: Functional activity analysis. (a)*** *Graph showing conduction velocity of CTRL (black) and R92Q (red) hearts.* ***(b)*** *and* ***(c)*** *The graphs displaying the standard deviation of average conduction velocity and average angle in CTRL and R92Q mice. Each symbol corresponds to the same pair of animals. Statistical tests: Unpaired Student t tests.*

## 11.2 Structural investigation

Electrical dysfunction observed in the diseased hearts can be also related to macroscopical disorganization of conduction fibers. To exclude this hypothesis, a 3D architecture analysis of the samples was performed. To this aim, a protocol able to reconstruct the whole heart using a combination of advanced labeling, clearing and imaging techniques was developed.

### 11.2.1 Clearing, staining and imaging optimization

All samples that previously underwent functional measurements were structurally evaluated in a direct correlative manner. 3D whole heart reconstruction was achieved developing a clearing-staining-imaging-analysis pipeline to visualize conduction fibers. First, a clearing technique was optimized, PASSIVE CLARITY protocol [3], to render the heart optically transparent. The figure 43 shows an entire heart before and after application of the PASSIVE CLARITY method. This technique was able to render the heart transparent. The 3D conduction fiber reconstruction was based on cellular membrane labeling using WGA conjugated with a fluorophore. The developed protocol was able to stain the heart thought its whole thickness. A TDE based clearing method [1] was used to homogenize the refractive index of the tissue and reduce light scattering. The sample was acquired using a custom-made light-sheet microscope that allows mesoscopic reconstruction at micro-scale resolution (see figure 44). A volumetric stitching based on a global optimization algorithm was performed on the entire dataset using a custom-made Python software: ZetaStitcher (see figure 45).

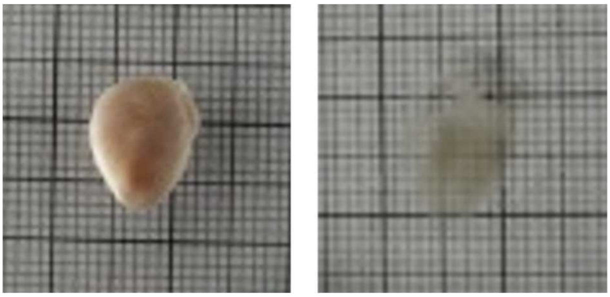

***Figure 43: Tissue clearing.*** *Images of whole heart in PBS before (left) and after (right) clearing with PASSIVE CLARITY protocol.*

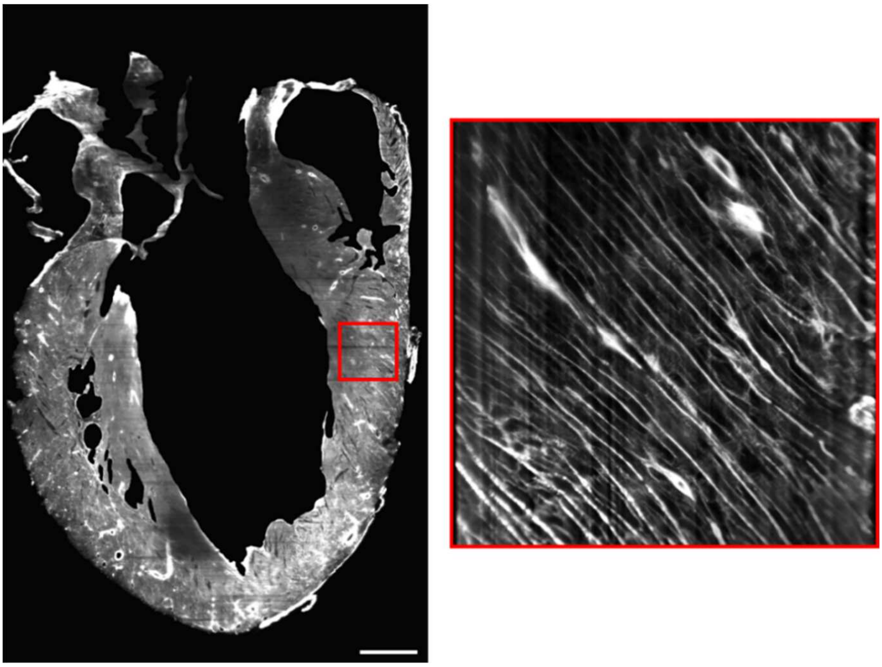

***Figure 44: Tissue labeling and imaging.*** *A reconstruction of a representative mouse heart treated with PASSIVE CLARITY protocol, stained with WGA, cleared with 68% TDE/PBS and imaged with LSM (Olympus, 10X objective) is represented. A magnification showing the sub-cellular resolution is displayed in the red square. Scale bar 1 mm.*

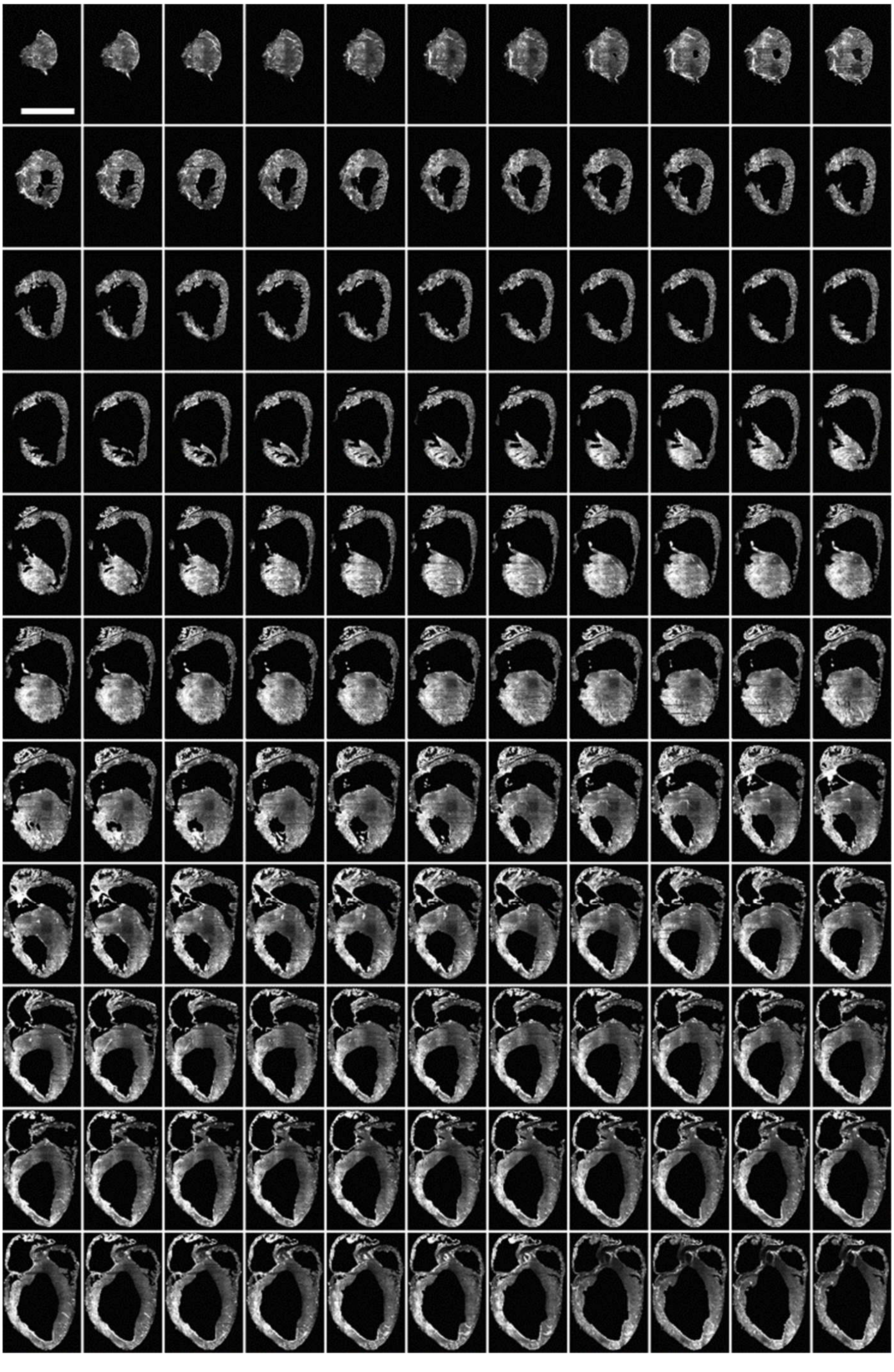

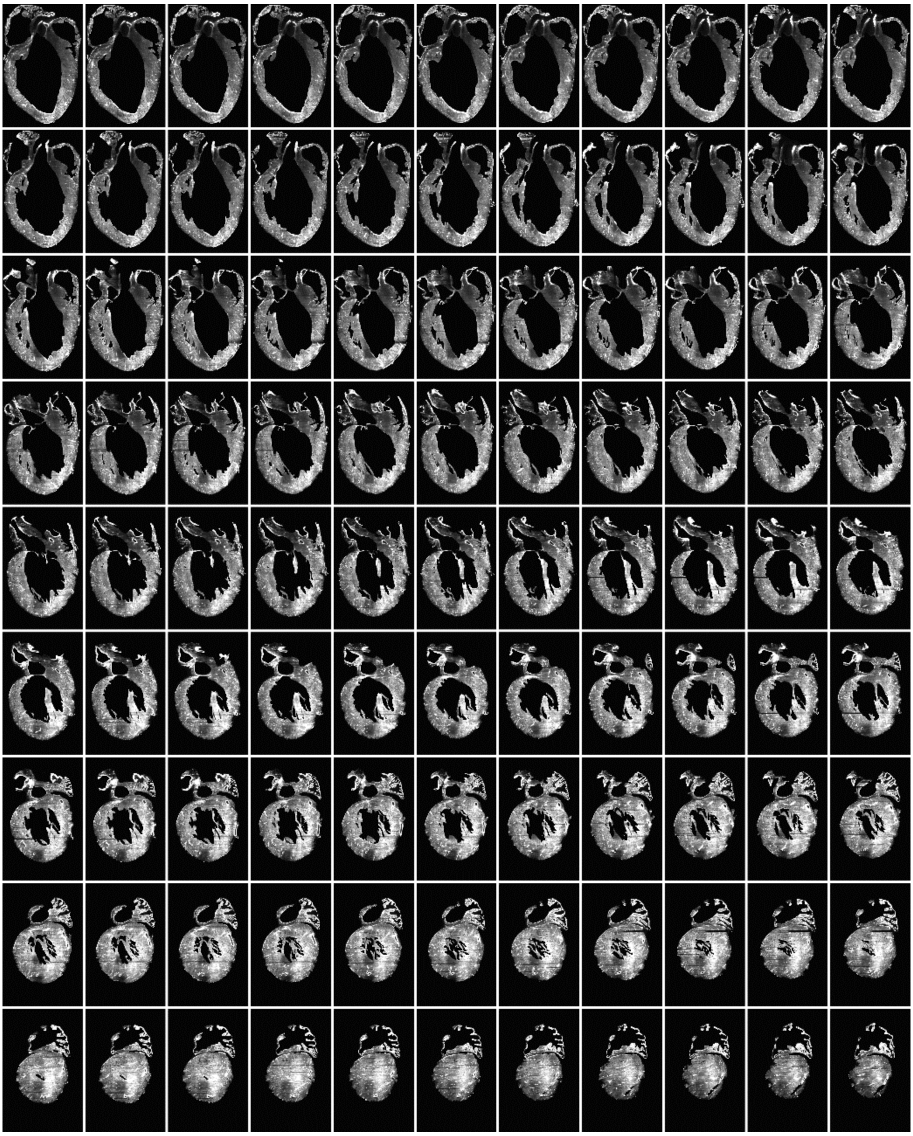

***Figure 45: Representative 3D reconstruction of whole mouse heart.*** *Frames in series of a whole mouse heart with a depth of 8 mm. There are 36 µm between a frame and its next. Sample was treated with PASSIVE CLARITY protocol, stained with WGA and cleared with 68% TDE/PBS, imaged with LSM (Olympus, 10X objective) and stitched with ZetaStitcher. Scale bar 5 mm.*

### 11.2.2 3D fibers orientation analysis

In order to reconstruct 3D conduction fibers organization of the whole mouse heart with micro-scale resolution, the two datasets, each corresponding to half of the heart, were fused. To this end, the ImageJ's plugin, Align3 TP was employed. Then, 3D volume was segmented using the ImageJ's plugin, Trainable WEKA Segmentation. Subsequently, to quantify conduction fibers orientation across the whole heart in 3D, the entire volume was virtually dissected in portions (132 × 135.2 × 135.2) µm and the cell disposition inside each virtual block was estimated with Structure Tensor Analysis. Finally, 3D reconstruction is virtually decomposed in portions (528×540.8×540.8) µm and local disarray is calculated inside each portion. In figure 46 the result obtained applying this analysis at whole heart level in a control and in a diseased heart is shown. In R92Q mouse the global disarray, obtained averaging all local disarrays, is higher than in CTRL. An increased disarray in HCM mouse model was expected based on previous anatomical studies in literature and functional recordings performed in this thesis work. However, this is a preliminary investigation to validate clearing and imaging techniques. Further analysis to quantify global disarray in control and diseased hearts are necessary to confirm this result.

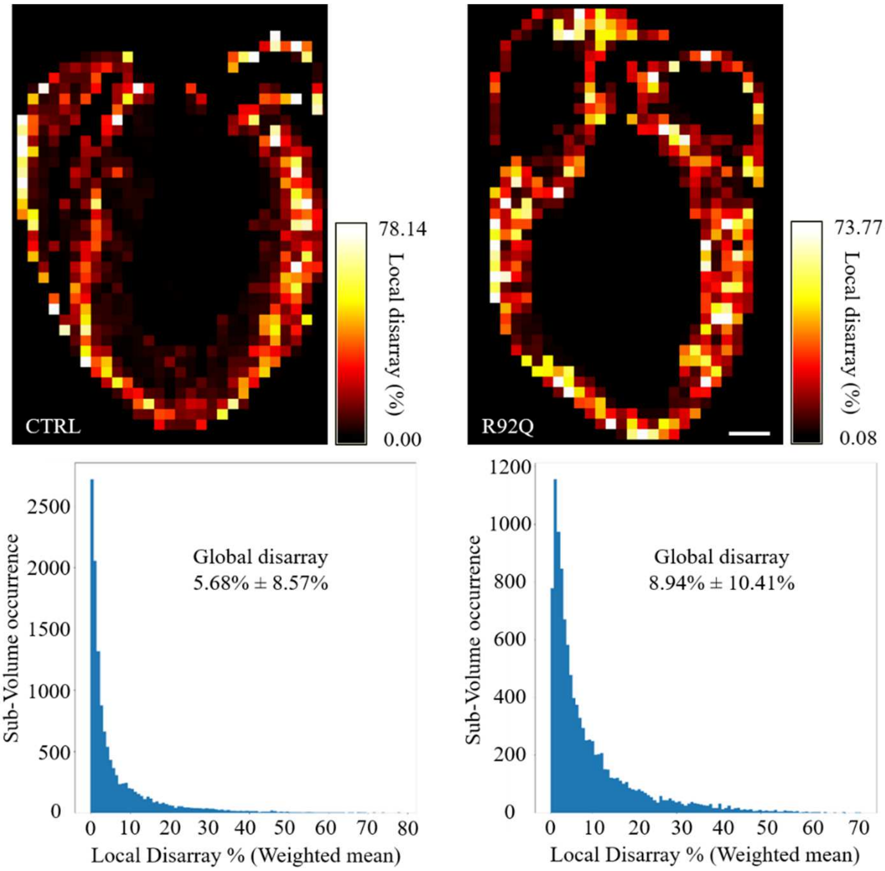

***Figure 46: Representations of local disarray at whole heart level.*** *Representative local disarray maps (top) and relative distributions (bottom) of a CTRL and a R92Q hearts are shown. Red color scales correspond to a different disarray degree. Global disarray and standard deviation are indicated for each heart. Scale bar 1 mm.*

# Chapter XII

# Discussion

A HCM mouse model carrying the R92Q TNNT2 mutation has been investigated for functional and structural aspects. This model has been previously characterized with echocardiography showing LV hypertrophy, enhanced contractility and diastolic dysfunction [88]. Moreover, findings from echocardiographic measurements, performed in this previous work [88], showed that several hallmarks of human HCM phenotype (increased septal thickness, increased ejection fraction and diastolic dysfunction) are present in this HCM mouse model. For these reasons, in this thesis work, R92Q pathological model has been undergone to electrical measurements and structural investigations to assess whether complex functional and structural remodelling are correlated.

An ultrafast wide field macroscope was employed to optically map action potential propagation with a red-shifted voltage sensitive dye in whole mouse heart. Using a bipolar electrode, a burst of electrical stimuli was delivered to the heart apex to control cardiac electrical activity. Following, action potential propagation alterations were observed in diseased hearts. Moreover, some parameters were calculated: conduction velocity, SD mod and SD angle. Despite, no significant difference was observed in conduction velocity between control and diseased hearts; the R92Q mouse model showed significant differences in SD mod and SD angle with respect to control. These results demonstrated a uniform and homogenous action potential propagation along conduction fibers in control hearts, and a jagged and heterogeneous action potential propagation from the apex to the surrounding myocardium after electrical stimulation in diseased hearts.

However, to correlate these electrical dysfunctions with structural alterations at whole heart level it is necessary to performed high-resolution imaging. For this purpose, in this thesis work, a clearing method, named PASSIVE CLARITY protocol [3], was optimized to clear the entire heart. Applying this technique based on tissue transformation, it was possible to make the heart transparent without the sample undergoing size changes such as shrinkage or swelling. Moreover, cellular membranes were labelled with WGA to visualize conduction fibers and a TDE based clearing method [1] was used to homogenize the refractive index of the tissue and reduce light scattering during imaging performed with a custom-made light-sheet microscope. Combining these techniques, a mesoscopic reconstruction with micron-scale resolution of the whole heart was performed and an uniform labelling was obtained throughout the thickness of the cardiac walls. Finally, imaging data were submitted to Structure Tensor Analysis to estimate 3D conduction fibers orientation and to investigate structural parameters, such as fibers alignment and local disarray. These parameters were fundamental to estimate global disarray in the whole 3D reconstruction.

In the future, an analysis software will be developed to correlate 2D maps of action potential propagation with 3D reconstruction of whole mouse heart with micron-scale resolution.

# Part IV

## Conclusions

# Chapter XIII

# Conclusions and future perspectives

In conclusion, in this thesis project, clearing-imaging-analysis pipeline was developed and applied to visualize cardiac conduction pathway in three-dimensions and multi-technique approaches were employed to correlate electro-mechanical dysfunctions with structural alterations. In detail, tissue clearing methods, together with high-resolution microscopic imaging and subsequent image analysis, were used to study cardiac structure with micron-scale resolution and correlate it with functional investigations, in particular, with energetic and mechanical measurements in human muscles strips and action potential propagation in a mouse model at whole heart level.

For the future, these pipelines can be applied to investigate the structure at whole heart level in small animal models (mouse and rat), but also to study the structure in biopsies from big animals (pig and rabbit) and human. Moreover, it is possible investigate different cardiac pathologies such as: cardiomyopathies, myocardial infarction, heart failure and so on; and more interestingly, what they entail at structural level. Indeed, it would be interesting to study what are the effects of cardiomyopathies on heart muscle, for example, are cells to increase/reduce in number or in dimensions to induce hypertrophy or dilatation? And is the fibrosis to induce a stiffening in restrictive cardiomyopathy? Another interesting aspect may be to investigate which cells are involved in the border zone of the infarcted area in myocardial infarction. All these investigations are made possible thanks to developed pipeline. Indeed, different antibodies direct to a specific epitope can be used to perform a homogeneously staining, thus the structures of interest are highlighted.

The capability to perform immuno-staining in large volumes of cardiac tissue or in entire hearts is made possible thanks to the PASSIVE CLARITY protocol [3] optimized, during this thesis work, on the cardiac muscle tissue. Moreover, to investigate structural characteristics with cellular or sub-cellular resolution, high-throughput microscopy imaging systems are employed, such as LSM and TPFM. These imaging techniques have to be coupled with clearing solvent (TDE) [1] to match the refractive index and reduce the scattering. Finally, to analyse the features of interest, the analysis software will be implemented. Therefore, not only cellular alignment and local disarray will be investigated, but also cellular dimensions and number of cells, local fibrosis, the interaction between cardiomyocytes and other cells such as myofibroblasts, fibroblasts, macrophages and so on. Moreover, it would be interesting to know the relationship between cardiomyocytes and capillary network as well as the distribution and the radius size of capillaries, arteries and veins in diseased that involve blood vessels.

In conclusion, this clearing-imaging-analysis pipeline, developed in this thesis project, allows to perform structural investigations concerning different heart diseases and to correlate them with electro-mechanical dysfunction.

# Appendix A

# Fluorescence microscopy

Fluorescence is the emission of light that occurs within nanoseconds after the absorption of light with a shorter wavelength. The difference between the exciting and emitted wavelengths, known as the Stokes shift, is the property that permits the detection of signals. By filtering out the exciting light without screening the emitted fluorescence, it is possible to see only the objects that are fluorescent, while the rest, not labelled cellular components, provide a black background. Despite many organic substances have intrinsic fluorescence (autofluorescence), fluorescence microscopy usually exploits synthesized compounds (fluorophores). The energy states of a molecule can be displayed graphically using the Alexander Jablonski diagram (see figure 48). When a fluorophore absorbs light, all the photon energy is transferred to the fluorophore. This energy is inversely related to the exciting wavelength $E=hc/\lambda$, where h is Plank's constant and c and $\lambda$ are the speed and wavelength of light in vacuum, respectively. For each given fluorophore there is a range of wavelengths, excitation spectrum, that can excite it. Before the molecule fluoresces to reach back $S_0$, part of the absorbed energy gets dissipated because of internal conversion and vibrational relaxation. It is the origin of the Stokes shift and varies from one fluorophore to another. The basic concept of a fluorescence microscope is to irradiate the sample and to detect the fluorescence emitted.

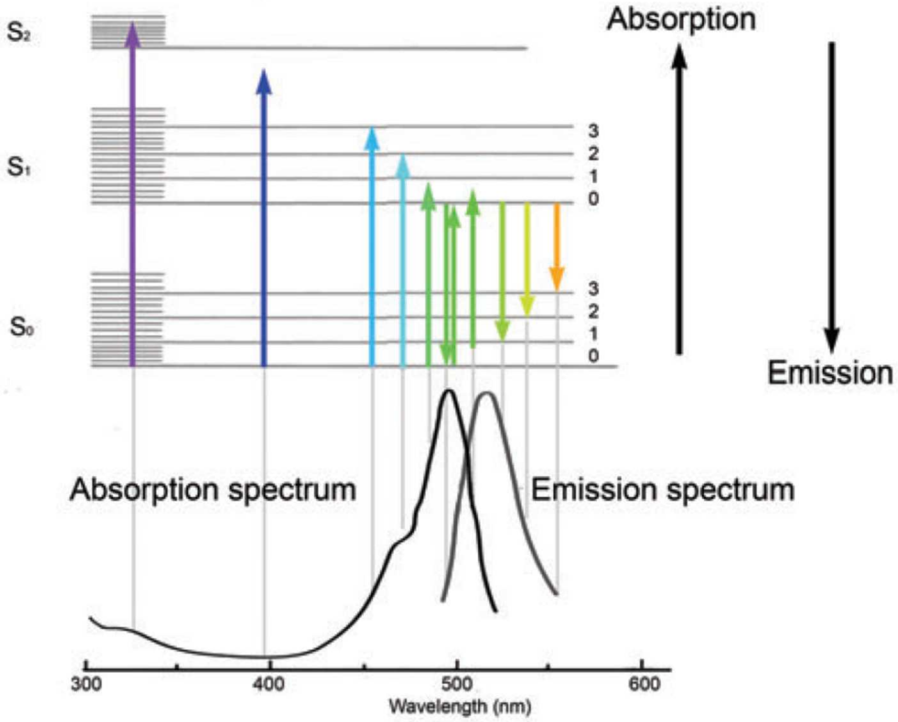

***Figure 48: Jablonski's diagram.*** *Scheme depicting the spectral characteristics related to absorption and emission of energy by a molecule. Molecules not absorbing energy are mainly confined to the lowest vibrational states of the ground state S0. Each vertical gray line aligns the spectra with the energy of the absorbed (arrows pointing up) or emitted (arrows pointing down) photons. The arrows are coloured to represent the wavelength of the photons. From* [129].

# Bibliography

1. Costantini I., Ghobril J. P., Di Giovanna A. P., Allegra Mascaro A. L., Silvestri L., Mullenbroich M. C., Onofri L., Conti V., Vanzi F., Sacconi L., Guerrini R., Markram H., Iannello G. and Pavone F. S. *A versatile clearing agent for multi modal brain imaging*. Scientific Reports 5, 9808 (2015).
2. Crocini C., Ferrantini C., Coppini R., Scardigli M., Yan P., Loew L. M., Smith G., Cerbai E., Poggesi C., Pavone F. S. and Sacconi L. *Optogenetics design of mechanistically-based stimulation patterns for cardiac defibrillation.* Scientific Reports 6, 35628 (2016).
3. Chung K., Wallace J., Kim S. Y., Kalyanasundaram S., Andalman A. S., Davidson T. J., Mirzabekov J. J., Zalocusky K. A., Mattis J., Denisin A. K., Pak S., Bernstein H., Ramakrishnan C., Grosenick L., Gradinaru V. and Deisseroth K. *Structural and molecular interrogation of intact biological systems.* Nature 497, 332-339 (2013).
4. Ho C. Y. *Hypertrophic Cardiomyopathy: For Heart Failure Clinics: Genetics of Cardiomyopathy and Heart Failure*. Heart Failure Clinics 6, 141-159 (2010).
5. Maron B. J. *Hypertrophic cardiomyopathy. A systematic review.* The Journal of the American Medical Association 287, 1308-1320 (2002).
6. Rajendran P. S., Challis R. C., Fowlkes C. C., Hanna P., Tompkins J. D., Jordan M. C., Hiyari S., Gabris-Weber B. A., Greenbaum A., Chan K. Y., Deverman B. E., Munzberg H., Ardell J. L., Salama G., Gradinaru V. and Shivkumar K. *Identification of peripheral neural cisrcuits that regulate heart*

*rate using optogenetic and viral vector strategies*. Nature Communications 10, 1944 (2019).

7. Minsky M. *Memoir on inventing the confocal scanning microscope*. Scanning 10, 128-138 (1988).
8. Denk W., Strickler J. H. and Webb W. W. *Two-photon laser scanning fluorescence microscopy*. Science 248, 73-76 (1990).
9. Keller P. J. and Dodt H. U. *Light sheet microscopy of living or cleared specimens*. Current Opinion in Neurobiology 22, 138-143 (2012).
10. Silvestri L., Costantini I., Sacconi L. and Pavone F. S. *Clearing of fixed tissue: a review from a microscopist's perspective.* Journal of Biomedical Optics 21, 081205 (2016).
11. http://www.lpch.org/DiseaseHealthInfo/HealthLibrary/cardiac/0243-pop.html.
12. https://www.pinterest.it/pin/122934264805295331.
13. http://www.yalemedicalgroup.org/stw/Page.asp?PageID=STW022865.
14. Katz A. M. *Physiology of the heart*. Fifth edition. Lippincott Williams & Wilkins.
15. Hodgkin A. L., Huxley A. F. and Katz B. *Measurement of current-voltage relations in the membrane of the giant axon of Loligo*. The Journal of Physiology 116, 424-448 (1952).
16. Kurtenbach S., Kurtenbach S. and Zolid G. *Gap junction modulation and its implications for heart function*. Frontiers in Physiology 5, 82 (2014).
17. http://www.cvphysiology.com/Arrhytmias/A004.
18. Bers, D. M. *Excitation-Contraction Coupling and Cardiac Contractile Force*. Second edition. Kluwer Academic Publishers.
19. Kushnir A. and Marks A. R. *The ryanodine receptor in cardiac physiology and disease*. Advances in Pharmacology 59, 1-30 (2010).

20. Sham J. S., Cleemann L. and Morad M. *Functional coupling of Ca2+ channels and ryanodine receptors in cardiac myocytes*. Proceedings of the National Academy of Sciences of the United States of America 92, 121-125 (1995).
21. Sipido K. R. and Callewaert G. *How to measure intracellular [Ca2+] in single cardiac cells with fura-2 or indo-1*. Cardiovascular Research 29, 717-726 (1995).
22. Bers D.M. *Cardiac sarcoplasmic reticulum calcium leak: basis and roles in cardiac dysfunction*. Annual Review of Physiology 76, 107-127 (2014).
23. Wier W. G. and Balke C. W. *Ca(2+) release mechanisms, Ca(2+) sparks, and local control of excitation-contraction coupling in normal heart muscle*. Circulation Research 85, 770-776 (1999).
24. Bassani, J. W. Yuan W. and Bers D. M. *Fractional SR Ca release is regulated by trigger Ca and SR Ca content in cardiac myocytes*. The American Journal of Physiology 268, C1313-1319 (1995).
25. Eisner D. A., Trafford A. W., Diaz M. E., Overend C. L. and O'Neill S. C. *The control of Ca release from the cardiac sarcoplasmic reticulum: regulation versus autoregulation*. Cardiovascular Research 38, 589-604 (1998).
26. Huxley H. E. *The double array of filaments in cross-striated muscle*. The Journal of Biophysical and Biochemical Cytology 3, 631-648 (1957).
27. Gregorio C. C. and Antin P. B. *To the heart of myofibril assembly*. Trends in Cell Biology 10, 355-362 (2000).
28. Swartz D. R., Yang Z., Sen A., Tikunova S. B. and Davis J. P. *Myofibrillar troponin exists in three states and there is signal transduction along skeletal myofibrillar thin filaments*. Journal of Molecular Biology 361, 420-435 (2006).

29. Gordon A. M., Homsher E. and Regnier M. *Regulation of contraction in striated muscle*. Physiological Reviews 80, 853-924 (2000).
30. Huxley H. E. *Fifty years of muscle and the sliding filament hypothesis*. European Journal of Biochemistry 271, 1403-1415 (2004).
31. Murphy C. T., Rock R. S. and Spudich J. A. *A myosin II mutation uncouples ATPase activity from motility and shortens step size*. Nature Cell Biology 3, 311-315 (2001).
32. Seidman J. G. and Seidman C. *The genetic basis for cardiomyopathy: from mutation identification to mechanistic paradigms*. Cell 104, 557-567 (2001).
33. Marian A. J. and Roberts R. *The molecular genetic basis for hypertrophic cardiomyopathy*. Journal of Molecular and Cellular Cardiology 33, 655-670 (2001).
34. Rayment I., Holden H. M., Whittaker M., Yohn C.B., Lorenz M., Holmes K.C. and Milligan R. A. *Structure of the actin-myosin complex and its implications for muscle contraction.* Science 261, 58-65 (1993).
35. Tyska M. J., Hayes E., Giewat M., Seidman C. E., Seidman J. G. and Warsham D. M. *Single molecule mechanics of R403Q cardiac myosin isolated from the mouse model of familial hypertrophic cardiomyopathy*. Circulation Research 86, 737-744 (2000).
36. Tardiff J. C. *Sarcomeric proteins and familial hypertrophic cardiomyopathy: linking mutations in structural proteins to complex cardiovascular phenotypes*. Heart Failure Reviews 10, 237-248 (2005).
37. Freiburg A. and Gautel M. *A molecular map of the interactions between titin and myosin-binding protein C. Implications for sarcomeric assembly in familial hypertrophic cardiomyopathy.* European Journal of Biochemistry 235, 317-323 (1996).

38. Niimura H., Patton K. K., McKenna W. J., Soults J., Maron B. J., Seidman J. G. and Seidman C. E. *Sarcomere protein gene mutations in hypertrophic cardiomyopathy of the elderly*. Circulation 105, 446-451 (2002).
39. Moolman J.C., Corfield V.A., Posen B., Ngumbela K., Seidman C., Brink P. A. and Watkins H. *Sudden death due to troponin T mutations*. Journal of the American College of Cardiology 29, 549-555 (1997).
40. Watkins H., McKenna W.J., Thierfelder L., Suk H. J., Anan R., O'Donoghue A., Spirito P., Matsumori A., Moravec C. S., Seidman J. G. and Seidman C. E. *Mutations in the genes for cardiac troponin T and alpha-tropomyosin in hypertrophic cardiomyopathy*. The New England Journal of Medicine 332, 1058-1064 (1995).
41. Knollmann B. C. and Potter J. D. *Altered regulation of cardiac muscle contraction by troponin T mutations that cause familial hypertrophic cardiomyopathy*. Trends in Cardiovascular Medicine 11, 206-212 (2001).
42. Yan P. Acker C. D., Zhou W. L., Lee P., Bollensdorff C., Negrean A., Lotti J., Sacconi L., Antic S. D., Kohl P., Mansvelder H. D., Pavone F.S. and Loew L.M. *Palette of fluorinated voltage-sensitive hemicyanine dyes*. Proceedings of the National Academy of Sciences of the United States of America 109, 20443-20448 (2012).
43. Peterka D. S., Takahashi H. and Yuste R. *Imaging voltage in neurons*. Neuron 69, 9-21 (2011).
44. Denk W., Strickler J. H. and Webb W. W. *Two-photon laser scanning fluorescence microscopy*. Science 248, 73-6 (1990).
45. Zipfel W. R., Williams R. M. and Webb W. W. *Nonlinear magic: multiphoton microscopy in the biosciences*. Nature Biotechnology 21, 1369-1377 (2003).

46. Helmchen F. and Denk W. *Deep tissue two-photon microscopy.* Nature Methods 2, 932-940 (2005).
47. Svoboda K. and Yasuda R. *Principles of two-photon excitation microscopy and its applications to neuroscience.* Neuron 50, 823-839 (2006).
48. So P. T. C. *Two-photon fluorescence light microscopy.* Encyclopaedia of Life Sciences - Macmillan Publishers Ltd, Nature Publishing Group (2002).
49. Ragan T., Kadiri L. R., Venkataraju K. U., Bahlmann K., Sutin J., Taranda J., Arganda-Carreras I., Kim Y., Seung H. S. and Osten P. *Serial two-photon tomography for automated ex vivo mouse brain imaging.* Nature Methods 9, 255-258 (2012).
50. Osten P. and Margrie T. W. *Mapping brain circuitry with a light microscope.* Nature Methods 10, 515-523 (2013).
51. Huisken J., Swoger J., Del Bene F., Wittbrodt J. and Stelzer E. H. *Optical sectioning deep inside live embryos by selective plane illumination microscopy.* Science 305, 1007-1009 (2004).
52. Dodt H. U., Leischner U., Schierloh A., Jahrling N., Mauch C. P., Deininger K., Deussing J. M., Eder M., Zieglgansberger W. and Becker K. *Ultramicroscopy: three-dimensional visualization of neuronal networks in the whole mouse brain.* Nature Methods 4, 331-336 (2007).
53. Huisken J. and Stainier D. Y. *Selective plane illumination microscopy techniques in developmental biology.* Development 136, 1963-1975 (2009).
54. Leischner U., Zieglgansberger W. and Dodt H. U. *Resolution of ultramicroscopy and field of view analysis.* PLoS One 4, 5785 (2009).
55. Richardson D. S. and Lichtman J. W. *Clarifying tissue clearing.* Cell 162, 246-257 (2015).
56. Huffman D. R. and Bohren C. F. *Absorption and scattering of light by small particles.* Wiley (1983).

57. Kao F. and Torok P. *Optical imaging and microscopy.* Number 2nd edition, Springer (2007).
58. Hecht E. *Optics.* Number 2nd edition, Addison Wesley (1987).
59. Silvestri L. *Confocal ultramicroscopy: micron-scale neuroanatomy of the entire mouse brain.* PhD thesis.
60. Spalteholz W. *Uber das Durchsichtigmachen von menschlichen und tierischen Praparaten.* Uber das Durchsichtigmachen von menschlichen und tierischen Praparaten. S. Hierzel (1914).
61. Becker K., Jahrling N., Saghafi S., Weiler R. and Dodt H. U. *Chemical clearing and dehydration of gfp expressing mouse brains.* PLoS One 7, e33916 (2012).
62. Erturk A., Becker K., Jahrling N., Mauch C. P., Hojer C. D., Egen J. G., Hellal F., Bradke F., Sheng M. and Dodt H. U. *Three-dimensional imaging of solvent-cleared organs using 3disco.* Nature Protocols 7, 983-995 (2012).
63. Renier N., Wu Z., Simon D. J., Yang J., Ariel P. and Tessier-Lavigne M. *idisco: a simple, rapid method to immunolabel large tissue samples for volume imaging.* Cell 159, 896-910 (2014).
64. Schwarz M. K., Scherbarth A., Sprengel R., Engelhardt J., Theer P. and Giese G. *Fluorescent-protein stabilization and high-resolution imaging of cleared, intact mouse brains.* PLoS One 10, 1-26 (2015).
65. Tsai P. S., Kaufhold J. P., Blinder P., Friedman B., Drew P. J., Karten H. J., Lyden P. D. and Kleinfeld D. *Correlations of neuronal and microvascular densities in murine cortex revealed by direct counting and colocalization of nuclei and vessels.* Journal of Neuroscience 29, 14553-14570 (2009).
66. Ke M. T., Fujimoto S. and Imai T. *SeeDB: a simple and morphology-preserving optical clearing agent for neuronal circuit reconstruction.* Nature Neuroscience 16, 1154-1161 (2013).

67. Hou B., Zhang D., Zhao S., Wei M., Yang Z., Wang S., Wang J., Zhang X., Liu B., Fan L., Li Y., Qiu Z., Zhang C. and Jiang T. *Scalable and Dil-compatible optical clearance of the mammalian brain.* Frontiers in Neuroanatomy 9, 19 (2015).
68. Aoyagi Y., Kawakami R., Osanai H., Hibi T. and Nemoto T. *A rapid optical clearing protocol using 2,2'-thiodiethanol for microscopic observation of fixed mouse brain.* PLoS One 10, e0116280 (2015).
69. Staudt T., Lang M. C., Medda R., Engelhardt J. and Hell S. W. *2,2'-thiodiethanol: a new water soluble mounting medium for high resolution optical microscopy.* Microscopy Research and Technique 70, 1-9 (2007).
70. Hama H., Kurokawa H., Kawano H., Ando R., Shimogori T., Noda H., Fukami K., Sakaue-Sawano A. and Miyawaki A. *Sca/e: a chemical approach for fluorescence imaging and reconstruction of transparent mouse brain.* Nature Neuroscience 14, 1481-1488 (2011).
71. Hama H., Hioki H., Namiki K., Hoshida T., Kurokawa H., Ishidate F., Kaneko T., Akagi T., Saito T., Saido T. and Miyawaki A. *Sca/eS: an optical clearing palette for biological imaging.* Nature Neuroscience 18, 1518 (2015).
72. Kuwajima T., Sitko A. A., Bhansali P., Jurgens C., Guido W. and Mason C. *Clear(T): a detergent- and solvent-free clearing method for neuronal and non-neuronal tissue.* Development 140, 1364-1368 (2013).
73. Tainaka K., Kubota S. I., Suyama T. Q., Susaki E. A., Perrin D., Ukai-Tadenuma M., Ukai H. and Ueda H. R. *Whole-body imaging with single-cell resolution by tissue decolorization.* Cell 159, 911-924 (2014).
74. Susaki E. A., Tainaka K., Perrin D., Kishino F., Tawara T., Watanabe T. M., Yokoyama C., Onoe H., Eguchi M., Yamaguchi S., Abe T., Kiyonari H., Shimizu Y., Miyawaki

A., Yokota H. and Ueda H. R. *Whole-brain imaging with single-cell resolution using chemical cocktails and computational analysis.* Cell 157, 726-739 (2014).

75. Yang B., Treweek J. B., Kulkarni R. P., Deverman B. E., Chen C. K., Lubeck E., Shah S., Cai L. and Gradinaru V. *Single-cell phenotyping within transparent intact tissue through whole-body clearing.* Cell 158, 945-958 (2014).
76. Kim S. Y., Cho J. H., Murray E., Bakh N., Choi H., Ohn K., Ruelas L., Hubbert A., McCue M., Vassallo S. L., Keller P. J. and Chung K. *Stochastic electrotransport selectively enhances the transport of highly electromobile molecules.* Proceedings of the National Academy of Science of the United States of America 112, E6274-E6283 (2015).
77. Murray E. Cho J. H., Goodwin D., Ku T., Swaney J., Kim S. Y., Choi H., Park Y. G., Park J. Y., Hubbert A., McCue M., Vassallo S., Bakh N., Frosch M. P., Wedeen V. J., Seung H. S. and Chung K. *Simple, scalable proteomic imaging for high-dimensional profiling of intact systems.* Cell 163, 1500-1514 (2015).
78. Sivaguru M., Fried G., Sivaguru B. S., Sivaguru V. A., Lu X., Choi K. H., Saif M. T. A., Lin B. and Sadayappan S. *Cardiac muscle organization revealed in 3-D by imaging whole-mount mouse hearts using two-photon fluorescence and confocal microscopy.* Biotechniques 59, 295-308 (2015).
79. Lee S. E., Nguyen C., Yoon J., Chang H. J., Kim S., Kim C. H. and Li D. *Three-dimensional cardiomyocytes structure revealed by diffusion tensor imaging and its validation using a tissue-clearing technique.* Scientific Reports 8, 1-11 (2018).
80. Semsarian C., Ingles J., Maron M. S. and Maron B.J. *Reply: What is the true prevalence of Hypertrophic Cardiomyopathy?* Journal of the American College of Cardiology 66, 1846-1847 (2015).

81. Maron B. J. and Maron M. S. *Hypertrophic cardiomyopathy.* Lancet 381, 242-255 (2013).
82. Ho C. Y., Charron P., Richard P., Girolami F., Van Spaendonck-Zwarts K. Y. and Pinto Y. *Genetic advances in sarcomeric cardiomyopathies: state of the art.* Cardiovascular Research 105, 397-408 (2015).
83. Witjas-Paalberends E. R., Ferrara C., Scellini B., Piroddi N., Montag J., Tesi C., Stienen G. J., Michels M., Ho C. Y., Kraft T., Poggesi C. and van der Velden J. *Faster cross-bridge detachment and increased tension cost in human hypertrophic cardiomyopathy with the R403Q MYH7 mutation.* The Journal of Physiology 592, 3257-3272 (2014).
84. Belus A., Piroddi N., Scellini B., Tesi C., D'Amati G., Girolami F., Yacoub M., Cecchi F., Olivotto I. and Poggesi C. *The familial hypertrophic cardiomyopathy-associated myosin mutation R403Q accelerates tension generation and relaxation of human cardiac myofibrils.* The Journal of Physiology 586, 3639-3644 (2008).
85. Piroddi N., Witjas-Paalberends E. R., Ferrara C., Ferrantini C., Vitale G., Scellini B., Wijnker P. J. M., Sequiera V., Dooijes D., Dos Remedios C., Schlossarek S., Leung M. C., Messer A., Ward D. G., Biggeri A., Tesi C., Carrier L., Redwood C. S., Marston S. B., van der Velden J. and Poggesi C. *The homozygous K280N troponin T mutation alters cross-bridge kinetics and energetics in human HCM.* The Journal of General Physiology 151, 18-29 (2018).
86. Ashrafian H., Redwood C., Blair E. and Watkins H. *Hypertrophic cardiomyopathy: a paradigm for myocardial energy depletion.* Trends in Genetics 19, 263-268 (2003).
87. Ferrantini C., Coppini R., Pioner J. M., Gentile F., Tosi B., Mazzoni L., Scellini B., Piroddi N., Laurino A., Santini L., Spinelli V., Sacconi L., De Tombe P., Moore R., Tardiff

J., Mugelli A., Olivotto I., Cerbai E., Tesi C. and Poggesi C. *Pathogenesis of Hypertrophic Cardiomyopathy is Mutation Rather Than Disease Specific: A Comparison of the Cardiac Troponin T E163R and R92Q Mouse Models.* Journal of the American Heart Association 6, 1-19 (2017).

88. Jung J., Oh J. and Lee K. *Nucleotide and deduced amino acid sequences of rat myosin binding protein H (MyBP-H).* Archives of Pharmacal Research 21, 712-717 (1998).
89. Crilley J. G., Boehm E. A., Blair E., Rajagopalan B., Blamire A. M., Styles P., McKenna W. J., Ostman-Smith I., Clarke K. and Watkins H. *Hypertrophic cardiomyopathy due to sarcomeric gene mutations is characterized by impaired energy metabolism irrespective of the degree of hypertrophy.* Journal of the American College of Cardiology 41, 1776-1782 (2003).
90. Spindler M., Saupe K. W., Christe M. E., Sweeney H. L., Seidman C. E., Seidman J. G. and Ingwall J. S. *Diastolic dysfunction and altered energetics in the alphaMHC403/+ mouse model of familial hypertrophic cardiomyopathy.* The Journal of Clinical Investigation 101, 1775-1783 (1998).
91. Javadpour M. M., Tardiff J. C., Pinz I. and Ingwall J. S. *Decreased energetics in murine hearts bearing the R92Q mutation in cardiac troponin T.* The Journal of Clinical Investigation 112, 768-775 (2003).
92. Chandra M., Tschirgi M. L. and Tardiff J. C. *Increase in tension-dependent ATP consumption induced by cardiac troponin T mutation.* American Journal of Physiology-Heart Circulatory Physiology 289, 2112-2119 (2005).
93. Luedde M., Flögel U., Knorr M., Grundt C., Hippe H. J., Brors B., Frank D., Haselmann U., Antony C., Voelkers M., Schrader J., Most P., Lemmer B., Katus H. A. and Frey N. *Decreased contractility due to energy deprivation in a transgenic rat model*

*of hypertrophic cardiomyopathy.* Journal of Molecular Medicine 87, 411-422 (2009).

94. Witjas-Paalberends E. R., Güçlü A., Germans T., Knaapen P., Harms H. J., Vermeer A. M., Christiaans I., Wilde A. A., Dos Remedios C., Lammertsma A. A., van Rossum A. C., Stienen G. J., van Slegtenhorst M., Schinkel A. F., Michels M., Ho C. Y., Poggesi C. and van der Velden J. *Gene-specific increase in the energetic cost of contraction in hypertrophic cardiomyopathy caused by thick filament mutations.* Cardiovascular Research 103, 248-457 (2014).
95. He H., Javadpour M. M., Latif F., Tardiff J. C. and Ingwall J. S. *R-92L and R-92W mutations in cardiac troponin T lead to distinct energetic phenotypes in intact mouse hearts.* Biophysical Journal. 93, 1834-1844 (2007).
96. Richard P., Charron P., Carrier L., Ledeuil C., Cheav T., Pichereau C., Benaiche A., Isnard R., Dubourg O., Burban M., Gueffet J. P., Millaire A., Desnos M., Schwartz K., Hainque B. and Komajda M. *Hypertrophic cardiomyopathy: distribution of disease genes, spectrum of mutations, and implications for a molecular diagnosis strategy.* Circulation 107, 2227-2232 (2003).
97. Pohlmann L., Kröger I., Vignier N., Schlossarek S., Krämer E., Coirault C., Sultan K. R., El-Armouche A., Winegrad S., Eschenhagen T. and Carrier L. *Cardiac myosin-binding protein C is required for complete relaxation in intact myocytes.* Circulation Research 101, 928-938 (2007).
98. Carrier L., Mearini G., Stathopoulou K. and Cuello F. *Cardiac myosin-binding protein C (MYBPC3) in cardiac pathophysiology.* Gene 573, 188-197 (2015).
99. Carrier L. *Cardiac myosin-binding protein C in the heart.* Archives des Maladies du Coeur et des Vaisseaux 100, 238-243 (2007).

100. Sadayappan S. and de Tombe P. P. *Cardiac myosin binding protein-C: redefining its structure and function.* Biophysical Reviews 4, 93-106 (2012).

101. Olivotto I., Girolami F., Ackerman M. J., Nistri S., Bos J. M., Zachara E., Ommen S. R., Theis J. L., Vaubel R. A., Re F., Armentano C., Poggesi C., Torricelli F. and Cecchi F. *Myofilament protein gene mutation screening and outcome of patients with hypertrophic cardiomyopathy.* Mayo Clinic Proceedings 83, 630-638 (2008).

102. Vignier N., Schlossarek S., Fraysse B., Mearini G., Krämer E., Pointu H., Mougenot N., Guiard J., Reimer R., Hohenberg H., Schwartz K., Vernet M., Eschenhagen T. and Carrier L. *Nonsense-mediated mRNA decay and ubiquitin-proteasome system regulate cardiac myosin-binding protein C mutant levels in cardiomyopathic mice.* Circulation Research 105, 239-248 (2009).

103. De Lange W. J., Grimes A. C., Hegge L. F., Spring A. M., Brost T. M. and Ralphe J. C. *E258K HCM-causing mutation in cardiac MyBP-C reduces contractile force and accelerates twitch kinetics by disrupting the cMyBP-C and myosin S2 interaction.* The Journal of General Physiology 142, 241-255 (2013).

104. Narolska N. A., Eiras S., van Loon R. B., Boontje N. M., Zaremba R., Spiegelen Berg S. R., Stooker W., Huybregts M. A., Visser F. C., van der Velden J. and Stienen G. J. *Myosin heavy chain composition and the economy of contraction in healthy and diseased human myocardium.* Journal of Muscle Research and Cell Motility 26, 39-48 (2005).

105. Potma E. J., Stienen G. J., Barends J. P. and Elzinga G. *Myofibrillar ATPase activity and mechanical performance of skinned fibres from rabbit psoas muscle.* Journal of Physiology 474, 303-317 (1994).

106. Bria A. and Iannello G. *TeraStitcher - A tool for fast automatic 3D-stitching of teravoxel-sized microscopy images.* BMC Bioinformatics 13, 1-15 (2012).

107. de Tombe P. P., Stienen G. J. *Protein kinase A does not alter economy of force maintenance in skinned rat cardiac trabeculae.* Circulation Research 76, 734-741 (1995).

108. Witjas-Paalberends E. R., Piroddi N., Stam K., van Dijk S. J., Oliviera V. S., Ferrara C., Scellini B., Hazebroek M., ten Cate F. J., van Slegtenhorst M., dos Remedios C., Niessen H. W., Tesi C., Stienen G. J., Heymans S., Michels M., Poggesi C., van der Velden J. *Mutation in MYH7 reduce the force generating capacity of sarcomeres in human familiar hypertrophic cardiomyopathy.* Cardiovascular research 99, 432-441 (2013).

109. Van Dijk S. J., Dooijes D., Dos R. C., Michels M., Lamers J. M., Winegrad S., Schlossarek S., Carrier L., Ten Cate F. J., Stienen G. J. M., Van der Velden J. *Cardiac myosin-binding protein Cmutations and hypertrophic cardiomyopathy: haploinsufficiency, deranged phosphorylation, and cardiomyocyte dysfunction.* Circulation 119, 1473-1483 (2009).

110. Hoskins A. C., Jacques A., Bardswell S. C., McKenna W. J., Tsang V., dos Remedios C. G., Ehler E., Adams K., Jalilzadeh S., Avkiran M., Watkins H., Redwood C., Marston S. B., Kentish J. C. *Normal passive viscoelasticity but abnormal myofibrillar force generation in human hypertrophic cardiomyopathy.* Journal of Molecular and Cellular Cardiology 49,737-745 (2010).

111. Kraft T., Witjas-Paalberends E. R., Boontje N. M., Tripathi S., Brandis A., Montag J., Hodgkinson J. L., Francino A., Navarro-Lopez F., Brenner B., Stienen G. J. M., Van der Velden J. *Familial hypertrophic cardiomyopathy: functional*

*effects of myosin mutation R723G in cardiomyocytes.* Journal of Molecular and Cellular Cardiology 57,13-22 (2013).

112. Van Dijk S. J., Paalberends E. R., Najafi A., Michels M., Sadayappan S., Carrier L., Boontje N. M., Kuster D. W., Van S. M., Dooijes D., Dos R. C., Ten Cate F. J., Stienen G. J. M., Van der Velden J. *Contractile dysfunction irrespective of the mutant protein in human hypertrophic cardiomyopathy with normal systolic function.* Circulation Heart Failure 5,36-46 (2012).

113. Montgomery D. E., Tardiff J. C., Chandra M. *Cardiac troponin T mutations: correlation between the type of mutation and the nature of myofilament dysfunction in transgenic mice.* The Journal of Physiology 536, 583-592 (2001).

114. Coppini R., Ho C. Y., Ashley E., Day S., Ferrantini C., Girolami F., Tomberli B., Bardi S., Torricelli F., Cecchi F., Mugelli A., Poggesi C., Tardiff J. and Olivotto I. *Clinical phenotype and outcome of hypertrophic cardiomyopathy associated with thin-filament gene mutations.* Journal of the American College of Cardiology 64, 2589-2600 (2014).

115. Tardiff J. C. *Thin filament mutations: developing an integrative approach to a complex disorder.* Circulation Research 108, 765-782 (2011).

116. Varnava A. M., Elliott P. M., Baboonian C., Davison F., Davies M.J. and McKenna W. J. *Hypertrophic cardiomyopathy: histopathological features of sudden death in cardiac troponin T disease.* Circulation 104, 1380-1384 (2001).

117. Maron B. J., Wolfson J. K., Epstein S. E. and Roberts W. C. *Intramural ("small vessel") coronary artery disease in hypertrophic cardiomyopathy.* Journal of the American College of Cardiology 8, 545-57 (1986).

118. Tanaka M., Fujiwara H., Onodera T., Wu D. J., Hamashima Y. and Kawai C. *Quantitative analysis of myocardial fibrosis in normals, hypertensive hearts, and*

*hypertrophic cardiomyopathy.* British Heart Journal 55, 575-581 (1986).

119. Factor S. M., Butany J., Sole M. J., Wigle E. D., Williams W. C. and Rojkind M. *Pathologic fibrosis and matrix connective tissue in the subaortic myocardium of patients with hypertrophic cardiomyopathy.* Journal of the American College of Cardiology 17, 1343-1351 (1991).
120. Shirani J., Pick R., Roberts W. C. and Maron B. J. *Morphology and significance of the left ventricular collagen network in young patients with hypertrophic cardiomyopathy and sudden cardiac death.* Journal of the American College of Cardiology 35, 36-44 (2000).
121. Basso C., Thiene G., Corrado D., Buja G., Melacini P. and Nava A. *Hypertrophic cardiomyopathy and sudden death in the young: pathologic evidence of myocardial ischemia.* Human Pathology 31, 988-998 (2000).
122. Selcuk Adabag A., Maron B. J., Appelbaum E., Harrigan C. J., Buros J. L., Michael Gibson C., Lesser J. R., Hanna C. A., Udelson J. E., Manning W. J. and Maron M. S. *Occurrence and Frequency of Arrhythmias in Hypertrophic Cardiomyopathy in Relation to Delayed Enhancement on Cardiovascular Magnetic Resonance.* Journal of the American College of Cardiology 51, 1369-1374 (2008).
123. Tardiff J. C., Hewett T. E., Palmer B. M., Olsson C., Factor S. M., Moore R. L., Robbins J. and Leinwand L. A. *Cardiac troponin t mutations result in allele-specific phenotypes in a mouse model for hypertrophic cardiomyopathy.* The Journal of Clinical Investigation. 104, 469-481 (1999).
124. Javadpour M. M., Tardiff J. C., Pinz I. and Ingwall J. S. *Decreased energetics in murine hearts bearing the r92q mutation in cardiac troponin t.* The Journal of Clinical Investigation. 112, 768-775 (2003).

125. Matiukas A., Mitrea B. G., Qin M., Pertsov A. M., Shvedko A. G., Warren M. D., Zaitsev A. V., Wuskell J. P., Wei M. D., Watras J. and Loew L. M. *Near-infrared voltage-sensitive fluorescent dyes optimized for optical mapping in blood-perfused myocardium.* Heart Rhythm 4, 1441-1451 (2007).

126. Scardigli M., M¨ullenbroich C., Margoni E., Cannazzaro S., Crocini C., Ferrantini C., Coppini R., Yan P., Loew L. M., Campione M., Bocchi L., Giulietti D., Cerbai E., Poggesi C., Bub G., Pavone F. S. and Sacconi L. *Real-time optical manipulation of cardiac conduction in intact hearts.* The Journal of Physiology 596, 3841-3858 (2018).

127. Mullenbroich M. C., Silvestri L., Onofri L., Costantini I., Hoff M. V., Sacconi L., Iannello G. and Pavone F. S. *Comprehensive optical and data management infrastructure for high-throughput light-sheet microscopy of whole mouse brains.* Neurophotonics 2, 041404 (2015)

128. Garcia Canadilla P., Cook A. C., Mohun T. J., Oji O., Schlossarek S., Carrier L., McKenna W. J., Moon J. C. and Captur G. *Myoarchitectural disarray of hypertrophic cardiomyopathy begins pre-birth.* Journal of Anatomy 10, 13058 (2019).

129. Lichtman J. W. and Conchello J. A. *Fluorescence microscopy.* Nature Methods 2, 910-919 (2005).

# *Ringraziamenti*

*Tre anni! Una bella ed intensa esperienza a 360°, sia professionale che formativa, ma soprattutto la definirei esperienza di vita.*

*In questi anni, ho avuto la possibilità di svolgere un percorso di dottorato composto da numerose esperienze: ho partecipato a conferenze presentando il mio lavoro e ho collaborato con altre Università; in questo modo ho avuto la possibilità di confrontarmi con altre realtà e conoscere nuove persone. Tutto questo lo devo a Leonardo, il mio supervisor, al quale va il mio primo grazie. Voglio dirgli grazie anche per i suoi costanti entusiasmo e supporto, per la sua instancabile presenza e per aver creduto nelle mie capacità.*

*È chiaro che diverse sono le persone che mano a mano, in modi e occasioni diverse, mi hanno aiutata; a cominciare dal Prof. Francesco Saverio Pavone che ringrazio per aver permesso che il tutto si realizzasse.*

*Vorrei inoltre ringraziare il Prof. Corrado Poggesi, Cecilia, Raffaele e Giulia, per le vostre disponibilità ed essenziale collaborazione.*

*Voglio anche ringraziare Irene, che fin dall'inizio del dottorato mi ha sempre seguita, consigliata ed incoraggiata, per tutto il tempo che abbiamo passato insieme a cercare campioni invisibili e microscopici al due fotoni, per aver creduto in me e per le cose che mi ha insegnato.*

*Un grazie di "cuore" alle persone del gruppo di cui ho fatto parte, Mari, Vale, Fra e Cami, per aver condiviso avventure e disavventure, ma soprattutto per non aver mai mollato. Grazie a Mari e Vale per i confronti che abbiamo avuto, per la sincerità e la schiettezza, per aver sopportato i miei sfoghi. Voglio fare un ringraziamento particolare a Fra per il suo aiuto e per avermi chiarito le idee innumerevoli volte,*

*perché senza il suo lavoro ed impegno il mio progetto di tesi sarebbe stato incompleto.*

*Grazie a Ludo per il tempo insieme passato alla SPIM, ma soprattutto per avermi spigato cosa è l'FFT dopo pochi mesi che avevo iniziato il dottorato, non lo dimenticherò! E grazie a Giacomo che mi ha fatto scoprire cose delle quali ignoravo l'esistenza, tipo il terminale……*

*Un immenso grazie a Caroline per aver dedicato un po' del suo tempo a leggere e correggere la mia tesi.*

*Grazie a tutti quelli che sono passati dal "Pollaio", Mari, Emi, Lapo, Ire, Anto, Tomba; grazie a quelli che ancora ci sono, Ale, Elena, Tiziano; e grazie anche ad i nuovi arrivati, Cami, Cate, Pietro e Laura. Vi ringrazio per avermi incoraggiata e consigliata, ma soprattutto per avermi sopportata.*

*Grazie a tutte le persone con le quali ho condiviso laboratori, uffici, sala pranzo e pause caffè, per il tempo passato insieme, per esservi interessate a me e per l'aiuto che mi avete dato; in particolare ringrazio Luca, Carmen, Caterina, Giulia e Claudia.*

*Un ringraziamento speciale va alle persone con le quali ho condiviso questi tre anni; persone che mi hanno dato consigli preziosi in modo disinteressato, persone che mi hanno incoraggiata a fare delle scelte e prendere decisioni importanti non solo lavorative, ma anche di vita, persone che mi hanno regalato gioie e con le quali ho condiviso momenti che non dimenticherò. Non starò a fare l'elenco dei nomi di queste persone, dopotutto, si dice il peccato, ma non il peccatore.*

*Vorrei ringraziare le mie amiche, Martina, Eleonora, Alessia, Valentina, Caterina, Sara e Giulia, per esserci sempre state, per tutti i momenti passati insieme, per le risate e le serate, per le chiacchierate interminabili, perché anche se gli anni passano le cose tra noi non cambiano.*

*Grazie alla mia famiglia, presenti e assenti, senza di voi non sarei arrivata dove sono, in fondo a questo lungo, impegnativo e tortuoso cammino. Vi ringrazio per l'affetto che non mi avete mai fatto mancare e per essere sempre stati orgogliosi di me.*

*A mia nonna Fiorenza, grazie per essersi sempre impegnata e sforzata di capire cosa stavo facendo e di aver mostrato interesse al riguardo.*

*Ai miei genitori, grazie per non avermi mai fatto pensare che non avrei potuto fare quello che volevo o non diventare ciò che volessi essere. Siete il mio punto di riferimento, i miei due pilastri. Grazie per avermi sempre sostenuta, incoraggiata e spronata a dare il massimo.*

*Grazie a Sofia, mia sorella, con la quale ho condiviso tutto, che conosce di me ogni cosa e non mi giudica, presente in ogni instante della mia vita, sempre pronta ad ascoltarmi e darmi consigli. Pensando a te non posso non pensare a Lorenzo, una persona riservata che nel suo silenzio riesce a dare conforto e sostegno. Grazie!*

*Ultimo ringraziamento, ma non per importanza, va ad Alessandro, il "colpo di fulmine" nella mia vita. Grazie per esserci stato nel momento finale, probabilmente quello più difficile, per la molta pazienza che hai avuto, per avermi sopportata nonostante i miei difetti e per avermi aiutata quando ne ho avuto bisogno, ma soprattutto grazie per l'amore che non mi fai mai mancare.*